University of Southampton

Faculty of Engineering and Physical Sciences

Department of Mechanical Engineering

Understanding the Damage Accumulation and Tensile Strength in Carbon Fibre Reinforced Polymers using High Resolution *in situ* Computed Tomography

by

Sebastian Rosini

A thesis submitted for the degree of

Doctor of Philosophy

October 2019

Supervisors

Professor S. Mark Spearing

Professor Ian Sinclair

Dr. Mark N. Mavrogordato

In loving memory of
Carmela Iannucci

For all the time spent driving me to school,
the efforts to allow me to study,
the moral support.

Nothing is as beautiful and pure as the love of a mother.

(This page was intentionally left blank)

University of Southampton

Abstract

Faculty of Engineering and Physical Sciences
Department of Mechanical Engineering

A thesis submitted for the degree of
Doctor of Philosophy

Understanding the Damage Accumulation and Tensile Strength in Carbon Fibre Reinforced Polymers using High Resolution *in situ* Computed Tomography

by
Sebastian Rosini

Currently, composite components are widely adopted in aerospace applications but typically over-designed due to the lack of reliable predictive models for their mechanical properties. The objective of this thesis is to reach a higher level of understanding of the damage accumulation processes occurring in tensile loaded carbon fibre reinforced polymer systems to advance the development of predictive models. *In situ* loading combined with high-resolution Synchrotron Radiation Computed Tomography (SRCT) imaging has allowed a data-rich investigation of the key mechanisms leading to the final failure in different material systems. An extensive database of performance and damage behaviour has been compiled and systematic comparisons performed for material systems consisting of aerospace and industrial grade fibres, as well as different levels of adhesion of the fibre/matrix interface, obtained through changes in the sizing agent and fibre surface treatment. Focus was given to the damage mode that drives tensile failure in unidirectional layers loaded in the fibre direction: i.e. fibre failure, as this is often considered to be the final failure event in the application of multi-layered components. Clusters of fibre breaks (hereby indicated as multiplets) are believed to play a significant role in the provision of a critical crack site that propagates to final failure. Both qualitative and quantitative analyses have been performed, indicating that the accumulation of fibre breaks does not have a simple correlation to the macroscopic properties of the material, such as the ultimate tensile strength (UTS) and the fibre type but particularly the fibre/matrix interface have been observed to affect the multiplet formation.

The morphology of local damaged sites has been investigated in a novel statistical approach, needed to distinguish very similar fibre arrangements. Automated tools have been specifically developed to extract fibre breaks and the fibre shapes from low contrast images with high fibre volume fraction. The fibre misorientation in damaged sites is seen to differ statistically from that in non-damaged sites (using well recognised statistical tools) and the single fibre misorientation distributions show a consistently higher standard deviation in orientation when compared to intact fibre distributions, even though locally damaged sites did not exhibit a peculiar fibre packing arrangement. The research provides a unique database of data as well as automated statistically inferred tools that can provide a better insight into the fundamental mechanisms leading to tensile failure in longitudinally loaded composites, supporting the model development in two different phases: (a) at the initial stages, identifying phenomena and influences that should be included in accurate but parsimonious model formulation and (b) at a quantitative calibration/verification point, providing critical but previously unavailable numerical descriptions of micro-mechanical processes.

DECLARATION OF AUTHORSHIP

I, **Sebastian Rosini**, declare that this thesis and the work presented in it are my own and has been generated by me as the result of my own original research titled, **Understanding the Damage Accumulation and Tensile Strength in Carbon Fibre Reinforced Polymers using High Resolution *in situ* Computed Tomography**.

I confirm that:

1. This work was done wholly or mainly while in candidature for a research degree at this University;
2. Where any part of this thesis has previously been submitted for a degree or any other qualification at this University or any other institution, this has been clearly stated;
3. Where I have consulted the published work of others, this is always clearly attributed;
4. Where I have quoted from the work of others, the source is always given. With the exception of such quotations, this thesis is entirely my own work;
5. I have acknowledged all main sources of help;
6. Where the thesis is based on work done by myself jointly with others, I have made clear exactly what was done by others and what I have contributed myself;

7. Either none of this work has been published before submission, or parts of this work have been published as:
    - Rosini, Sebastian, Mavrogordato, Mark N., Egorova, Olga, Matthews, Emily S., Jackson, Samuel E., Spearing, S. Mark and Sinclair, Ian (2019) In situ *statistical measurement of local morphology in carbon-epoxy composites using synchrotron X-ray computed tomography.* Comp. Part A: Appl. Sci. and Manu., 125. (doi:10.1016/j.compositesa.2019.105543);

Signed: ....

Date: ....

ACKNOWLEDGEMENTS

I would like to express my sincere gratitude to my advisors Prof. S. Mark Spearing, Prof. Ian Sinclair and Dr. Mark Mavrogordato for the continuous support of my Ph.D study and related research, for their patience, motivation, and immense knowledge. Their guidance helped me in all the time of research and writing of this thesis. I could not have imagined having better advisors and mentors for my Ph.D study.

Besides my advisors, I would like to thank the rest of my thesis committee: Prof. Michael Sutcliffe, Prof. Fabrice Pierron and Dr. Stephen W. Boyd for their insightful comments, but also for the hard questions which encouraged me to widen my research from various perspectives.

I would like to acknowledge the European Synchrotron Radiation Facility for provision of synchrotron radiation facilities and would like to thank Dr. Lukas Helfen and Ms. Elodie Boller for assistance in using beamline ID19. I also gratefully acknowledge Mr. Tsuneo Takano, Mr. Naoki Sugiura and Mr. Akinobu Sasaki from Mitsubishi Chemical Co. for materials supply and support, the EPSRC for funding under grant EP/M508147/1 and the µ-VIS X-Ray Imaging Centre at the University of Southampton for provision of tomographic imaging facilities, supported by EPSRC grant EP-H01506X, with particular thanks to Dr. Richard Boardman and Dr. Kathryn Rankin for the continuous support and the help in handling the great amount of data produced during the synchrotron sessions, and Dr. Sharif Ahmed for preparing me to my first synchrotron session and introducing me to the image processing world. Thank you to Dr. Olga Egorova, Dr. Emily S. Matthews and

Dr. Samuel E. Jackson from the Department of Statistics and Mathematics Sciences, University of Southampton, for the help with the statistical analysis of the data.

I thank my friend and colleague Antonio De Grazia for the stimulating discussions and the weekends spent working together before deadlines. I also thank in no particular order: Federica Teodoro, Chiara Petroselli, Sara Ferri, Mariaconcetta Alteno, Martina Dell'Albani, Giuliana Benina, Alessandro Lorefice, Annalisa Privitera and Pasquale Romano. Thank you for being family to me and supporting me through the difficult times of these last years.

Last but not the least, I would like to thank my father: you supported me spiritually throughout writing this thesis and my life in general, always believing in me.

LIST OF ACRONYMS

A-D Anderson-Darling test
BIS Break Influence Superposition technique
BVID Bare Visible Impact Damage
CFRP Carbon Fibre Reinforced Polymers
CSA Cross-Sectional Area
CT Computed Tomography
DVC Digital Volume Correlation
ESRF European Sycnhrotron Radiation Facility
FBM Fibre Bundle Model
FBP Filtered Back Projection reconstruction
K-S Kolmogorov-Smirnov test
LGF Lattice Green Function
NDE Non-Destructive Evaluation
PLAW Power-Law Accelerated Weibull distribution
RVE Representative Volume Element
QIS Quadratic Influence Superposition technique
SEM Scanning Electron Microscope
SFC Stress Concentration Factor
SRCT Synchrotron Radiation Computed Tomography
UTS Ultimate Tensile Strength
WOW Weibull Of Weibulls model
WWFE World-Wide Failure Exercises

(This page was intentionally left blank)

CHAPTER 1

INTRODUCTION

In implementing the Paris Agreement [1], the EU 2020 Climate and Energy Package was introduced to achieve a 20% reduction in the total greenhouse gas emissions compared to 1990 levels [2]. The European Council has then raised the goal to 40% within the new 2030 Framework [3]. The transportation sector is particularly targeted and is an area in need of solutions to cut the CO_2 and NO_x emissions to meet the new tighter limits. Thanks to a variety of beneficial properties (such as high specific structural properties, customisable anisotropic behaviour, potential to integrate sensors and actuators, high structural damping and good fatigue performance), carbon fibre composite materials have been replacing traditional materials in transportation applications over the last few decades [4]. Moreover, high specific strength and stiffness, corrosion resistance and high energy absorption capabilities have highlighted their potential in other sectors, such as construction and medical orthopaedics [5]. Within the transport sector, a key benefit is the potential fuel saving linked to weight reductions that are made possible and hence carbon fibre composite materials are playing a crucial role in the realisation of the climate plan and emissions targets. Globally, automotive companies are pushing towards lightweight composite materials for use in electric cars [6], while aerospace manufacturers in the last decade have greatly increased the applicability in air-framing; the Boeing 787 Dreamliner consists of 50% by weight of composite material, that translates into 32 tonnes of continuous fibre composites per aircraft, of which 23 tonnes is carbon fibre composite [7].

Many other areas of applicability for carbon fibre composites can be envisaged, ranging from the defence sector, to sports equipment such as bikes, golf clubs, paddles, boats, and racquets. Carbon fibre composites are also being adopted for under-water pipeline applications, avoiding traditional issues with corrosion, as well as high temperature pressure operating environments that represented a challenge for steel [8]. Highly graphitic carbon fibres are also attractive for electronic systems that require improved heat transfer away from electronic components [9, 10]. An important niche market is identifiable in high-pressure gas cylinders applicable to life-protecting breathing apparatus for medical use and emergency service first responders, through to alternative fuel vehicles (e.g. hydrogen) [23].

The ability to optimise composite structures to assist in meeting tight limits in greenhouse gas emissions is arguably constrained by the lack of reliable prediction models for mechanical performance and tailored advanced design tools [11]. The damage and failure modes of composite structures present new challenges for in-service assessment and non-destructive evaluation (NDE) techniques: for example, the 'barely visible impact damage' (BVID) that can be caused by a tool drop during maintenance can be very hard to detect and a combination of different NDE methods, such as such as visual inspection, tap testing, through-transmission ultrasonics, radiography and thermography might be needed to characterise the severity of the damage [7]. The development of reliable models and experimental validation routines are a key step in realising the true potential for this class of materials [12, 13].

Failure of continuous fibre laminates under arbitrary stress states commonly involves a complex interaction of events, such as fibre/matrix debonding matrix cracking, delamination, fibre breakage and ply failure. The final tensile failure of multi-directional laminates is often attributed to failure of the tows or plies aligned to the loading direction. Hence, in improving the understanding of failure in multidirectional composites, a key role is played by the longitudinal damage development in a 0°(with respect to the loading direction) ply [14].

This study will be focused on the longitudinal tensile failure of continuous composites, while details on the compressive failure for example (dominated by plastic fibre kinking) can be found elsewhere [15–21]. In the final stages of longitudinal tensile failure, individual fibre breakages are reported [22] that cause stress concentrations on the surrounding fibres. For a high level of applied stress, groups of interacting fibre breaks (multiplets) are seen to appear in experimental observations – often in different and seemingly unrelated locations from the previously formed individual fibre breaks [14]. This observation highlights a discrepancy between experimental observations, obtained via *in situ* synchrotron radiation computed tomography (SRCT) [22–24] and various established modelling predictions that assume single fibre breaks progressively evolve into multiplets prior to final failure [25–30]. This is in contrast to the experimental observations, clearly indicating no significant multiplet growth in terms of number of breaks at a given break site prior to failure [31]. Prior to failure, more multiplets form within a given ply - eventually triggering final failure of the entire composite component. This is often linked to the development and existence of a cluster of critical size [14, 32].

However, no experimental evidence has definitely confirmed this yet, and exactly how the final failure event is controlled remains one of the questions that is not completely understood and limits the use of accepted prediction models for reliable industrial design and development [14]. To attempt to answer this question and provide modellers with the data they need, experimental validation methods is required, with SRCT appearing to be a promising tool to non-destructively track the damage micro-mechanisms in composites under load (*in situ*) [32].

1.1 Aims and objectives

The present work uses SRCT to reach a better understanding of the micro-mechanisms leading to failure in longitudinally tensile loaded composites, through a data-rich approach that has provided a unique analysis with the following aims:

- analysis of the effects of different sizing types, surface treatments and fibre diameters (not accounted in the currently available predictive models [32]) on the macroscopic properties of CFRPs, e.g. ultimate tensile strength (UTS), and on the damage accumulation, e.g. fibre break accumulation;
- detailed assessment on the formation, local morphology and evolution of clusters of interacting fibre breaks (multiplets), obtained through a careful comparison

of the data obtained from coupons of the same material to assess levels of reproducibility, as well as from coupons with systematic variations in material properties;

- identification of potential connections between local fibre misorientation, packing and Weibull strength distribution in tensile failure processes, implementing automated image processing techniques in combination with reliable statistical tools to extract and evaluate micro-structural information from large volumes of CT data.

1.2 Thesis structure

The content of the thesis is based on three journal papers, written at the end of the current research period. One of these has been published (Chapter 6), with the remaining two being in preparation (Chapter 4 and 5). For this reason, the chapters are self-contained and some repetition of information can be found in the introduction section of the chapters. The structure of the thesis is as follows:

- Chapter 2 - Presents the literature review on tensile failure mechanisms. The chapter encompasses the typical distribution adopted to describe the strength of the carbon fibres, the fibre/matrix interface and how models have evolved since the 1940s to today. The chapter also identifies areas for analysis and provides motivation for the following experimental chapters.

- Chapter 3 - Provides an overview of the X-ray Computed Tomography technique. Different methods are presented with advantages and limitations. The approach chosen for the current work is presented and justified.

- Chapter 4 – Describes the material properties, experimental procedures and the semi–automated tools developed to reduce the processing time of the many 3D imaging volumes collected during the main synchrotron test campaign. The effects of different fibre types, sizing and surface treatments on the strength of the materials are presented.

- Chapter 5 – Discusses qualitatively and quantitatively the effects of the different fibre types and treatments on damage development at a micro-scopic level, with particular focus on the planar multiplets.
- Chapter 6 – Presents an automated approach adopting image processing techniques and reliable statistical tools to investigate at a micro-scale level single and adjacently coupled fibre break locations and clarify the local fibre misorientation and packing effects on the tensile failure processes.
- Chapter 7 - Summarises the conclusions of the current work and discusses the implications with respect to the further work.

1.3 List of publications

- Rosini, Sebastian, Mavrogordato, Mark N., Egorova, Olga, Matthews, Emily S., Jackson, Samuel E., Spearing, S. Mark and Sinclair, Ian (2019) In situ *statistical measurement of local morphology in carbon-epoxy composites using synchrotron X-ray computed tomography.* Composites Part A: Applied Science and Manufacturing, 125. (doi:10.1016/j.compositesa.2019.105543);
- Rosini, Sebastian, Mavrogordato, Mark N., Spearing, S. Mark and Sinclair, Ian. *Fibre failure assessment in carbon fibre reinforced polymers under tensile loading using* in situ *synchrotron X-ray computed tomography.* In preparation;
- Rosini, Sebastian, Mavrogordato, Mark N., Spearing, S. Mark and Sinclair, Ian. *Planar fibre break cluster assessment in carbon fibre reinforced polymers under tensile loading using* in situ *synchrotron X-ray computed tomography.* In preparation;
- Rosini, Sebastian, Mavrogordato, Mark N., Spearing, S. Mark and Sinclair, Ian. *Understanding the Damage Accumulation and Tensile Strength in Carbon/Epoxy Composites using High Resolution Computed Tomography.* In, 18th European Conference on Composite Materials, Athens, Greece, 24-28 June 2018.

(This page was intentionally left blank)

CHAPTER 2

LITERATURE REVIEW

The literature review describes the reported statistical nature of the fibre strength and how is thought to affect the accumulation of damage in tensile loaded CFRPs. Matrix and interfacial properties are examined for their direct influence on the magnitude and extent of stress concentrations leading to longitudinal tensile failure. An overview of the early models is provided that starts from the simpler 2D cases with few fibres, moving on to more complex 3D configurations of randomly distributed fibres, to the current models. Recent models that include the dynamics of the fibre failure processes are presented, potentially represent an important development in modelling the tensile failure of composites. A review of previous studies making use of computed tomography to understand damage in tensile loaded CFRPs are encompassed, that have set the basis for the current work. Lastly, the current chapter identifies the gaps in the literature that this work aims to fill.

2.1 Introduction

Examples of composite material utilisation can be found profusely in history [33]. Egyptians were applying the concept of composite material when using glued laminated wood for making furniture and statuary. Nowadays, a strategic role in aerospace engineering is covered by materials made of polymer-matrix reinforced by fibres with the key concept of reaching very high stiffness and strength-to-weight ratios. Innumerable types of composites can be designed by associating different matrices (e.g. polymer, metal, ceramic) with different kinds of fibres (e.g. carbon, glass, silicon carbide). Micro-mechanical analysis has a fundamental role in composite failure analysis as it allows one to correlate the properties of the composite constituents (i.e. fibre and matrix) to the composite structure properties. As such, this review is focused on micro-mechanics of contemporary carbon fibre reinforced composites, with particular emphasis on processes occurring down to the single fibre level, i.e. in the order of a few micro-metres.

Composite materials display complex failure modes, such as fibre tensile failure, fibre buckling, inter-lamina delamination and transverse ply cracking, typically interacting with each other and occurring at different length-scales [22]. Any solid generalised failure prediction framework relies on the accuracy in all these aspects [12].

Fibre properties have an important role in defining the tensile strength of CFRPs and having a complete understanding of the fibre failure processes is vital to improve the properties of these materials, as tensile strength is a key property for many applications [23, 34, 35]. It is widely recognised that when a fibre breaks within a composite due to tensile loading, the matrix transfers the stress to the neighbouring fibres, and along the length of the broken fibre. If the load continues growing, the stress on neighbouring fibres will increase, potentially causing them to break in the vicinity of the original break. This phenomenon is indicated in the literature as “clustering” and the growth of more and larger clusters will finally lead to the failure of the composite [34]. In this work, the terms multiplet and n-plet will be used to indicate a cluster, as allowing a direct indication of the dimension of the cluster, e.g. a cluster made of two fibre breaks will be indicated as 2-plet or, more in general a multiplet.

Composite failure mechanisms are still far from being completely understood. Many models have been presented in recent decades with the aim of predicting the failure of a composite by representing the correct initiation and evolution of damage under load [35], and in particular for fibre break and multiplet accumulation, on which this work is focused, assumptions have been made based on relatively limited experimental observations. Composite failure differs from failure in conventional, bulk metallics, due to the pronounced anisotropy and heterogeneity. Composite failure mechanisms are strongly dependent on the material lay-up and the direction/type of loading [34]. Several micro-mechanical models have been developed throughout the years to predict composite behaviour under aligned uniaxial loading. It has been generally recognised that modelling the axial tensile failure must take into account the statistical nature of fibre strength, the load transfer in and around a fibre failure, and the subsequent potential for multiplet formation [23].

2.2 Fibre strength statistics

While investigating the effects of surface scratches on the mechanical strength of solids, Griffith *et al.* in 1921 [36] came to the conclusion that the presence of microscopic discontinuities, or flaws, affects the strength of materials. Carbon and glass fibres are essentially brittle and when their weakest cross-section is overloaded, they fail. Rosen in 1964 [37] introduced the weakest-link theory, considering a fibre as made of links (as shown in Figure 2.1), that is to say small segments. with failure happening in the link/segment containing the flaw of highest severity. This model is also known as the 'Chain of Links' model [38]. This phenomenon affects the average strength of the fibres as the presence of weak links has to be taken into account when evaluating the failure probability. In particular, shorter fibres will have a lower probability of having weak links, i.e. likeliness of showing a higher strength [14]. In Figure 2.2, it is shown how both the mean strength and the scatter of it is highly dependent on the fibre length (or more correctly its volume) [39]. This represents a fundamental feature of CFRP failure, as strength variability means that fibres will not all break at the same applied stress, but will follow a statistical distribution. Thus, a unique value for

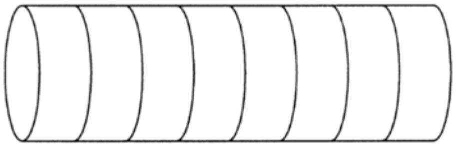

a) Fibre Exhibiting Chain of Links

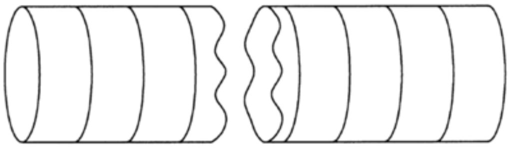

b) Fibre with a Failed Link

Figure 2.1. Fibre as described in the weakest-link theory [38].

the composite strength should not be assigned, preferring the probability of composite failure at a certain load [23, 40]. The most used approach to describe the strength of fibres is the Weibull probability distribution. Its parameters are considered in most of the tensile strength models. Weibull *et al.* in 1939 [41], showed for the first time a fibre strength probability distribution function P:

$$P(\sigma_f) = 1 - exp\left(-\left(\frac{L}{L_0}\right)\left(\frac{\sigma_f}{\sigma_0}\right)^m\right) \tag{2.1}$$

σ_f is the fibre strength, σ_0 the scale parameter, m the shape parameter or Weibull modulus, L the characteristic gauge length and L_0 the reference gauge length [42]. Single fibre tests typically use values of L_0 ranging between 10 and 50 mm and are often used to obtain the parameters σ_0 and L. In particular, σ_0 will represent the value at which 63% of the fibres will fail. The Weibull modulus m represents the parameter that influences the probability distribution, with small values of m indicating a large distribution (large scatter) (as for example $m = 3$ in Figure 2.3).

This represents the simplest equation to describe the fibre strength distribution that is commonly indicated in the literature as unimodal or two-parameter (referring to the Weibull shape and scale parameters) distribution. Other parameters and manufacturing considerations have been added during the years making the model more complex, but reported to better estimate the strength distribution of fibres (such as [43]). The unimodal distribution shown in Eq. (2.1) refers to one flaw population

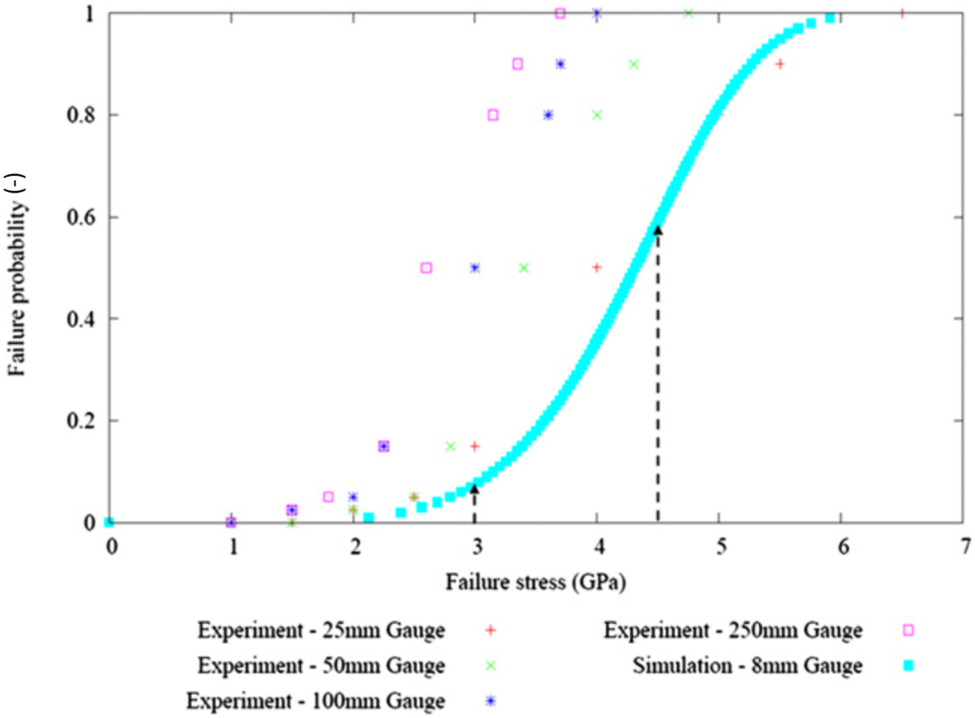

Figure 2.2. Probability of failure curves for different carbon fibres gauge lengths [39].

only. However, experiments show how outer fibres of a bundle can be exposed to different temperatures or to friction, leading to other strength-determining flaws [14].

To obtain the Weibull parameters, standard test methods for single fibres can be identified within the literature, commonly based on fibres being extracted from a yarn, fixed by epoxy glue on a cardboard frame that is then cut in the central region to act as loading tabs. Fibres are then loaded to failure [44]. The methodology to extract the Weibull parameters from the strength values obtained in the tests is presented in detail in [23, 38].

Most predictive models need Weibull distributions at gauge lengths L much smaller than the L_0 values noted about. The relevant lengths are often in the order of the ineffective length (definition is provided in Section 2.3.2), i.e. $\sim$100 μm [45].

Studies have mentioned that the average strength at short gauge lengths is smaller than the value predicted by the use of the unimodal distribution parameters obtained for gauge lengths in the order of 25 to 50 mm [46–48]. This has been explained in terms of fibre misalignment and/or slippage between the fibre and adhesive, causing the actual gauge length being longer than the nominal one. The brittle

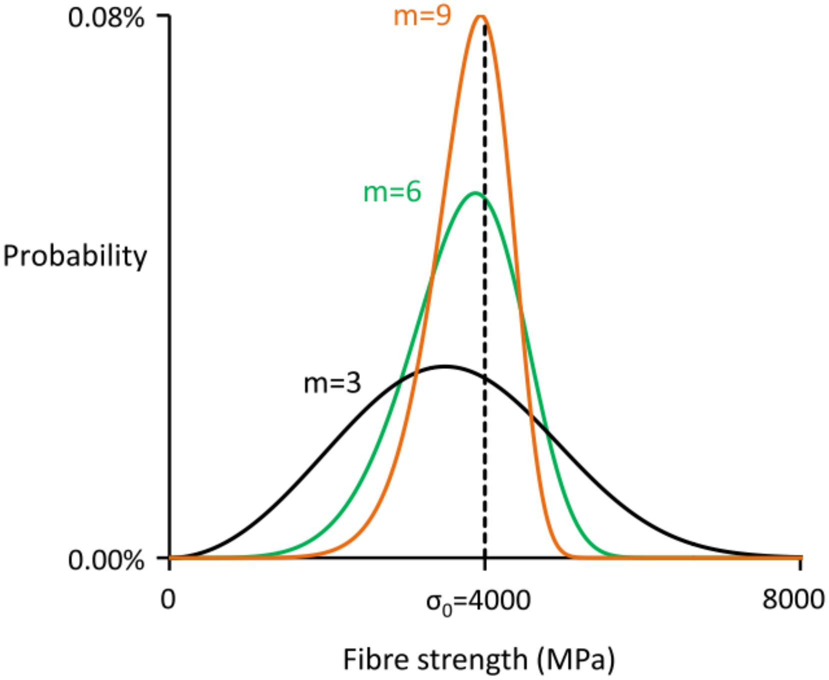

Figure 2.3. Weibull distribution example. The dependency on the Weibull modulus of the scatter in fibre strength is shown [14].

and elastic fibre is tensile loaded and the adhesive (that can be approximated as perfectly plastic) is shear loaded. In the clamping region (i.e. the region in which the fibre is fully bonded to the matrix), the stress field that can be described using the shear-lag model (illustrated in Section 2.4.1) leads to the fibre being more likely to fail in the clamping region than in the nominal gauge length [49]. Hence, shorter gauge lengths will result in higher probability of failure within the clamping region [50]. Discarding the data from the fibres prematurely failed within the clamps leads to the above-mentioned overestimation.

Moreover, as reported in [51], when extracting a fibre from a yarn for single fibre tensile testing, the fibre should possess a minimum strength to not fail during the extraction process. The effective exclusion of the weakest fibres during the extraction (they break before being loaded) then generates unrepresentative behaviour at low strength levels. In [51], it is also discussed the importance of the number of fibres tested to obtain reliable Weibull parameters, and not to falsely predict more than one flaw population if it is not case. The typical number of tested fibres reported in the literature is in the order of 20 to 50, reaching 100 in some cases [52]. In general, it is not easy to a priori establish a generally applicable number of tests that should be performed, and the number is influenced by the Weibull modulus of the fibres, as reported in [53]. To summarise: finding the optimal value for the gauge length is not easy: tests performed at below 10 mm could result in the fibres failing at the clamping region or being misaligned, while tests performed at larger gauge lengths could lead to the strongest fibres preselection, as the weakest would fail during the extraction from the yarn. Swolfs *et al.* suggest in [14], that related to experimental issues a gauge length in between the two mentioned cases (i.e. ∼10 to 25 mm) could be reasonable for most fibre types.

In [50], some advances are described in a correct evaluation of the tensile strength distribution for carbon fibres with short gauge lengths (in the order of 1 to 10 mm), of which the most important are: (i) the value of the Weibull shape parameter was experimentally found to be higher for shorter gauge lengths than for longer ones, providing indication of the strength being governed by different flaw population, i.e. a unimodal distribution is not enough, at least a bimodal model should be adopted; (ii) the tensile strength values of resin-impregnated fibre bundles predicted using the bimodal distribution were in better agreement with the experimental data (cf. using the unimodal distribution). When predicting the strength distributions of carbon fibres, models based on the unimodal Weibull distributions and that followed it were: the power-law accelerated Weibull distribution (PLAW) described in [43, 48, 54] that augmented the original model by adding an exponent α to Eq. (2.1) to account for the gauge length dependence, for which it is still unclear if it provides acceptable values at short gauge lengths [14], and the Weibull of Weibull model (WoW) that adopts a more physical approach by assuming that the strength distribution along a fibre follows a Weibull distribution. Hence, at a certain length L each fibre will have a strength value associated with it. Then, also the characteristic strengths of each fibre are assumed to follow a Weibull distribution, based on the presence of defects caused by the processing and handling of the fibres [45]. This distribution is however challenging to implement in strength models, hence is not widely adopted in contemporary models. More complex distributions are retrievable in the literature, which however often lack a clear mechanical basis, being based on a curve fitting approach [55, 56].

Although the uncertainties related to its evaluation are not negligible, the Weibull modulus is considered a parameter of great importance for the fibre break geometry evaluation. By providing an indication of the variation in the strength of the fibres [42], different behaviour in fibre break formation are expected based on its magnitude [57]. Fibres with a low Weibull modulus (i.e. exhibiting a large spread in the fibre strength values), are expected to result in a composite in which the formation of dispersed breaks will prevail over the appearance of groups of adjacent fibre breaks, hereby indicated as planar multiplets [14]. A high Weibull modulus, results in the fibres failing in a narrower range of values surrounding the mean strength. Hence, once a certain stress level is exceeded, more fibres are likely to fail together once a neighbour breaks, leading to multiplets formation [58]. Recent SRCT investigations [22, 24, 31] have asserted that dynamic effects may be an additional critical factor in multiplet formation, disregarding this point.

2.2.1 Summary

The fibre strength statistical nature is commonly described using the Weibull model [41, 42]. This distribution represents the first input parameter for modelling the longitudinal tensile strength of composites [14]. Although many studies have focused on it over the last seventy years (to cite a very few [38, 44–51, 53, 54, 59–61]), measuring this distribution still represents a difficult task, with the literature not agreeing on the most suitable corresponding statistical model [14]. The abovementioned issues are of statistical and experimental nature. A need for an improved distribution that accounts for the strength spread showing more flaw populations is indicated in the review, as well as the need for improved testing techniques accounting for gauge lengths requested by the current predictive models, which are of different magnitudes smaller than those on which most studies are based.

Notwithstanding such issues, the Weibull modulus of a fibre type may be taken as some indication of a composite that is more likely to exhibit dispersed breaks (low values of the modulus) or localised fibre break formation. Hence, attention is typically given to it when studying the fibre break behaviour of a composite material. In 1972 Phoenix *et al.* in [49] concluded their study on the clamping effects on the fibre strength extraction at short gauge length with the following: 'it is then hoped that more accurate estimates of the Weibull parameters for use with recent statistical strength theories of composite materials can be achieved'. Almost fifty years later, this statement appears to still hold and could conclude current publications on the matter.

2.3 The fibre/matrix interface

2.3.1 The matrix and the interfacial properties

In fibre reinforced composites, the matrix covers different functions: (i) protects the fibres surfaces, (ii) separates the fibres to ameliorate crack propagation and (iii) transfers the stress between the fibres [14]. The interaction between fibres and matrix is fundamental in defining the failure properties of the composite [62]. The fibre/matrix interface, which can be defined as the boundary between the two parts, transferring stresses between the fibres, predominantly via shear [63].

Surface treatment and fibre sizing are two factors that affect the interface and if used properly can control/improve load transfer, leading to a more efficient composite [64]. In the context of fibre failure, this may mean that a successful interface is one that allows enough stress to be transferred from a broken fibre to the matrix and from that to the surrounding fibres [63]. The surface of fibres is commonly treated to increase the roughness, which affects adhesion [14]. Epoxy resins, (used in the CFRPs of this study) do not bond well to non-treated carbon fibres, in which case a bonded interface could not be observed [65]: poor surface treatment could then lead to extensive fibre decohesion. After the surface treatment, a fibre sizing process follows, with uncured resin applied in a thin layer, protecting the fibres and improving the interfacial properties [64]. In [66], carbon fibres with different surface finishes were assessed using a Broutman test, with Scanning Electron Microscope (SEM) micrographs indicating that matrix fracture observed around sized fibres (i.e. a cohesive failure), while fibres that did not undergo a sizing treatment appeared as clean from any matrix bonded to the fibre surface, i.e. an adhesive failure occurred.

The interfacial strength is generally evaluated by single fibre or multi-fibre tests, of which the most common is the fibre pull-out test, consisting of one or more fibres being pulled out of a block of resin, as shown schematically in Fig. 2.4 ([67]).

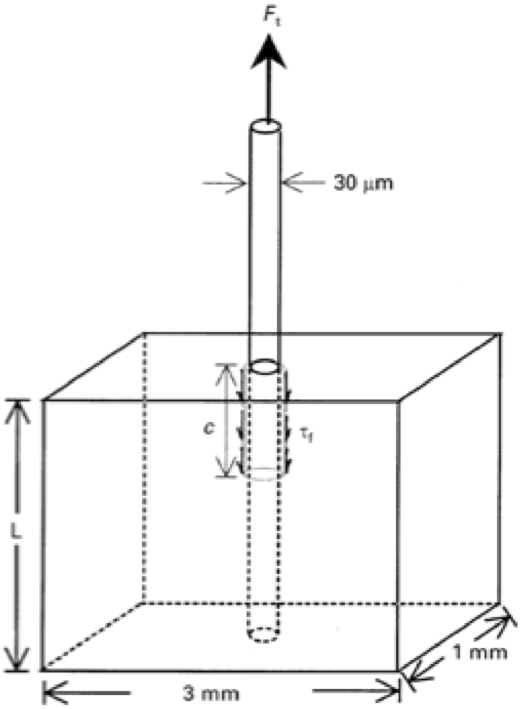

Figure 2.4. Schematic of the pull-out model, with L embedded fibre length and c, length of debond [67].

The interfacial shear stress is obtained as:

$$\tau = \frac{F_p}{\pi D_f L} \tag{2.2}$$

with F_p the peak load, D_f the fibre diameter and L the embedded fibre length. The debonding force is related to the embedded fibre length, i.e. a maximum fibre length has to be considered to allow fibre pull-out without the fibre to fail.

However, the embedded length for carbon fibres/epoxy resin reinforced materials could be less than 200 μm, making the realisation of the test complicated. An alternative to this test is then the fibre-fragmentation test. A fibre is embedded in a higher strain to failure matrix, and loaded in tension. The fibre breaks several times along its length in its weakest sections. This continues until the remaining parts of fibres are so short that the shear stress transfer between fibre and matrix is not enough to allow the tensile stress to recover, stopping any further breaks to appear

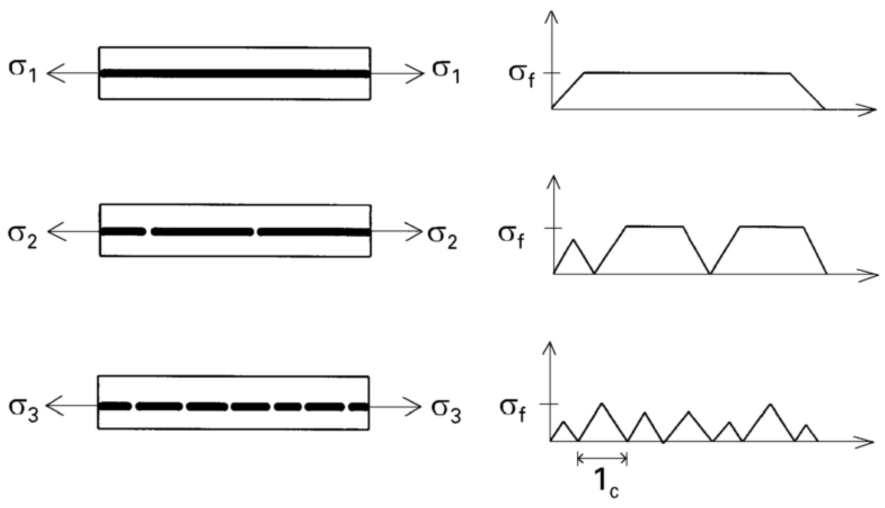

Figure 2.5. Schematic of the fragmentation test, with indicated the difference in length of the fibre fragments. l_c is the critical fibre length [68].

[68]. Fig. 2.5 shows a schematic of the test, where the difference in length of the fragments is presented. This difference in length is related to the statistical nature of the fibre strength and the shortest of these lengths represents the 'critical length'.

The main limitation of these techniques is represented by the use of a single or few fibres, not accounting for the effect of multiple neighbouring fibres. Despite this, an approximate estimate can be achieved to rank different materials [23]. In the real application, with many fibres surrounding a broken one, the shear stiffness of the material surrounding the break is higher, reducing the critical length. Hence, the nominal stress along the broken fibre will be recovered much closer to the break position if more fibres (stiffer configuration) are closely surrounding the break, i.e. the fibre volume fraction and the fibres stiffness affect this [14]. The critical length is also affected by the level of surface treatment, with increasing the interfacial shear strength, by improving surface treatment being found to yield smaller critical length [64, 66, 69].

In the first instance, very strong adhesion (high interfacial shear strength) may be expected to cause the localisation of the fracture on a given plane, making its propagation easier, while a poor adhesion would result in longer critical lengths and stress concentrations distributed over bigger regions [70]. The latter is anticipated to lead to lower composite tensile strength as the effect of the matrix spreading the load in a region close to the break is not obtained [70–72]. For this reason, it is believed that the best tensile properties can be achieved with a good compromise between the two cases indicated above [70], i.e. an interfacial strength high enough to encourage relatively short ineffective lengths, but not so strong that it results in closely spaced/planar fracture events.

Other parameters may be anticipated to affect the stress concentration around a fibre break, e.g. the fibre stiffness and any thermal residual stresses caused by the resin cure. When curing the thermoset resins, a compressive state is induced on the fibres by the matrix shrinking. However, these effects have been reported to be negligible in polymer matrix composites [73, 74]. As pointed in [14], no existing work has taken into account the energy release rate for interfacial debonding, disregarding a dynamic aspect of the problem that could be of importance.

2.3.2 Interaction between fibre breaks

As noted above, when a fibre breaks, load is transferred to the surrounding material causing a shear stress concentration in the matrix surrounding the break. If the interface between the breaking fibre and the matrix is weak, the crack may develop along the interface, otherwise the crack will propagate into matrix first, with corresponding stress concentration at the crack tip [75]. As notes, it has been suggested that the ultimate failure of a unidirectional composite may depend on the fibre break progression from a single, isolated break to multiple connected breaks until a critical cluster forms [76]. A micro-mechanical analysis of the progression of fibre failure (which takes into account the statistical aspect of the failures and the load shedding mechanics) is then necessary to define a correct failure strength value for a composite. The term ineffective length is often adopted in the literature when discussing about the stress recovery on a broken fibre [70, 77–79] and corresponds typically to the length along which the stress is lower than 90% of its nominal value. This definition is somewhat arbitrary but it is clearly an important parameter as it is related to the length over which the stress concentrations are significant [14]. Many polymer matrices experience a visco-elastic behaviour at room temperature leading to time-dependent effects on the ineffective length. The length may indeed increase as a function of time, i.e. stress concentrations over a larger area with more fibres breaking with time [14]. Where a fibre fails, the axial stress equals zero, while the shear stress reaches its maximum. Away from the break, the interfacial properties will allow axial stress recovery and the shear stress to diminish to zero. The ineffective length may be calculated as:

$$l_c = \frac{D_f}{2}\frac{\sigma_{f,ut}\left(l_c\right)_{tens}}{\tau_i} \tag{2.3}$$

where $\sigma_{f,ut}\left(l_c\right)_{tens}$ is the tensile strength at the critical length from the break, τ_i is the interfacial shear stress and D_f the fibre diameter [66]. Fig. 2.6 shows the ineffective length as obtained from a fragmentation test.

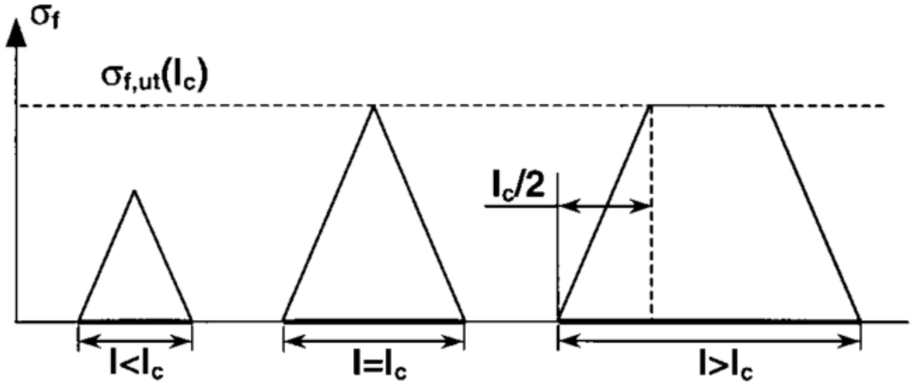

Figure 2.6. Ineffective length, showed in a fibre stress profile obtained with a fibre segmentation test [66].

Eq. (2.2) can be rewritten to obtain the interfacial shear stress transfer level $\langle\tau\rangle$ from the critical length l_c:

$$\langle\tau\rangle = \frac{d\sigma_{f,ut}\left(l_c\right)}{2l_c} \tag{2.4}$$

When a fibre breaks, the probability of another break arises along that length in surrounding fibres. As shown in Fig. 2.7, in [80] a simple 2D case is considered of a single line of parallel fibres in which a damage zone of l_c is generated after a breakage, $l_c/2$ on either side of the break. Considering the fibre adjacent to the broken one, when the load increases if this fibre breaks as well and within the ineffective length, then there will be a damaged zone between the two breaks and the two can eventually join up as indicated in Fig. 2.7a. The two will be indicated as duplet.

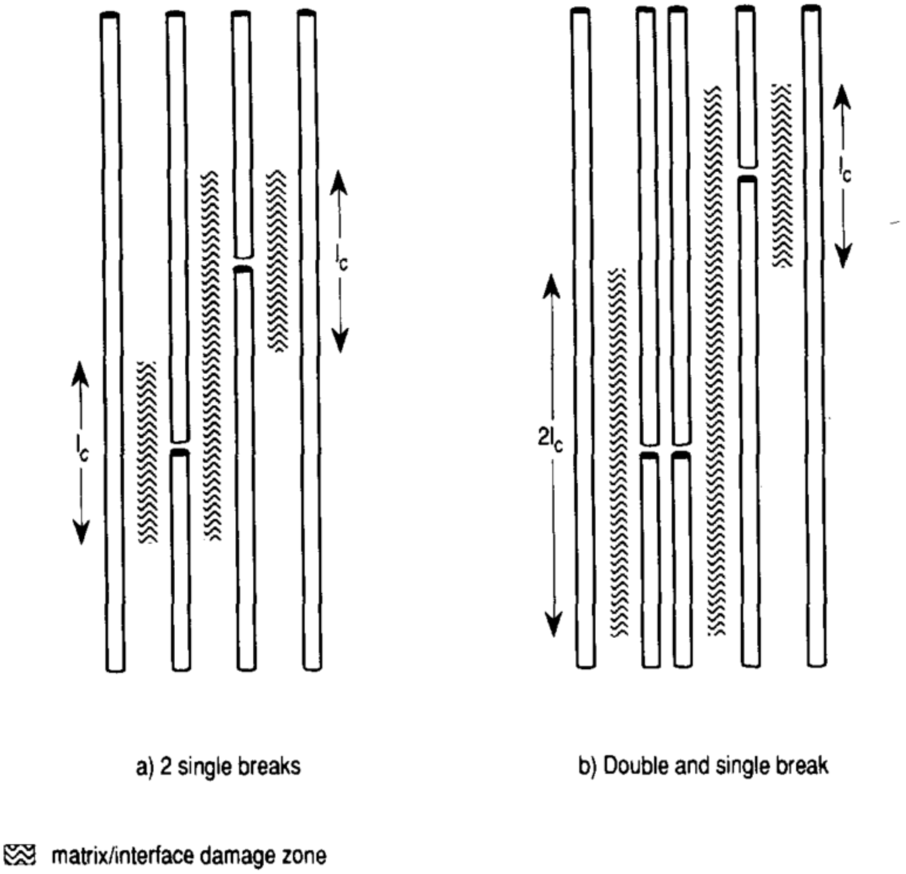

a) 2 single breaks

b) Double and single break

Figure 2.7. Fibre breaks interactions for a) two single breaks and b) a duplet plus a non-coplanar third break [80].

To simplify the problem, the two mentioned breaks can be considered to be on the same cross-section, as reported in Fig. 2.7b. The damaged zone will be wider then for the first case. If a third fibre is breaking within this wider damaged zone, this can be considered as part of the first two breaks, forming a so called triplet. Breaks will continue to interact until being within the ineffective length of each other [80]. Such interaction of breaks is of course dependent on the stress concentrations around a break site, which is dependent on the material properties [81].

2.4 The predictive strength models: an overview

2.4.1 The first analytical micro-mechanical models

The first available example of analytical composite failure modelling was the fibre bundle model (FBM) by Daniels (1945), which also was the first and simplest load redistribution model. It considered the load from a broken fibre to be carried in equal measure by all the surrounding intact fibres (a concept known as global load sharing) [75, 82]. The maximum load the bundle could support was defined for the first time as the bundle strength. A group of parallel fibres of equal length and the same load-extension curve up to the breaking point was considered and the probability distribution of the strength of the bundles was investigated [34]. However, this model examined the fibres without matrix bonding them together, with this approach then being modified and extended by many authors [75].

Cox introduced in 1952 the shear-lag model. It represents one of the main works on the analysis of the strength and damage of fibre reinforced composites; this model is commonly used to estimate the load distribution occurring on the fibres around the broken one [33]. In it's basic form, this model allows one to calculate the stresses in a fibre in an elastic matrix. Within the model the failure of one or more fibres was considered. Circular cylinder fibre geometry, negligible dynamic effects, linear elastic and isotropic matrix behaviour are some of the main assumptions considered by Cox and carried forward to in successive models based on this approach [35].

In 1972, Rosen and Zweben showed how a fibre break can influence the stresses on the surrounding fibres and this can eventually result in crack propagation along the fibre interface. Fig. 2.8 shows schematically the non-uniform stresses generated by a fibre crack. These authors also investigated the statistical nature of fibre strength considering how each broken fibre increases the probability of additional broken fibres until failure of the whole section.

Starting from the shear-lag approach by Cox, in 1961 Hedgepeth introduced the stress concentration factor (SFC) for fibres surrounding a broken one in a 2D unidirectional composite [83]. The elasticity of fibres and matrix and the independence of the SFC from fibres and matrix moduli and from the distance between the fibres were the main assumptions of this model. The SCF for intact fibres surrounding up to six broken fibres was calculated and was found to be increasing with the adjacent breaks. However, the first version of this model over-predicted the SCF value [14].

In 1967 additional work was published by Hedgepeth and Van-Dyke in which the main corrections were the introduction of the elastic-plastic behaviour of the matrix and the extension of the study to the 3D case, although the matrix was still considered to be loaded in shear only [34, 84]. Many other authors modified Hedgepeth shear-lag model to include more complex behaviour. In 1976, Fukuda and Kawata improved the SCF calculation by introducing its dependence on the material properties and considering that the matrix carries not only shear stress but also tensile stress [85]. Obtained SCF values were lower and increased more slowly than Hedgepeth *et al.*'s values, when increasing the load level. Also, the SCF was shown to be increasing with the fibre volume fraction and the fibre/matrix moduli ratio [34].

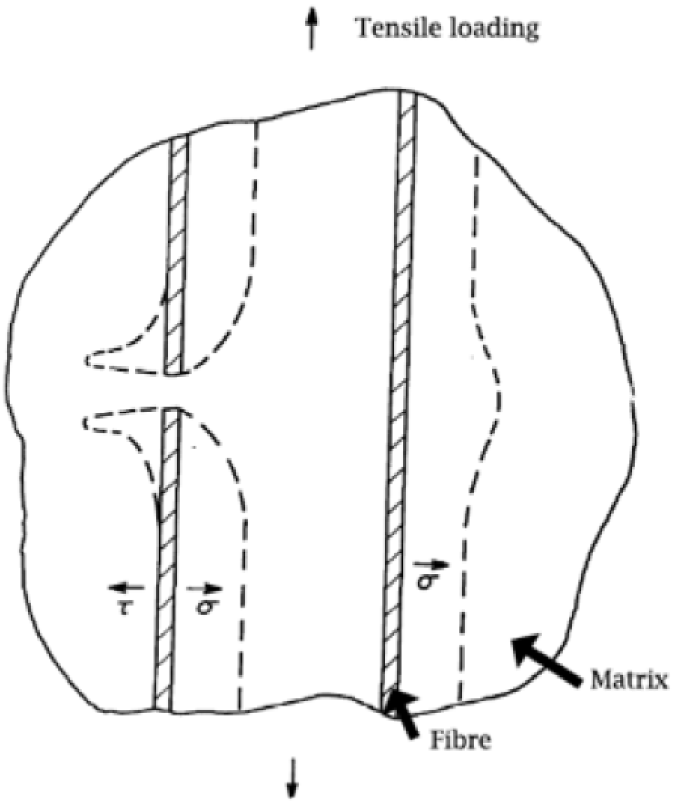

Figure 2.8. Redistribution of the stresses around a fracture site. and are respectively the tensile and shear stresses originated from a fibre break [86].

Beyerlein and Phoenix in 1996 introduced the quadratic influence superposition

(QIS) computational technique, an improvement of their previous break influence superposition technique (BIS) [63]. The QIS was proposed as an efficient model as it considered discretisation close to the fibre breaks only, while previous techniques were discretising the whole composite. This allowed the reduction of simulation times of shear-lag models. Also, the method provided more precise results by the introduction of fibre/matrix debonding and fibre pull-out as model parameters. The fibre/matrix loads and displacements are obtained by taking into account the sums of the influences of N fibre breaks, to which N equations correspond. Fig. 2.9 shows schematically the analysis of the damage of the fibres and matrix, as well as the debonding mechanism analysed by the authors.

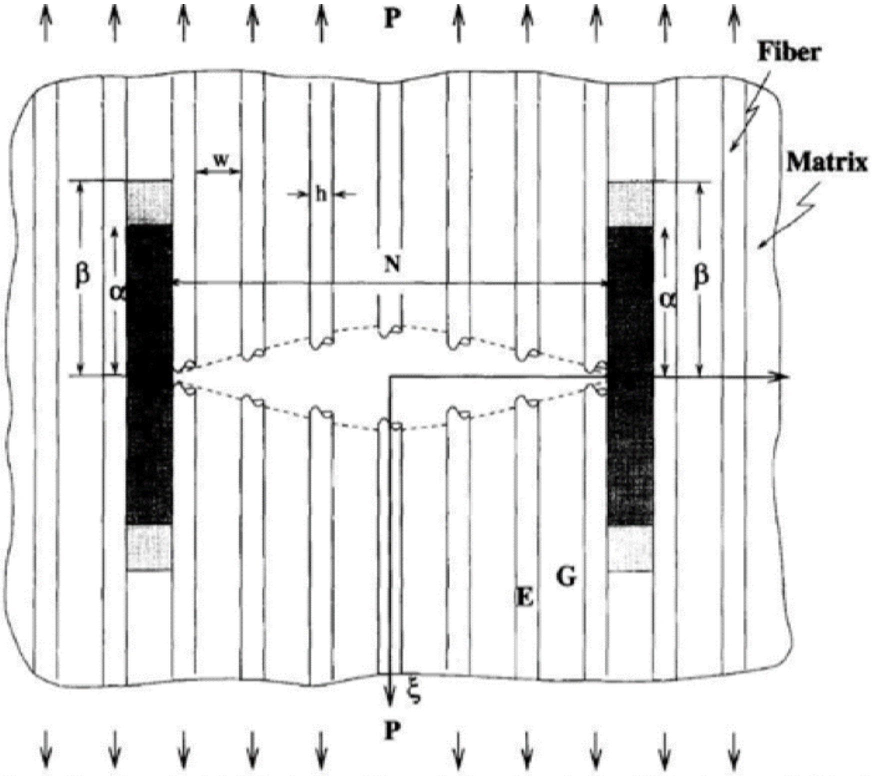

Figure 2.9. 2D composite with central crack and equispaced N fibres. Debonding lengths vary from zero to α, while yield zones extent from zero to α [63].

Within the model hundreds of breaks could be considered, and by including matrix yielding and debonding mechanisms it is shown that the stress concentration at the crack edge is reduced, the load transfer length is extended and stress decay ahead of the crack tip is reduced. Zhou and Curtin in [87], proposed a numerical simulation based on the lattice Green function (LGF) to analyse the 3D stress state of composites. Based on their work, Landis [88] and Okabe [89] built the 2D shear-lag model into a 3D model, leading to very large computational times. In [90], Okabe *et al.* proposed a novel computationally efficient approach, coupling analytical stress recovery to the shear-lag model, referred as the spring element model.

2.4.2 Contemporary models

Seventy years after the fibre bundle model (representing a first basic example of a composite model) was published, the modelling community is still refining predictive models to fully capture the tensile response of composite components. Since the 1990s, The World-Wide Failure Exercises (I, II and III) [12, 13, 91–93] have provided a comprehensive description of the widely recognised composite failure theories, comparing their predictions between each other and against experimental data. Multi-directional composites under complex 3D stress conditions were tested. The limitations and the steps to improve each models were clearly reported, as well as the recommendations on how the models could be implemented for real-world design applications. A wide range of models were included that considered micro-mechanics and finite element approaches, as well as linear and non-linear aspects, etc. [13]. A wide spread was found in the modelling predictions, highlighting the challenge in industry utilisation of composite failure models.

The main limitations about this validation exercise were: (i) models required a large amount of input properties (up to 80), of which some are of not easy to obtain, leading to the parameters being fitted so that models would provide results close to the experimental values; (ii) practical experimental issues associated with the complex loading cases coupled with the multidirectional nature of the modelled composites that have been suggested as contributing to the lack of agreement between the experimental data and model predictions.

The longitudinal tensile damage development and failure in composite are however thought to better understood [24], and given how critical the longitudinal tensile strength is for the reliability of composite structures, benchmarking exercises have been recently developed focussing on this particular damage process. Although several longitudinal tensile strength models have been checked against experiments [26, 94–

98], the experimental results were known a priori potentially engendering confirmation bias [32]. Hence, a first version of an exercise to address this issue was proposed in 2018 [10]. The benchmarking exercise focused on following the fibre break accumulation in tensile loaded unidirectional composites.

The exercise provided a comparison of the model predictions when blindly compared to a hypothetical composite material, not corresponding to any real material, and with different properties from a second material considered for comparison: based on Hexcel T800/M21. This allowed a systematic check for consistency of results among the different model approaches. A brief overview of the models analysed in [32] is hence provided here, identifiable as the contemporary models available. In addition to the models described in [32], the model from Tavares *et al.* [99, 100] is included in this review as it considers the dynamic effects on the damage accumulation in longitudinally loaded tensile composites.

2.4.2.1 The hierarchical scaling law

Described in [98, 101], this analytical model is based on previous work on the strength of dry hierarchical bundles of fibres [102], adding the shear-lag effect to explain the presence of the matrix, using [103]. Fibres are paired into hierarchical fibre bundles and failure is assumed to propagate in a hierarchical and self-similar way. It is the only model described here accounting for an ineffective length growing with the applied stress and the number of fibres involved in a cluster, based on [80]. It is the identified as a particularly computationally-efficient model of those presented here [32], without sacrificing the accuracy of predictions when comparing to the experimental results. Its analytical formulation leads to the lowest computational times, which makes the model suitable for very large structures analyses. Static studies of fibre bundles with perfectly-aligned fibres have provided maximum stress concentration factors that are lower than the value of 2 adopted in this model [25, 97].

However, Beyerlein *et al.* in [63] have shown that stress concentration factors higher than 2 should be considered in the formation of large multiplets. Furthermore, dynamic effects and real-composite random fibre misorientation might lead to higher maximum stress concentration values, that could be closer to the value adopted in the model.

2.4.2.2 Direct numerical simulations

In this model extensively described in [24–26, 104, 105], a Fibre-Bundle Model (FBM) similar to the spring element model of [90] is adopted. A random fibre packing model is produced that adds fibres at random coordinates within a square representative volume element (RVE), followed by some positioning adjustments as described in [104]. A finite element model is created using the random fibre packing. Fibres are divided into elements of the length of the fibre radius and to each element a Weibull strength is assigned. The stress redistribution around a fibre break is calculated omitting the interaction between fibre breaks. After this, a correction for the interactions between the breaks (more details can be retrieved in [26]) is added. This model has been used for hybrid composites applications [52, 106], for which it has been positively validated against experimental data [107]. Two cases are described that make use of an elastic or perfectly-plastic matrix.

The model is the most versatile of the lot and uses less assumptions. Relatively straightforward can be considered the implementation of dynamic and viscoelastic effects or the ineffective length growing with the n-plet size. The large computational time and the largest n-plet that can be modelled are the main drawbacks of the model.

2.4.2.3 The multiscale FE model

Multiscale approaches have been reported by various groups to understand the failure processes of composite structures, with a FE method that allows overcoming the classical assumption of scale separation and does not require any analytical equations to be written at the macroscopic scale (often difficult to achieve), as done in [108–110]. Non-linearities are obtained at the microscopic scale, affecting also the larger scale. The approach may be simplified by using a pre-obtained database at the micro-scale, and FE analysis only being used at the larger structural scale [27, 60, 111].

Such modelling has been reported to be tested against acoustic emission [111] and computed tomography test results [112].

In [111], the stochastic nature of fibre strength, the stress transfer between fibre and matrix, the interfacial debonding and the viscoelastic nature of the matrix are considered together to predict the failure of carbon fibre composite pressure vessels, considering the rate dependency of failure of these components. Results have shown that while the viscoelastic nature of the matrix can be assumed as negligible in the case of longitudinally loaded unidirectional carbon fibre composites, for composite pressure vessels it is not the case. The faster the loading rate, the higher the applied stress at which the vessel becomes unstable. Advantages of the approach are the possibility to use it for relatively large applications with non-uniform stress fields, and the scalability to multi-directional laminates and the assumption of visco-elasticity of the matrix (not adopted in the other models). Drawbacks are the non-suitability for very small investigations (minimum length that can be analysed is of the length of the RVE, corresponding to 4 mm in [108–110]), and the non-linear matrix response neglect.

2.4.3 The unidirectional strength models benchmarking exercise

Starting from 2014, a benchmarking exercise was organised that was published in 2018 [32]. The joint effort of the authors (Bunsell *et al.*) and the different research groups taking par (KU Leuven, Imperial College London, Mines ParisTech and University of Southampton), provides an important basis and opportunity for improved model development. The predictions of the three models described in the previous sections of Section 2.4.2 were compared against each other and against experimental data. Focus was given to the tensile strength and the accumulation of fibre breaks, under uniform monotonic stress or displacement far-field. The exercise identified the benefits and the drawbacks of the different models and the aspects that require further attention for future studies.

As noted above, two CFRPs tested in the exercise are a hypothetical composite for which the model inputs had no equivalent in reality and hence constituted a truly-blind comparison for the models, and the Hexcel HexPly T800/M21 system provided by Airbus UK with modelling inputs collected from the literature. Experiments were carried out using this system and results disclosed only after the models predictions had been collected. The fibres diameter and the longitudinal Young's modulus of the

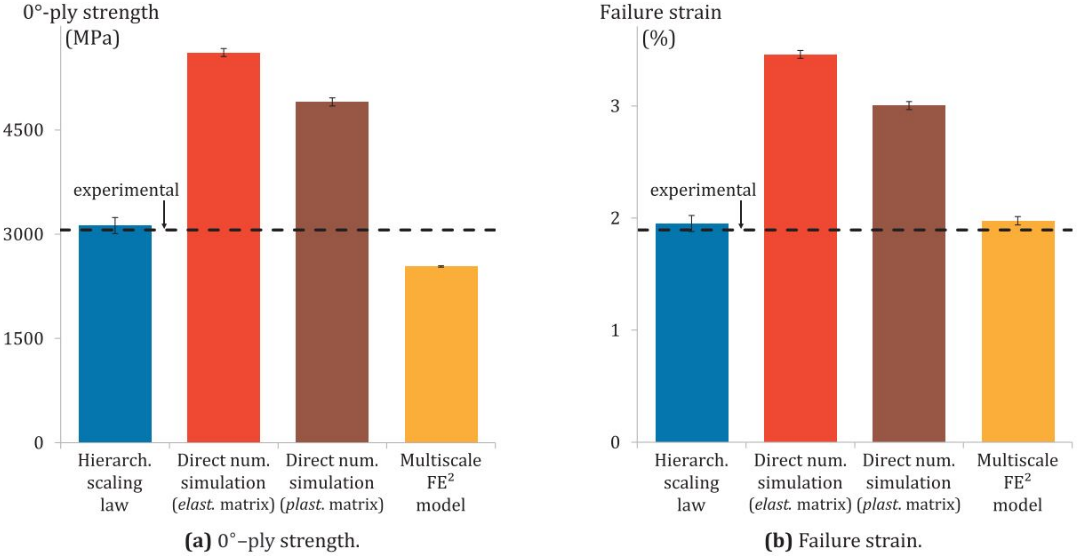

(a) 0°–ply strength. **(b)** Failure strain.

Figure 2.10. 0°-ply strength and failure strain model predictions, as shown in [32]. The hierarchical scaling law shows the closest results to the experimental values. Error bars representing ± one standard deviation.

Hexcel system were taken from the manufacturer's datasheet, and the other elastic properties extracted from [113], while the fibre strength distribution was assumed to follow a simple unimodal approach, with the parameters presented in [114]. The interlaminar shear strength was obtained from the M21 resin system datasheet. The composite geometry was examined by the researchers at the University of Southampton, evaluated from SRCT scans.

Results have showed that the hierarchical scaling law described in Section 2.4.2.1 and the multiscale FE model of Section 2.4.2.3 predict lower strength and failure strain than the direct numerical simulations of Section 2.4.2.2, as shown in Fig. 2.10. This is addressed with the assumption of a stress concentration factor of 2 in the nearest neighbour for the hierarchical model, while the other two models use lower values obtained through FE. The stress concentration is hypothesised to affect the surrounding fibres along all the length of the RVE (4 mm long) for the multiscale FE model, with the other models adopting the ineffective length (in the order of hundreds of microns). Also, the FE model models a larger specimen than what used for the experiments and hypothesised in the other two models.

As shown in Fig. 2.11, the direct simulations and the multiscale FE models

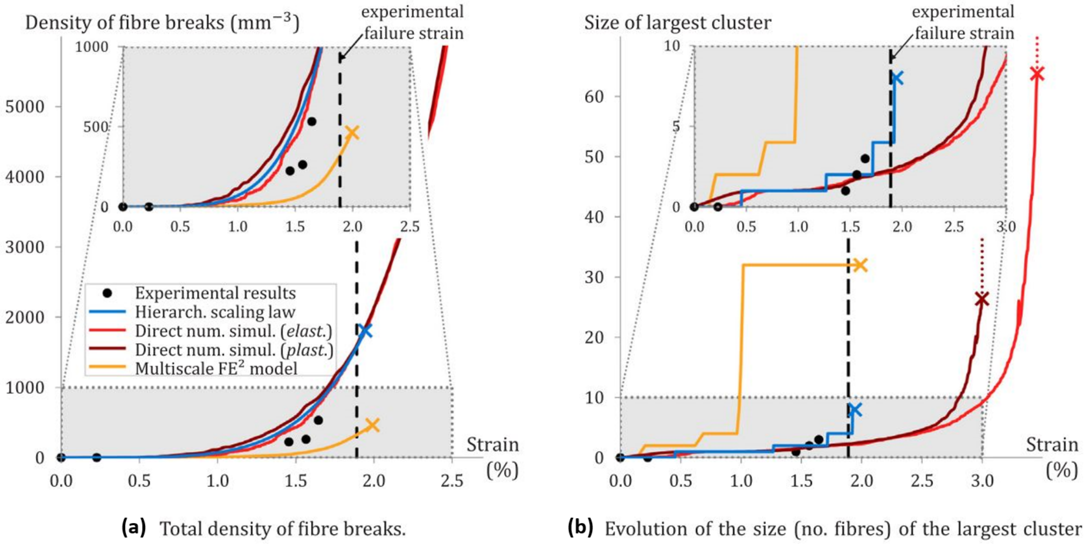

(a) Total density of fibre breaks.

(b) Evolution of the size (no. fibres) of the largest cluster

Figure 2.11. Density of fibre break predictions, as shown in [32]. The hierarchical scaling law shows the closest results to the experimental values.

predict a similar fibre break accumulation trend. This can be explained with the fibre breaks primarily being formed by individual fibre breaks, which are governed by the strength distribution that differ for the multiscale FE model. The ineffective length in the unimodal Weibull distribution in the order of mm against hundreds of microns is identified to lower the predicted number of fibre breaks, because of the different size-effects.

The planar n-plet formation and evolution is similar for the 2-plets and different for larger n for the hierarchical scaling law and the direct numerical simulation models. This can be explained with the 2-plet formation still being governed by the individual fibre strength distribution, while the larger n-plets are affected by the different stress concentration values adopted by the models. At the point of failure, the lowest number of fibres in an n-plet is predicted by the hierarchical scaling law model, consistently with the hypothesis adopted, for which a stress concentration factor equal to 2 is considered in the nearest neighbour to a broken fibre/n-plet, as well as a growing ineffective length with growing number of broken fibres in an n-plet.

In terms of failure strength and strain, the best predictions are obtained with the hierarchical scaling law and the multiscale FE models, while the closest predictions of accumulation and agglomeration of fibre breaks to the experimental data are obtained with the use of the hierarchical scaling law and direct numerical simulation models. This highlights how different modelling approaches can lead to the ability of predicting well one particular aspect of damage, while ‘missing’ another aspect.

Plasticity of the matrix was judged to have a role in the n-plet formation predictions: the hierarchical scaling law assumes a plastic matrix, as well as one of the options of the direct numerical simulation models. This has the effect of lowering the number of fibres involved in the largest n-plet formation, leading to values that are closer to what is observed experimentally.

The direct numerical simulation model with a matrix plasticity predicts values that are closer to the hierarchical scaling law model, if comparing to its elastic counterpart. Although the two models adopt different hypotheses on the stress concentration and the n-plet formation and this is clearly affecting the results, the response assumed for individual fibres and matrix seems to affect even more the results and hence the accuracy of the model predictions.

Open gaps in the literature that can be retrieved in the modelling exercise of Bunsell *et al.* in [32], are identifiable as:

(a) experimental data for model validation to provide:
    (i) variability from experimental results should be considered: a larger number of specimens should be tested to provide an indication of the variability in macro- and micro-scale response of the tested material, e.g. variability in strength and individual or group of fibre breaks accumulation count;
    (ii) consistent variation in materials parameters, e.g. fibre/matrix interface type, matrix or fibre volume fraction;
    (iii) fibre break and n-plet accumulation measurements closer to final failure, where the predictions of the models start to diverge;
    (iv) measures of the fibre break accumulation in continuous tests, rather than at discrete load steps, as matrix relaxation can affect the break accumulation (as shown in [30]);
(b) measuring data for fibres and matrix is difficult; however, more accurate inputs for material properties are needed:

    (i) single-fibre tensile tests are affected by stress concentrations at the grips while single-fibre fragmentation tests make use of assumptions on the fibre-matrix stress transfer; more reliable methods that can lead to a more accurate single-fibre strength distribution are needed;
    (ii) a simple Weibull distribution might not be sufficient in describing the fibre strength variability, particularly related to small scale cases [50];
    (iii) matrix properties are size dependent [115, 116]; bulk matrix properties may differ from the matrix properties in a composite with a high fibre volume fraction: changing the matrix behaviour from elastic to plastic in the direct numerical simulation model has led to strong differences in terms of fibre break accumulation behaviour. Capturing the correct matrix properties and behaviour might have a strong role in composite failure;

(c) given the importance of large n-plets in the failure events, capturing the interaction process between fibre breaks:

    (i) more studies are required detailing values for the ineffective length, as well as on the distance within which fibre breaks interact; studies should be performed that mapped the stress/strain in fibre break local sites, e.g. using Raman spectroscopy or digital volume correlation (DVC) methods;
    (ii) (ii) the great majority of n-plets are seen to appear instantaneously in the CT scans; techniques such as acoustic emission monitoring should be used to capture the timescale of this phenomenon; this is of great importance as the majority of the models predict a progressive formation of n-plets; dynamic effects might have a role in this, as the dynamic stress fields related to the fibre break formation are of significant difference from those considered in the quasi-static hypothesis;

(d) real micro-structure features to be considered, such as fibre misorientation and waviness, void presence, large resin rich regions are likely to have an effect in the strength predictions are not incorporated in the models yet.

The great discrepancy observed in the n-plet formations could be potentially related to the dynamic effects that are ignored in the assessed models [32], and that might have a strong impact on the coalescence of fibre breaks, as cause of stress fields around fibre breaks of significantly different intensity and duration from those considered in the quasi-static case.

As noted earlier, the problem of dynamic stress concentration due to fibre failure in a composite sheet was introduced by Hedgepeth [83] using the shear-lag approach and modelling the stress concentration at the plane of fibre failure, finding that the maximum stress concentration factor was distinctly higher than in the static case. Ji *et al.* in [117] more recently modelled the dynamic stress concentration factors along the entire length of a fibre neighbouring a broken one, using the same classical shear-lag approach. It was found that the dynamic effects are significant for a very short time scale, dependent on the mass-per-unit-area of the fibre, the fibre diameter and the shear stiffness of the matrix. The associated considerations were introduced in FE models only in the recent years (from 2017 onwards). A brief overview of these models is presented in the next section.

2.4.4 The dynamic progression of events after a fibre fracture

While many contemporary models describe the stress redistribution around a broken fibre as a static equilibrium problem, the fibre failure process can usefully be treated as a dynamic process; the elastic strain energy accumulated by the fibres is released as kinetic energy at rupture in the form of a stress wave that interacts with the fibres surrounding the broken one [83, 100, 117, 118].

Ganesh *et al.* presented an FE model validated using the analytical dynamic shear-lag solution proposed by Hedgepeth [83] and Ji [117].

The model showed the results associated to the stress redistribution after an S2 glass fibre failure for a 2D-planar array of fibres embedded in an epoxy matrix. The fibre and the matrix were modelled as linear-elastic and the interfacial debonding modelled using a traction law derived from micro-droplet experiments performed on the same composite system. Fibre and matrix were modelled as springs as reported for the FBM, and the SCF was defined as done by Swolfs *et al.* in [25].

A quasi-3D FE model with one element through the thickness was realised in which the fibre/matrix interface was modelled using surface-based cohesive contact formulation in ABAQUS. The results agreed with predictions by Hedgepeth, showing that the models that consider the shear-lag approach tend to under-predict the maximum SCF [14].

In 2019, Tavares *et al.* presented in [100] a geometrically 3D Spring Element Model (SEM) (based on the work of Okabe *et al.*, reported in [90, 97]), with a random distribution of fibres (that follows the work presented in [99]) that incorporates the dynamic effect related to fibre failure and shows how the dynamic aspect of the problem affects both the tensile behaviour and the multiplet formation in the longitudinal failure of unidirectional composites.

A periodic 3D Representative Volume Element (RVE) was generated that was constituted of transverse shear elements that connect the fibres made of longitudinal spring elements. To avoid dynamic instability of the system, mass and stiffness proportional damping was introduced, and for the fibre strength a unimodal Weibull distribution was adopted that considered as scaling length the length of the fibre element. The matrix behaviour was considered as both linear elastic and elastic perfectly plastic, as carried out in the direct numerical simulation model of crefsec:swolfs. To account for the time dependency in the system of equations of motion, a time integration scheme was adopted, that was based on the central difference method [119]. The authors demonstrated that modifying the magnitude of fibre volume fraction, matrix shear stiffness and fibre modulus did not affect the difference between the SCF in the dynamic case and the SCF in the static case, while both the dynamic and the static SCF absolute values varied with these properties. The primary factor affecting the increase in the SCF values was seen to be the matrix shear strength. In the case of an elasto-plastic matrix, an SCF increase of 43%, while it was almost double in the case of an elastic matrix, hence strongly affecting the multiplet formation and in general the material behaviour.

A snapshot of the stress in a broken fibre and its nearest neighbours, at about 13 ns after the moment of failure is reported in Fig. 2.12. The stress wave generated by the failure process produces a stress increase on the nearest neighbours in the plane of failure but also at an axial distance from it of ∼23 z/R, where z/R is the axial distance normalised to the nominal fibre radius. This can of course be identified with additional fibre failure on the considered plane, supporting the formation of diffuse multiplets (groups of neighbouring fibre breaks that are not on a same transversal plane, but a distance from each that is lower than the ineffective length). The study indicates that the individual fibre break density at peak stress is higher for the dynamic case, indicating the role that the stress wave may have in fibre break accumulation. The maximum SCF increase in the dynamic case is calculated and seen to increase with the multiplet size, as showed in other studies for the static case [120]. No clear change in the maximum size of the multiplet is extrapolated for the dynamic case. The multiplet formation is delayed (in terms of applied load) in the numerical results, if comparing to the experiments, as reported for the static case in [24]. A higher number of multiplets appear at lower strains, compared to the static case, for both the case of elastic and elasto-plastic matrices.

In this model that accounts for the dynamic effects in the fibre break formation, as in all the previous static models [26, 27, 101], there is still a large discrepancy between the predicted number of individual fibre breaks and multiplets prior to failure and what experimentally observed, with the final failure happening at a higher density of breaks than typically found in the experiments. The main achievement of the model can be retrieved in its finding that large multiplets may form at lower strain levels than predicted in static models.

2.4.5 Summary

Since the first fibre bundle model (FBM) presented in the 1950s [82], models have over time captured more complex phenomena occurring at a fibre-by-fibre level, and added more detailed inputs for the material properties to reach more accurate strength and fibre failure predictions. Although the computational advances have pushed much further the evolution and reliability of tensile models, to date many areas of improvement can be highlighted for more accurate predictive capabilities of the micromechanical models. Experimental exercises have been developed to provide more accurate data with which to validate the more and more complex models [12, 13, 92, 93, 113] and that highlight the large spread in the predictions of the different models available at the time. Bunsell *et al.* have focused in the last few years on the longitudinal tensile failure of unidirectional composites, simplifying the testing conditions and revealing the results of the experiments only after the models predictions were generated, avoiding model calibration bias to obtain results that

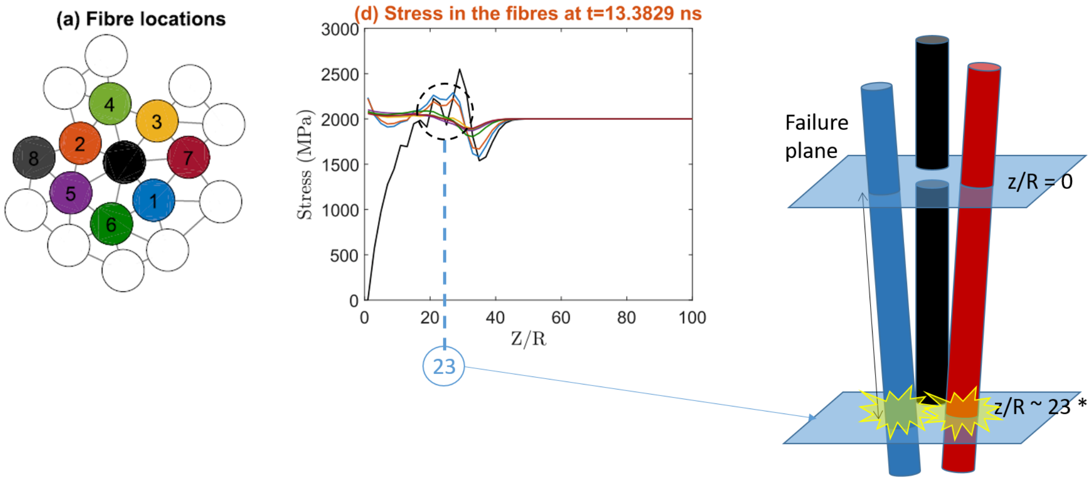

Figure 2.12. Tavares *et al.* [100]. The dynamic effects due to a fibre failure are shown: about 13 ns after the moment of fibre failure, the generated stress wave causes an over-stress on the nearest neighbours on the failure plane. At a distance of ∼23 z/R from the failure plane, the same fibres perceive a stress increase of ∼20%, while the broken fibre perceives an even a stronger increase, on a transversal plane slightly below. This stress increase on the plane z/R ∼ 23 from the failure plane could be cause of more fibre breakages.

could be close to the experimental ones.

The contemporary models for tensile failure of unidirectional composites (described in [24–27, 60, 98, 101, 104, 105, 111]) were tested against each other providing an overview of the discrepancies (on tensile strength and strain and accumulation of individual and adjacently grouped fibre breaks) that can be obtained when modelling the behaviour of the same material, using different assumptions. A further understanding of the features affecting the final failure, more accurate measurement of micro-mechanical properties for fibre, matrix and interface and the introduction of realistic features are the main suggestions that can be extracted from the study.

It was also indicated that the dynamic effects can be significant in the multiplet formation and hence in the cause of the final tensile failure of unidirectional composites. Spring models extended to the dynamic case showed the importance of treating the fibre failure as a dynamic process [100, 118]. Tavares *et al.* in particular, have shown that the dynamic consideration lead to a consistent increase in the maximum stress concentration factor (SCF) around a broken fibre. It was seen that the dynamic

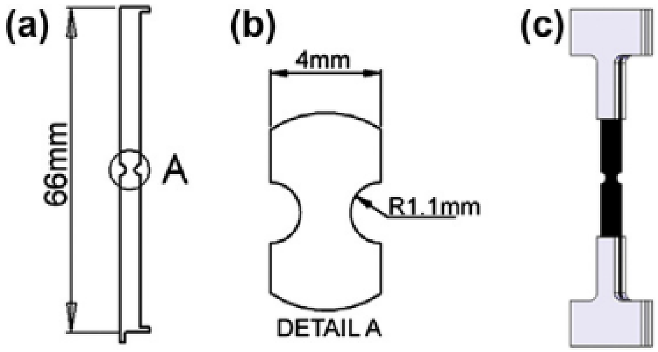

Figure 2.13. (a) The notched geometry of the specimen is indicated, with (b) the dimensions of the imaged region, and (c) the specimen ready for testing, with the adhesively bonded aluminium end tabs [126].

effects cause an earlier formation of large multiplets, as well as a higher individual fibre break density, if comparing to the static case, highlighting that dynamic effects should be kept into consideration when studying the tensile failure processes of unidirectional composites.

2.5 SRCT experimentation on tensile loaded CFRPs

Different techniques have been employed to capture the formation and progression of damage in composites, such as optical and scanning electron microscopy [19, 121], acoustic emission [122, 123] and ultrasonic C-scans [124, 125]. SRCT stands from these techniques for being non-invasive and having a resolution high enough to directly identify and quantify damage mechanisms, such as individual fibre breaks, matrix cracking, and other damage mechanisms, through time-resolved experiments in notched coupons.

This section aims at reporting what is available in the literature on *in situ* SRCT testing to understand the damage progression in carbon fibre laminates tensile loaded in the longitudinal direction. In these studies, the same geometry and composite layout has been used, following that reported in [127]: a 1 mm thick laminates made of aerospace grade level carbon fibre composites in a $(90/0)_2$ lay-out were water-jet cut to a notched geometry that allowed damage micro-mechanisms to be captured within the small field of view available using high resolution computed tomography, (see Fig. 2.13).

Wright *et al.* showed in [126, 127] the impact and the potential advantages of using Synchrotron Radiation Computed Tomography (SRCT) in carbon fibre epoxy reinforced coupons. The work showed that within the adopted double notched specimen geometry, it is possible to identify different damage modes and that the extracted information can be used to support model development and validation.

Scott *et al.* in [22, 112] showed that the fibre break accumulation can be followed from low to high stress levels and that the fibre break accumulation follows a power law curve, with a distinct acceleration prior to final failure of the specimen. No correlation was found between the fibre break locations and the transverse (90^o) plies cracks, suggesting the low influence of the transverse ply cracks on the fibre failure for this geometry. Scott showed in [34] how different manufacturing methods can lead to different failure mechanisms. In the notched coupons, a decoupling phenomenon was identified, due to delamination and 0^o splits that isolated the central 0^o layers, occurring at lower stress levels than those causing the spike in the fibre break accumulation. Scott's work was the first to show the presence of large multiplets in tensile (90^o) plies [22].

Morton *et al.* in [23] investigated for the first time the effect of fibre, matrix and interfacial properties on the initiation and accumulation of fibre breaks, using SRCT. It was observed that the fibre and matrix moduli had little effect on the accumulation of individual breaks (for the systems tested), as well on the geometry of interacting breaks. The accumulation trend was seen to not be strongly influenced by the Weibull strength moduli. Following the observations of Scott *et al.*, it was confirmed that groups of interacting fibre breaks formed within one load step, suggesting a dynamic role in the formation of such features. Different multiplet patterns were observed, not solely dependent on manufacturing methods. Individual fibre breaks formation was seen to be influenced by the fibre volume fraction and the presence of voids (with the latter also proven by Scott *et al.* in [128]). It was concluded that the fibre/matrix interface and hence the resultant stress transfer properties, have a role in driving the damage initiation and propagation in the tested composite geometry and reliable testing procedures are needed to evaluate the stress transfer in the bulk of composites at realistic volume fractions.

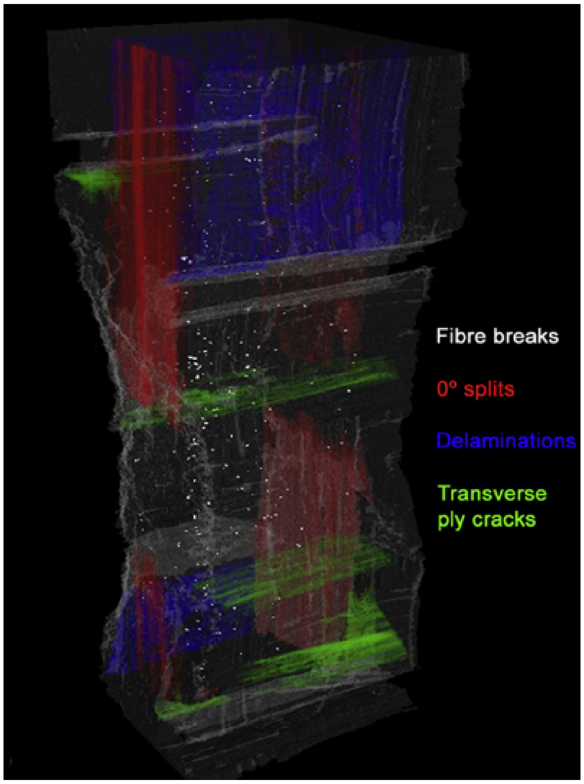

Figure 2.14. 3D segmented damage in a coupon, at 94% UTS of failure, with the composite bulk rendered semi-transparent. The fibre failure is the damage mode occurring at the highest stress levels, after a decoupling has isolated the central 0^o from the external transverse (90^o) plies [22].

Garcea *et al.* in [31] analysed fibre break accumulation using continuous monotonic tensile loading coupled to continuous scanning, rather than step-wise scanning with hold-at-load performed by Scott and Morton in [22, 23, 112]. Fibre break accumulation was followed up to 99.9% UTS, as opposed to 94% UTS in Scott *et al.* and showed to follow a power law curve until the very last moment preceding the macroscopic failure. It was confirmed that the great majority of fibre breaks is associated to new locations rather than occurring near pre-damaged sites. Within the 2 mm of length analysed for example, only one fibre was observed to fragment multiple times (breaking eight times), while from all the 14,000 fibres observed, none failed more than four times. The 2 ms exposure and 500 projections collected by Garcea *at al.* for each tomograph with a voxel size of 1.1 μm, led to a compromise in terms of image quality. Uninterrupted tensile loading showed that the fibre break accumulation phenomenon can be approximated by a power-law relationship until the very last moment preceding final failure, but while fibre breaks could be easily distinguished, an automated fibre-by-fibre detection approach with a contained level of error was not have been possible.

2.5.1 Summary

To the author's knowledge, Wright and Scott's works were the first to use SRCT to understand in situ the damage initiation and progression in CFRP laminates. The use of SRCT allowed the damage to be tracked in simulated working conditions at a high resolution, showing distinctively what are the main damage modes leading to final failure. From these works analysis has been extended to a range of fibre/matrix combinations and analyse in further detail how fibre breaks accumulate and how this accumulation is influenced by the material parameters. This was partially achieved by Morton's work, which showed little correlation between fibre/matrix moduli and the fibre break accumulation, suggesting a stronger influence of the Weibull and interfacial parameters. The work concluded with the suggestion of more effort should be put towards the measurement and calculation of interfacial properties and related stress transfer properties. Garcea's work proved that a power law curve can be used to estimate the fibre break accumulation until 99.9% UTS and that continuous monotonic tensile loading coupled to continuous scanning can be adopted to track the fibre break accumulation. However, by adopting this technique, lower quality scans are obtained that are a challenge to automated extraction of micro-structural features (as sought within the current work).

2.6 Conclusions from the literature

The failure of tensile loaded composite laminates is a complex phenomenon that involves multiple interacting damage mechanisms. The level of adhesion between fibre and matrix has a fundamental role in the damage formation and propagation and can be influenced by the fibre manufacturing methodology. Carbon fibres are brittle by nature and vary in strength significantly, hence a strength distribution, such as the Weibull distribution, has to be adopted to describe the strength variation.

However, the accuracy of the Weibull parameters is strongly affected by the testing methodology, the gauge length adopted and the number of specimens tested. It has been identified that greater higher accuracy is needed in determining such parameters. As a consequence, modelling the failure of a tensile loaded composite laminate is not a simple task. The work of Cox, Hedgepeth and Van-Dyke, Zweben and Rosen, Beyerlein and Phoenix, Zhou and Curtin, Landis and Okabe have set the understanding of the problem, leaving open questions, on what the real mechanisms controlling the final failure in real composites with thousands of fibres embedded in a matrix are. Contemporary models based on the previous efforts show different ways to approach the problem, using the recent technologies to understand the tensile failure of real composite micro-structures. While the strength and strain seem to be better predicted (as demonstrated by experimental exercises such as [32]]), there still is a lack of understanding in the micro-mechanisms leading to final failure, particularly regarding the formation of groups of interacting fibre breaks. Previous studies performed using SRCT to understand the damage progression in tensile loaded CFRPs have shown the ability of discerning different damage mechanisms happening within the bulk of the material, and particularly focusing on the fibre fracture failure mode, how this is influenced by the material parameters. Fibre breaks have been found to accumulate on a power law curve, as a function of the applied load and this has been shown up to 99.9% UTS. From the literature it can be seen that there is a need to analyse in more details the interaction between fibre breaks in representative CFRPs. Bunsell *et al.* in [32] have identified a number of gaps in the literature that need to be filled. In particular, picked in the current study are: the repeatability of the tests to account for the variability of response of the tested materials at a micro-scale, systematics variations within the same material (such as the fibre/matrix interface, fibre diameter, etc.), detailed analysis on multiplet accumulation and morphology prior to failure, where the model predictions start to be inaccurate, and the analysis of the influence of real micro-structural features, such as the fibre misorientation and the local fibre volume fraction.

CHAPTER 3

X-RAY COMPUTED TOMOGRAPHY

In this chapter, a brief overview of the X-ray computed tomography is presented. The basic principles behind the technique are illustrated, with examples of typical artefacts that can be seen in CT images. The advantages and disadvantages of adopting synchrotron radiation CT over laboratory-CT are shown, as well as the two mostly adopted modes to perform tomography, i.e. absorption and in-line phase-contrast imaging, and the reasons why the first mode has been preferred over the second in the current work. In situ damage accumulation detection in composite materials allows to examine the internal structure of components without laborious sectioning. Different testing (and acquisition) strategies can be chosen, such as ex situ, interrupted in situ and continuous streaming; the reasons for having chosen the interrupted approach for the current study are presented.

3.1 Background

High-resolution X-ray Computed Tomography (CT) has received extensive interest, being a powerful tool for estimating internal characteristics of materials and their behaviour [129–131]. X-Ray CT is characterised by an X-ray source and an array detector with the sample placed between the two. 2D radiographs are collected while the sample is rotating around a fixed axis. The photoelectric absorption and the incoherent Compton scattering are the two dominating processes of X-ray interaction with the condensed matter [132]. Depending on its material characteristics of linear attenuation, the sample will allow the X-ray beam to be transmitted though itself with a certain intensity distribution. This intensity distribution is measured by the detector and the Beer-Lambert law can be used to describe it:

$$I = I_0 exp^{-\mu L} \tag{3.1}$$

In the domain of the photoelectric absorption, the linear X-ray attenuation coefficient µ can be expressed as:

$$\mu(x, y, z) = K\rho\frac{Z^4}{E^3} \tag{3.2}$$

According to the Beer-Lambert law, the ratio of the number of transmitted to incident photons is related to the integral of the linear X-ray attenuation coefficient μ of the material along the path that the photons follow through the sample[133]. Parameters related to the X-ray beam are I and I_0, transmitted and incident beam intensity and E, the incident photons energy; L is the sample thickness. Material parameters are the density ρ and the atomic number Z; K is a constant. Hence, the beam intensity through the material decreases exponentially by an amount dependent on the beam energy (the higher the energy, the lower is the decrease in beam intensity) and on the material properties; if the material density or the atomic number increases, the beam intensity will decrease faster through the thickness. With the assumption of the incident and the transmitted X-ray energy being measured quantities, the absorption can be extracted from Eq. (3.1) as:

$$\tau = \mu L = ln\frac{I_0}{I} \tag{3.3}$$

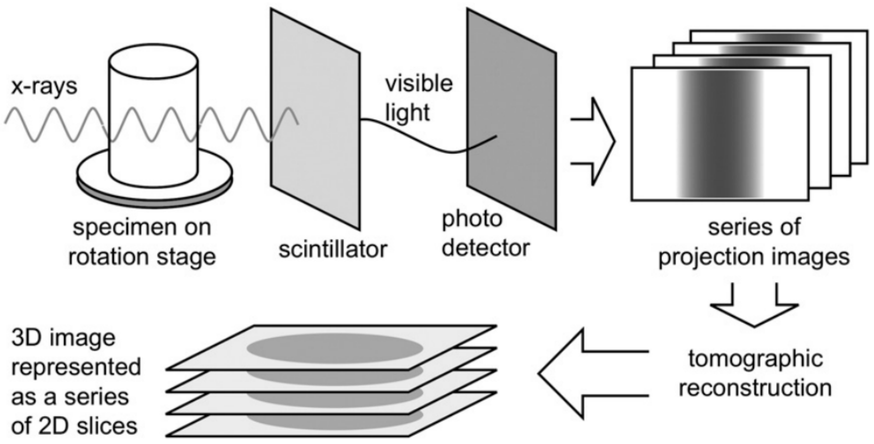

Figure 3.1. Schematic illustration of the X-ray CT acquisition and reconstruction workflow. The 3D volume of the scanned sample is obtained through the mathematical reconstruction of a series of X-ray projection images [137].

Attenuation by Compton scattering is the second most important absorption process, becoming prevailing with respect to the photon absorption when the atomic numbers Z increase; more details on it can be found elsewhere [132, 134, 135].

The transmitted intensity for a specific section of the sample is indicated as projection. The resultant collected image is a superimposition of a 3D volume on a 2D plane. Hence, to obtain 3D information a large number of radiographs are collected, while the sample is rotating. From this series of radiographs, algorithms are used to reconstruct the volume of the sample (see Section 3.2) [136]. A schematic representation of this is reported in Fig. 3.2.

Conventional CT scanners employ X-ray tube sources in which electrons are accelerated and allowed to collide with a target producing Bremsstrahlung radiation [137]. An appropriate scintillation is needed to convert the X-rays into visible light, and photodetectors to produce a digital image. First-generation scanners, based on the original idea of Sir Godfrey Hounsfield, were based on the 'translate-rotate' principle [138]: the X-ray tube and detector would translate across one transversal plane of the sample, than rotate of a small amount, and translate again. The system was indicated as 'pencil beam system' [139]. Earlier CT scanners used a linear array of photodetectors, i.e. one projection image was generated by the acquisition and the reconstruction of one plane at a time (fan beam, Fig. 3.2a). The development of

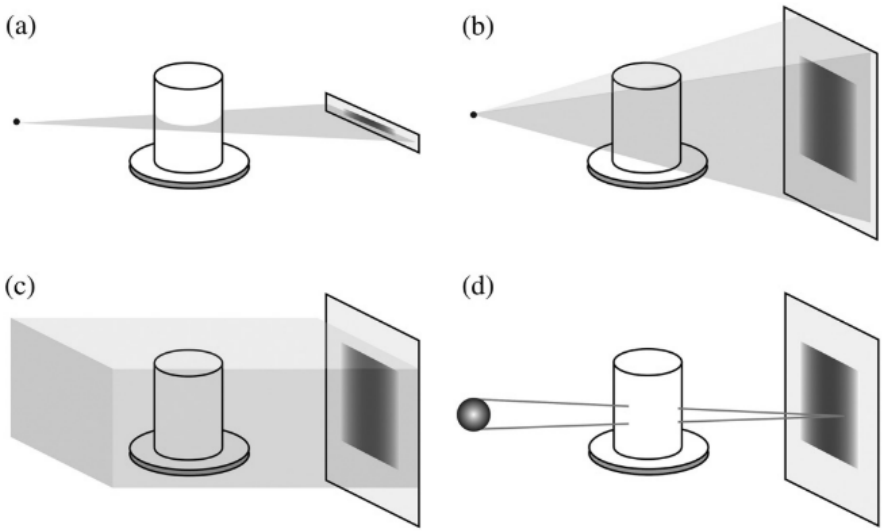

Figure 3.2. X-ray CT acquisition configurations. (a) shows an example of a fan beam (projection image is generated one slice at a time); (b) and (c) illustrate the cone beam and parallel beam configurations: 2D projection images are collected in a single step. In (d), the example of a large X-ray source. The intensity collected by a pixel could be related to ray coming through different paths, rather than a specific trajectory, leading to blurring in the projection image [137].

2D detectors allowed the acquisition of 2D projection images (cone beam Fig. 3.2b and parallel beam in Fig. 3.2c), reducing the scanning times. The conical shape generated by the beam (along with the characteristics of the detector), typically define the spatial resolution of the conventional CT systems [137]. Hence, a fundamental role is played by the spot size: the smaller this is, the smaller the penumbral blurring generated, leading to a more accurate projected image. Having a large spot (Fig. 3.2d) means that different ray paths through the sample could have been undertaken by a photon detected by a specific pixel, i.e. the intensity acquired by a pixel is formed by rays coming from different paths. As a consequence, geometrical unsharpness is added to the tomographic reconstructions. Hence, typical CT systems adopt micro-focus X-ray sources with spot sizes on the order of the tens of micro-metres or less [137].

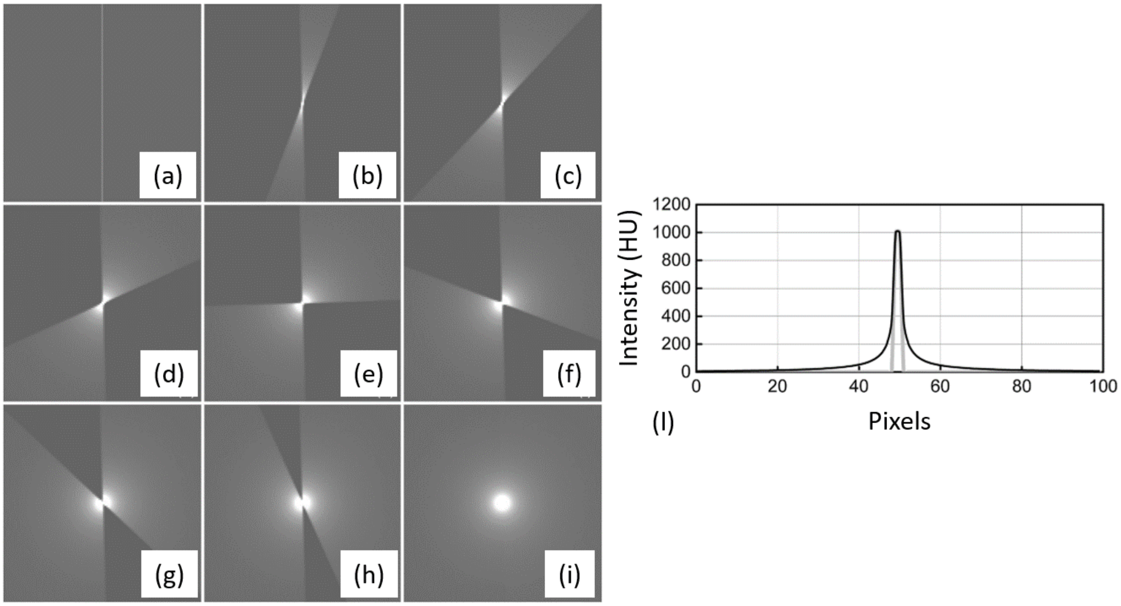

Figure 3.3. Backprojection process for a single point. In (a) the backprojected image of a single projection is shown. In (b) to (i) are reported the backprojections of the views covering respectively the angles 0 to 22.5 deg (b), 45 deg (c), 67.5 deg (d), 90 deg (e), 112.5 deg (f), 135 deg (g), 157.5 deg (h), 180 deg (i). In (l), the profile of a reconstructed point is indicated: in black, the reconstruction with backprojection; in grey, the ideal reconstruction [140].

3.2 CT reconstructions and imaging artefacts

After the projections are acquired, the data is reconstructed to obtain a 3D volume using appropriate algorithms, such as the Filtered Back Projection Reconstruction (FBP). An intuitive explanation of this concept of backprojection is shown in Fig. 3.3. The scanned sample is an isolated point; one X-ray projection is not enough to describe the position of the attenuating point. Additional X-ray paths are needed: by having more angular positions, it is possible to localise its position. Each projection will have an impulse function with the peak positioned where the X-ray met the sample (Figure 3l). Starting from the intensity function obtained for each projection, the algorithm provides a visual 2D representation of the object by backprojecting over a range of 180 deg. As shown in Figure 3i, the object has been identified but appears blurred.

The backprojection-filtering approach consists of filtering (convolving) the backprojected images using the inverse of the impulse response [140]. The convolution process corrects the blurring providing a more definite image. The 3D equivalent of a pixel, the voxel, is a critical factor affecting the quality of CT images. Indeed, the spatial resolution defines the smallest gap between two points at which they can still be recognized. It depends on different factors, e.g. the quality of the mechanical system (i.e. accuracy of the back projected views) and the X-ray optics, which define the level of details one can achieve.

The quality of the images obtained by computed tomography (CT) can be affected by artefacts. Methods to inspect causes of artefacts in synchrotron micro-tomography are retrievable in the literature [141]. Sources of artefacts can be lack of data, which can cause the aliasing distortions and misalignment between the sample and the camera, caused by the drift of the calibration parameters while the angular scans are taken, an example is shown in Fig. 3.4a. Other causes are limited field of view (see Fig. 3.4b for an example, sample is bigger than the detector) or beam hardening: which is related to the use of a polychromatic X-ray source and is caused by a non-uniform beam energy distribution, which is associated to higher energy X-ray beams absorbed less easily than lower energy beams. As shown in the example of Fig. 3.4d, this can lead to the object edges being more pronounced without the presence of a density gradient.

Lastly, ring artefacts are dark or bright rings. A CCD detector presents pixels not uniform in sensitivity. By subtracting a dark image and normalising using an image obtained with the same settings but without the sample, a flat-field correction can be applied to the projections. The flat-field correction are not enough to cancel the effect, which produces ring artefacts (Fig. 3.4c). Usually this is corrected by the use of filters. However, rings cannot be simply decreased when temporal and spatial beam intensity fluctuations occur [142]. Beam attenuation is the typical approach to produce an image with X-rays, but the transmitted wave optical phase can be used also. Objects in images reconstructed by phase contrast usually present fringes at the edges. Although this is an advantage of the technique, this can also become a source of artefacts.

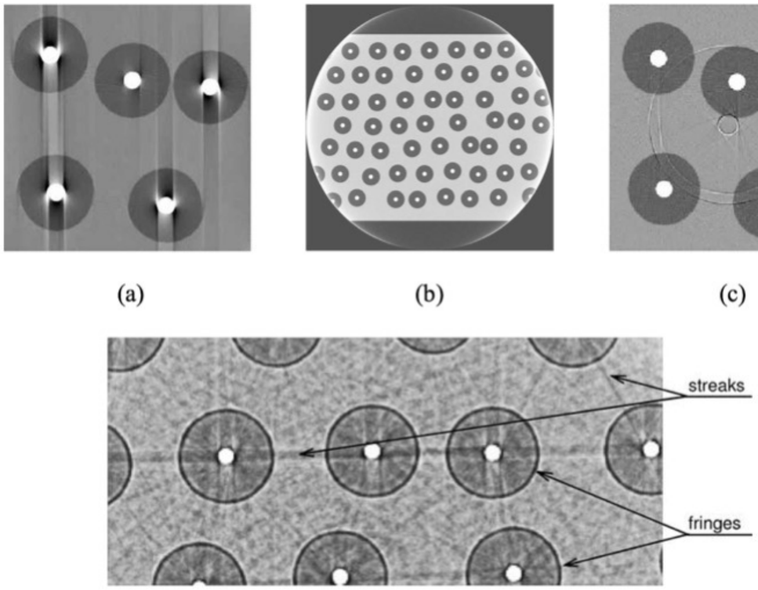

(a) (b) (c)

(d)

Figure 3.4. Examples of imaging artefacts; (a) example of lack of data causing drift of the calibration parameters while the angular scans are collected; (b) limited field of view, with sample being bigger than the detector; (c) example of ring artefacts; (d) example of beam hardening, caused by a not uniform beam energy distribution. Object edges appears more pronounced than they are [142].

3.3 Synchrotron radiation-CT and laboratory-CT

Micro-focus computed tomography scanning can be used successfully for assessing damage in composite components [34]. X-rays are generated by a molybdenum or tungsten target hit by an accelerated electron beam and the obtained beam is polychromatic and divergent (conical beam effect). Synchrotron radiation tomography offers a very high intensity beam with the use of a smaller source: third generation synchrotrons can generate more than 1000 times higher flux than micro-focus tubes [133]. Synchrotron radiation is characterised by electrons accelerated and diverted into a magnetic field to achieve X-rays. In this case, the beam is relatively coherent, monochromatic and parallel and orders of magnitude brighter. This affects the image quality and the acquisition time. Although recent laboratory CT systems have reduced the gap with SRCT regarding spatial resolution (now below 1μm in both cases) and phase contrast (obtainable to some extent with lab-CT), high temporal resolution and signal to noise ratio are still main features of SRCT, making this method a key tool for in situ testing [143]. On the other hand, while synchrotron sources are limited to the extent of the parallel beam (typically less than 50 mm), lab-CT systems allow larger parts to be scanned and multi-scale approaches to be adopted. The cone beam geometry of most lab-CT systems translates into higher resolutions achievable when reducing the source to sample distance. Accommodating in situ rigs often means this distance has to be increased with resulting resolution reductions. The parallel beam of synchrotron sources leads to the resolution not depending on the source to sample distance [143].

3.4 Absorption and in-line phase-contrast imaging

Two modes to perform tomography are widely adopted to study the damage evolution in polymer composites: the absorption mode and the phase contrast mode [143]. In the absorption mode the contrast is obtained by the difference between μ_1 and μ_2 of the two phases, i.e. the atomic numbers of the elements and the density. To a certain extent, a larger difference will allow an easier image analysis of the scanned sample [133]. In the case of a synchrotron radiation source, phase effects related to the propagation from the sample to detector are avoided by placing the sample close to the detector. Too high a transmission causes low contrast between the elements, while a low transmission leads to bad photon statistics, with an optimal value being at about 10% [144, 145]. If the beam is monochromatic, beam hardening is avoided and quantitative analysis is possible as the grey level is directly related to the linear attenuation coefficient μ, hence linked to the atomic number and the density of the scanned sample [133].

Phase imaging [146] allows the contrast between phases that attenuate the beam similarly to be increased, e.g. soft solids and fossils [147]. The enhanced edge contrast translates into edges being easier to segment, enabling quantitative information retrieval from low contrast micro-structures that could not be achieved with attenuation contrast [148]. Different phase contrast methods are available and described elsewhere [149]; in-line (or propagation) phase contrast imaging is described here for being the simplest X-ray phase-contrast method and widely adopted with synchrotron sources [150]. It exploits the Fresnel diffraction of X-rays to enhance the visibility of boundaries within a sample [148]. Requirements for the method are: (i) X-ray beam has high spatial coherence, which is easy to be obtained with a synchrotron source or a very small source size (on the order of microns) and (ii) a significant sample to detector distance should be provided. This allows the following: the presence of the sample distorts the X-ray wavefront. The propagation of the distorted X-ray wavefront between the sample and the detector provides the Fresnel diffraction fringes in the image (see Fig. 3.4) [150]. The intensity of the phase-contrast fringes increases with the sample to detector distance (R2 in Fig. 3.4), in the synchrotron parallel beam case; fringes broaden and the imaging regime moves from the near-field, edge-enhanced mode adopted in most phase-contrast imaging to the intermediate regime where more diffraction fringes are obtained, as done in the holotomography method [151].

Phase-contrast images are commonly edge enhanced, which means the image intensity is no longer directly linked to the thickness of the sample: the lowest and the highest intensities are typically observed in the fringes of the edges or any internal boundaries of the sample [150]. To extract quantitative information (and provide a better input to the reconstruction algorithm), a phase-retrieval step is performed that recovers the original phase-shift given by the presence of the sample on the X-ray wavefront, immediately after its position. The phase-retrieval process may require the same sample to be scanned at multiple values of the sample to detector distance, with the magnitude of the phase contrast increasing with the distance [152]. The Paganin solution [153]., based on a specific filtering of the projections, is often adopted to avoid collecting multiple images [148]. Synchrotron sources are particularly suited for the algorithm for their highly coherent beams, but applications of phase retrieval using laboratory-CT for imaging are available in the literature [154].

Fig. 3.5 shows cross-sections of two different in situ tested carbon fibre coupons extracted from [31] (Fig. 3.5a,b) and [143] (Fig. 3.5c) using synchrotron sources. For both coupons, scans were acquired in the near-field Fresnel regime, but Fig. 3.5a was reconstructed using conventional X-ray attenuation and Fig. 3.5b,c using Paganin. The same GRIDREC/FFT algorithm was employed for the tomographic reconstructions [155] and no image post processing was applied. The Paganin algorithm has not

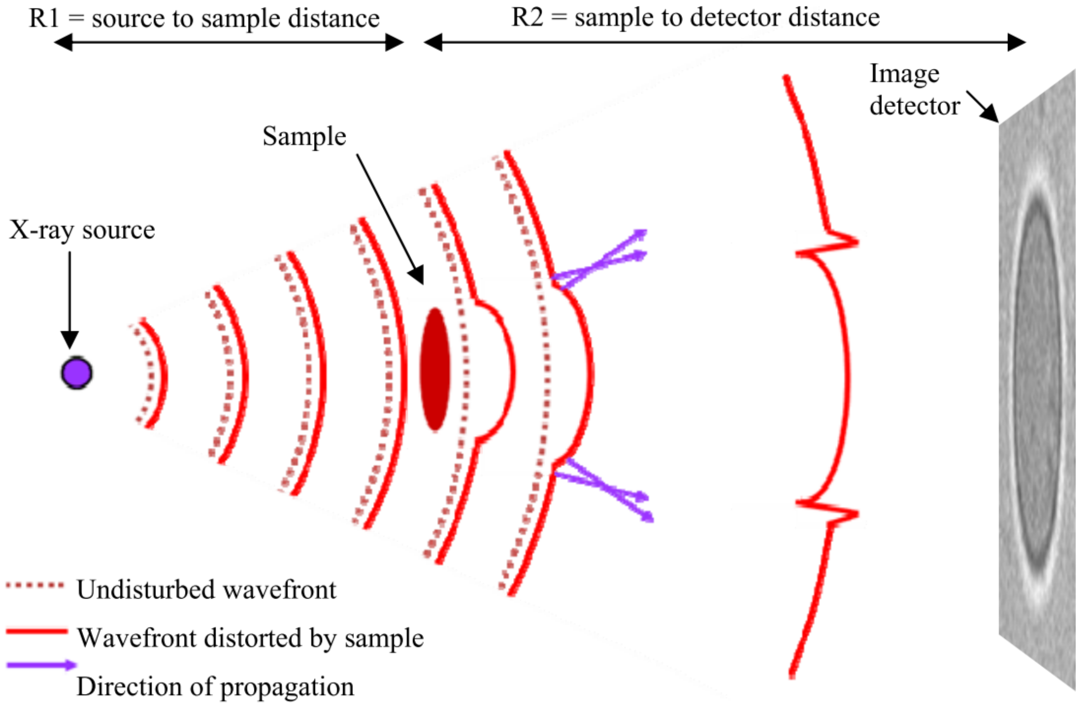

Figure 3.5. In-line phase contrast mechanisms explained for the cone-beam geometry. The phase-shift due to the sample being in the X-ray path, distorts its wavefront, giving the Fresnel diffraction fringes in the image. The synchrotron wavefront is approximately planar but the mechanism is the same [150].

enhanced the crack edges in the case of very small features, such as fibre breaks, while compromising sharpness (see Fig. 3.5b), but facilitated the segmentation of wider cracks, such as matrix cracks or large groups of fibre breaks, as shown in Fig. 3.5c.

Hence, even though phase retrieval is widely adopted for damage detection when in situ testing composites, absorption-based reconstructions have been used in this work, focused on the analysis of single fibre breaks and small groups of fibre breaks (up to six adjacent fibre breaks have been observed in the current work, as shown in Chapter 5).

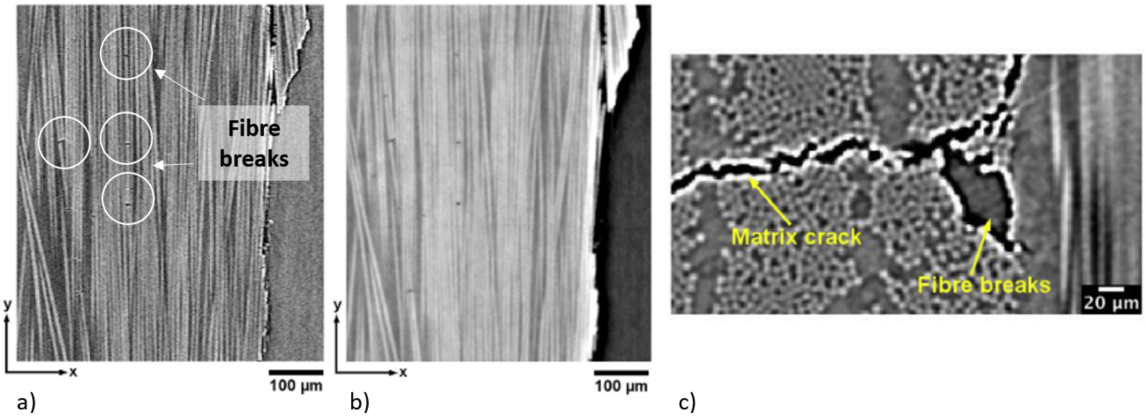

Figure 3.6. Cross-sections of a tensile tested carbon fibre composite coupon. Scans are reconstructed under absorption mode in (a) and Paganin mode in (b,c). Paganin mode has not provided any small crack detection enhancement (similar level of detectability in (a) and (b)), while the edges of matrix cracks and very large groups of fibre breaks are particularly enhanced, as shown in (c) [31, 143].

3.5 Ex situ, interrupted CT and continuous in situ CT

In recent years, the use of X-ray computed tomography for fibre architecture inspection and manufacturing defects and in situ damage accumulation detection in composite materials has gained more and more importance, allowing users to examine the internal structure of components without laborious sectioning, and the associated risk of causing further damage introduction.

Both ex situ and in situ imaging can be performed in a time-lapse manner on the same sample [156]. In an ex situ experiment, the sample is removed from the rig/chamber before scanning and placed on the stage of the X-ray CT setup and the acquisition strategy follows that shown in Fig. 3.6a. In an in situ experiment the sample is imaged under load/heat using a rig that is mounted on the X-ray CT stage. Advantages of the in situ approach rely on not having to move the sample from the rig/chamber to perform each scan, avoiding environmental changes as well as damage introduction. Moreover, features such as transverse cracks in tensile testing tend to close when load is completely removed, becoming more difficult to be resolved from CT scans [157]. In the interrupted in situ imaging, stress relaxation can occur (as

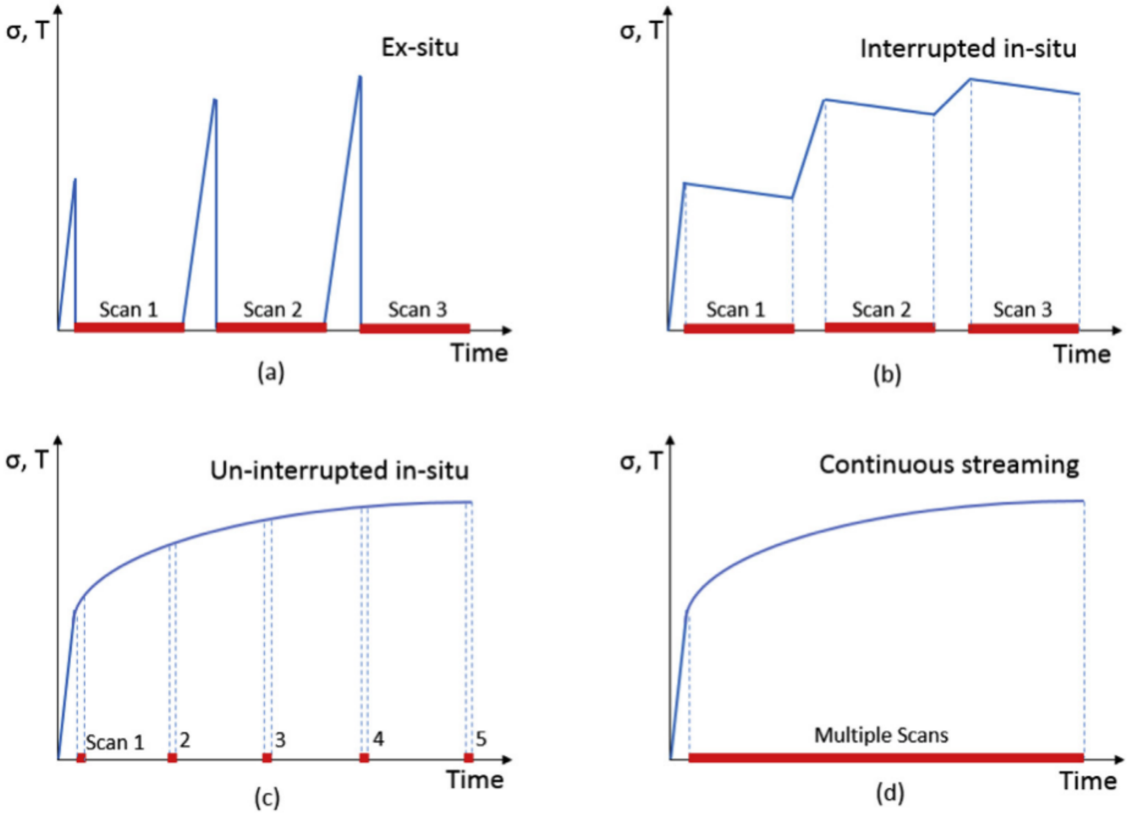

Figure 3.7. Temporal X-ray CT acquisition strategies (in red) to follow a tensile test or heating cycle (in blue) [143].

shown in Fig. 3.6b). Hence, an interrupted imaging approach with load reduction to levels that reduce any stress relaxations within the material before scanning is adopted in this work, allowing high quality scans to be collected and features such as individual fibres to be tracked and segmented from low contrast images with high levels of fidelity. In synchrotron facilities, continuous streaming of projections is being more and more adopted, allowing continuous imaging (Fig. 3.6d). However, if the time scale of damage evolution is much smaller than the duration of the tomogram acquisition the technique might not be useful and an interrupted approach preferred instead. A reduction in the number of projections per tomogram and an increase in the flux represent a possible solution to the issue [157]. However, this often leads to lower quality scans for which extracting particularly small features becomes challenging.

3.6 Conclusions

Currently, all the material characterisation techniques are affected by limitations. With X-ray micro-tomography limitations to be mentioned are the penetrating ability of the X-ray due to the material density of the scanned sample (in the case of dense material, very high-energy X-ray or very small specimens are typically adopted) and the limited ability to differentiate material phases with large differences in X-ray absorptions. In this case, the less absorptive phase would exhibit a very poor contrast. In the case of synchrotron X-ray sources, the availability of the facilities can be added to the limitations [136].

The main advantages of the technique can be summarised as allowing the non-destructive evaluation of internal material features that are imaged in three dimensions at relatively high spatial resolution. Quantitative measurements can be made: spatial distribution and the volume fraction of phases, as well as the evaluation of the variations in the phases due to mechanical or chemical phenomena [158]. Techniques such as Digital Volume Correlation (DVC) can be used to extract from the 3D images quantitative information on the displacement and strain distributions in heterogeneous materials under different loading conditions [159].

Even if the recent developments of the laboratory CT systems are reducing the gaps existing between laboratory- and synchrotron-CT, the latter will keep its unique characteristics: a combination of a high-speed detector, high flux X-ray beam and fast reconstruction algorithms can lead to 3D images being able to follow the effect on phases of mechanical or chemical testing with a level of details not achievable before.

(This page was intentionally left blank)

CHAPTER 4

FIBRE/MATRIX INTERFACE EFFECTS ON FIBRE FAILURE

In situ synchrotron radiation computed tomography (SRCT) has been used to compare the fibre damage progression in five configurations of $(90_2/0_2)_s$ *carbon-epoxy notched coupons loaded to failure. To the authors knowledge, this represents the first study in which the effects of different sizing types, surface treatments and fibre diameters on the macroscopic properties of the materials, e.g. ultimate tensile strength (UTS), and on the damage accumulation at a microscopic scale, e.g. fibre break accumulation, are assessed with particular focus to the formation of groups of interacting fibre breaks (multiplets), believed to drive the final failure events. A semi-automated approach has been adopted to process the large amount of data obtained from the SRCT scans to assess the fibre break development and further areas of applicability of the method can be envisaged. For the material tests, single fibre break accumulation was seen to be influenced by the fibre diameter and the fibre type, but not the surface treatment and the sizing type, which was seen to influence the formation of groups of interacting breaks. For the material configurations presented, it can be suggested that an increased defect tolerance can be obtained by moving from stronger to weaker fibre/matrix adhesion, with sub-critical multiplet behaviour emerging as independent of the average UTS value.*

4.1 Introduction

Accurate prediction of failure behaviour in composite laminates remains a topic of ongoing research [32]. Tensile failure of longitudinal unidirectional (UD) layers often represents the limiting factor in the ultimate tensile strength (UTS) of multi-layered composites, and has been widely discussed within the literature [14]. Analytical, statistical and finite element (FE) models are reported [26, 27, 40, 48, 76, 84, 86, 101, 105, 112, 160, 161], that often use the concept of a localised critical damage site controlling final catastrophic failure. Such a site is believed to be formed by a number of neighbouring fibres failing as a mechanically coupled group, guided primarily by the distribution of strength of the individual fibres and the stress concentration that occurs around broken fibres. When studying the tensile failure of unidirectional composites, the strength of the fibres is recognised to have a stochastic distribution, related to the presence of flaws, as first identified by Griffith in the early 1920's [36]. Many studies have focused on the characterisation of the fibre strength, using different approaches mainly based on the Weibull strength distribution [41, 42]. A development of this approach was proposed by Curtin in [45], who introduced the Weibull of Weibulls (WOW) model that proposes a strength distribution along a fibre to describe the presence of flaws, while a different distribution is adopted to assign to each fibre a characteristic strength value. This to account for the damage introduced during processing and handling of the fibres, and arguably represents a more physically realistic approach than a single distribution.

The second key parameter in studying the longitudinal tensile failure of composites is the stress concentration around fibre breaks. When a fibre breaks, load is transferred onto the surrounding fibres, eventually leading to the formation of groups of interacting fibre breaks (multiplets). Failure is presumed to occur by a critical multiplet acting as a crack unstably propagating and causing the failure of the component [14, 22, 27, 32]. When a fibre breaks, the matrix is primarily loaded in shear and transfers the stress back onto the fibre [84, 85, 162]. The ineffective length is defined as the length over which the fibre carries a reduced stress either side of the break, and models exist in the literature to evaluate this length, such as Cox's shear-lag model [163]. Many modelling strategies have been proposed: whilst some have considered fibre failure to be an essentially static problem, others have considered time-dependant aspects both in terms of (a) viscoelastic matrix behaviour [28–30], and (b) the dynamics of the fibre break [100, 164]. Previous synchrotron radiation computed tomography (SRCT) studies have adopted in situ testing to quantify the fibre failure progression in carbon fibre reinforced polymers (CFRPs) [22, 24, 31], showing that the total number of breaks observed can be approximated by a power-law relationship and a significant numbers of interacting fibre breaks (multiplets) are associated with high stress levels, close to final failure of the coupons. Such experimental results have been compared to the model predictions and highlighted how the models commonly overestimate the stresses at which multiplets form [24, 32], even when the effects of the dynamic stress concentrations are considered [100]. This emphasises the difficulties in predicting multiplet formation. Planar multiplets were seen to 'pop-in' and not increase in number of fibre fractures involved for higher stresses [24], and this is shown up to ~99.9% ultimate tensile strength (UTS) in [31].

In the current study, fibre break accumulation activity in different cross-ply prepreg laminate configurations has been explored, with the fibres being subjected to two surface treatment types and two sizing types, providing different levels of adhesion to the same matrix system. Differences in break accumulation between two different diameter fibres are also presented. A semi-automated approach is adopted to isolate specific regions of the coupons and to analyse within those the damage progression from low to high strains. The variation in fibre break accumulation within and between different coupons cut from the same composite laminate is also investigated. The differences among the tested materials is presented in terms of macroscopic (average UTS) and microscopic properties, with particular focus on the diffuse and planar multiplets; features that are closely related to the final failure events. The significance of the planar multiplets with regard to tensile failure is not completely clear to the research community engaged in modelling fibre fracture and tensile strength, as represented in the published literature on the subject. While it is understood that single-fibre breaks are unlikely to be the controlling damage mechanism for tensile strength [14, 32, 164], it is contended that models for tensile strength, which explicitly include fibre failure should be able to predict the formation of singlets as well as the more important multiplets. The available model predictions of single fibre breaks, both individual and grouped, all show significant discrepancies from the experimental data. The present work is an original attempt to understand whether there are additional micro-structural factors that should be considered to improve the modelling capability.

4.2 Materials and experimental procedure

4.2.1 Materials

Five different material configurations are tested in the current study, with coupons cut from $(90_2/0_2)_s$ laminates produced from Mitsubishi Chemical Corporation (MCC) carbon fibre prepreg to the manufacturer's specifications; a summary of material configuration identifiers, prepreg grade, fibre diameters, sizing agent, surface treatment and resin type adopted is reported in Table 1. Two fibre types are tested, with diameter respectively of 5.8 and 5.4 μm. Two proprietary sizing agent types are used, with sizing agent 1 being reported to provide stronger adhesion to the matrix resin than 2. Two surface treatments were also tested, with I providing stronger adhesion than II. The resin used for all the material configurations in this study is an MCC 350 series, amine curing epoxy. Indicated in Table 4.2 are additional properties, such as the Weibull parameters for the fibres provided by MCC and the composite average UTS measured for the geometry tested. Two coupons were tested per material system, using 1 mm thick double-edge notched coupons, realised via water-jet cutting, following the approach of Wright et al. [127], see Fig. 4.1. Aluminium tabs were adhesively bonded to ensure alignment of the coupons during tensile loading in the electro-mechanical rig. About 8000 fibres are captured in the 0^o layers across the central notch region, with a gauge length of $\sim$1.3 mm being imaged in the field of view of the scans that were carried out during tensile testing to failure (see Fig. 4.1c).

4.2.2 Experimental procedure

Progressive *in situ* tensile tests to failure were performed at the European Synchrotron Radiation Facility (ESRF) in Grenoble, France (ID19 micro-tomography beamline). Following [22], tests have been performed using a modified DEBEN

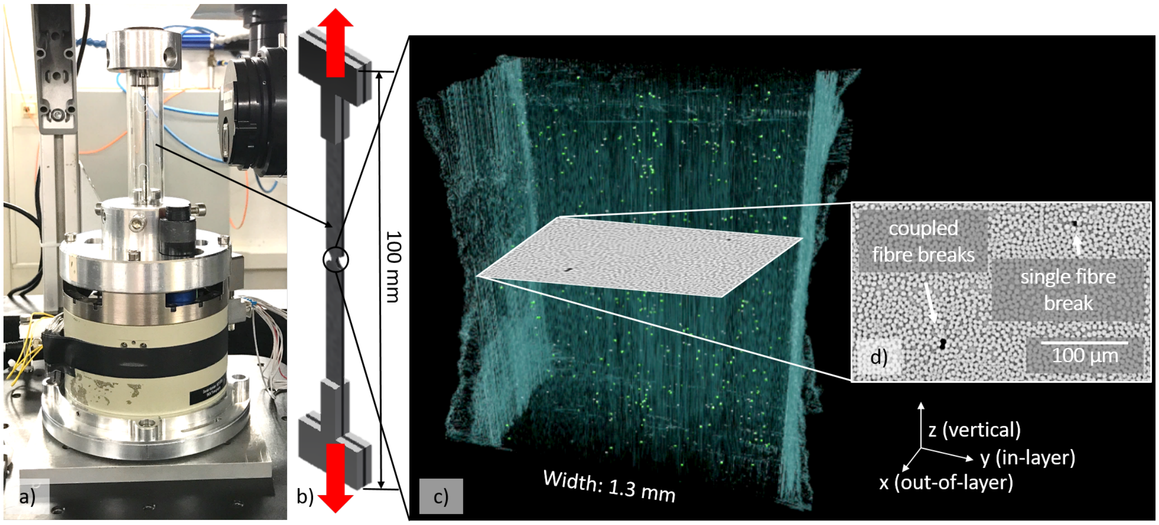

Figure 4.1. (a) Illustration of the compact loading rig on the experimentation stage at the synchrotron facilities, (b) coupon geometry, (c) a 3D representation of the imaged volumes for all the scans and (d) a top view of the features detected within the volume (single fibre breaks or groups of co-planar fibre breaks. In this case a singlet and a duplet are highlighted).

Table 4.1. Summary of the material configurations assessed in this work. Two carbon fibre types are used. Two sizing agent types (with type 1 providing stronger adhesion than type 2) and two surface treatment configurations are used, with type I stronger than type II.

Configuration	Fibre diameter (μm)	Sizing agent type	Surface treatment type	Resin
A	5.4	1	I	# 350 series, amine curing epoxy
B			II	
C		2	I	
D			II	
E	5.8	1	I	

CT5000$^{\circledR}$ tensile stage (Fig. 4.1a). The central notched region of the coupons (Fig. 4.1b) was initially scanned at between ~50% and ~80% of the expected UTS, with an average of eight more scans being collected between ~90% UTS and final tensile failure of the coupon. The number of scans collected per test varies somewhat due to the stochastic nature of composite strength. The individual scan duration was ∼2.5 min. A displacement rate of 0.2 mm/min was used between scans, with the tensile force on the coupon being reduced slightly (∼10%) while scanning, to promote sample stability during scanning. To ensure crack opening displacements at fibre breaks were well in excess of the voxel size, whilst maintaining a field of view large enough to perform a reasonable statistical evaluation of the data, a resolution of 0.65 μm was chosen for this study. A representative transverse SRCT slice of a single and two adjacent fibre breaks is highlighted in Fig. 4.1d. 2996 projections were collected per scan with an exposure time of 50 ms. A near-field Fresnel/edge enhancement regime was adopted at a coupon-to-detector propagation distance of 50 mm, using a multilayer monochromator (δE/E $\sim 10^{-2}$) at an energy of 19.5 kV. In-house software from ESRF was used for the tomographic reconstruction. In Fig. 4.1c, a scan collected immediately prior to macroscopic failure is shown (coupon C 1), highlighting the numbers of break events (typically in the order of 300 - 500) seen at this point within a scan volume (light green points within the Fig. 4.1c).

4.2.2.1 Notched coupons ultimate tensile strength evaluation

In order to obtain an average UTS, by which to guide the in situ tests, tensile tests were conducted on ten coupons per material configuration on an INSTRON® servo-mechanical testing machine at a displacement rate of 0.2 mm/min. The UTS for each specimen was obtained by dividing the failure load by the cross-sectional area between the notches of each coupon. This was essential as water-jet cut notched sections achieved a tolerance of ±10% from the nominal width value of 1.0 mm. The cross-sectional area (CSA) value was obtained by the use of optical microscopes and CT scans using the Custom Nikon/Xtek Hutch among the μ-VIS X-ray Imaging Centre facilities. The scans, obtained at a resolution of 75 μm, had provided CSA values that led to the average UTS measured on the ten coupons being ∼20% lower than the UTS of the SRCT in situ tested coupons (for which the CSA was measured through the 0.65 μm resolution scans), consistently for the six materials. However, by measuring the ten CSAs through laboratory microscopy, the measurement accuracy was improved and the CSA results were found to be in good agreement with those

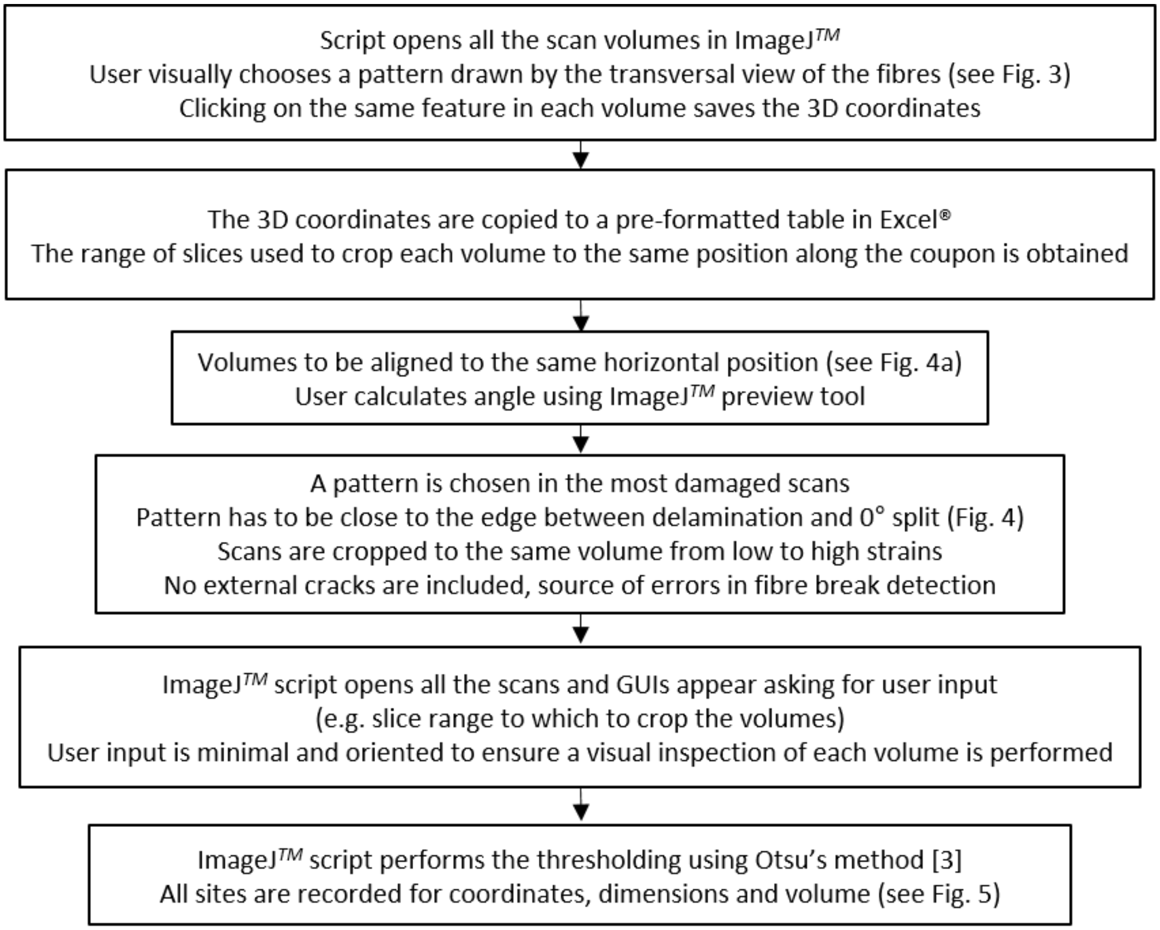

Script opens all the scan volumes in ImageJ^{TM}
User visually chooses a pattern drawn by the transversal view of the fibres (see Fig. 3)
Clicking on the same feature in each volume saves the 3D coordinates

The 3D coordinates are copied to a pre-formatted table in Excel®
The range of slices used to crop each volume to the same position along the coupon is obtained

Volumes to be aligned to the same horizontal position (see Fig. 4a)
User calculates angle using ImageJ^{TM} preview tool

A pattern is chosen in the most damaged scans
Pattern has to be close to the edge between delamination and 0° split (Fig. 4)
Scans are cropped to the same volume from low to high strains
No external cracks are included, source of errors in fibre break detection

ImageJ^{TM} script opens all the scans and GUIs appear asking for user input
(e.g. slice range to which to crop the volumes)
User input is minimal and oriented to ensure a visual inspection of each volume is performed

ImageJ^{TM} script performs the thresholding using Otsu's method [3]
All sites are recorded for coordinates, dimensions and volume (see Fig. 5)

Figure 4.2. (a) Illustration of the compact loading rig on the experimentation stage at the synchrotron facilities, (b) coupon geometry, (c) a 3D representation of the imaged volumes for all the scans and (d) a top view of the features detected within the volume (single fibre breaks or groups of co-planar fibre breaks. In this case a singlet and a duplet are highlighted).

found during the SRCT test campaign.

4.3 Image analysis

An automated image processing workflow was implemented in ImageJ$^{\text{TM}}$ and MATLAB®. The approach adopted in ImageJ$^{\text{TM}}$ for fibre break thresholding is shown in Fig. 4.2.

When strain is applied at this relatively high resolution, it requires care to image accurately the same volume with the required precision of a few micro-metres as the

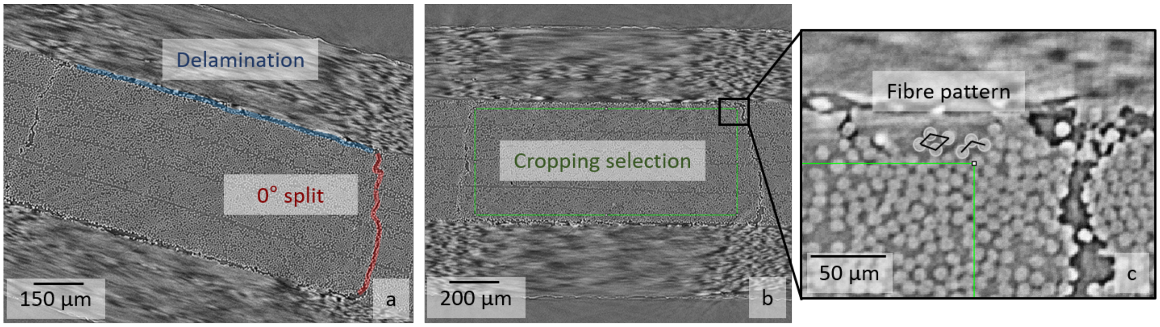

Figure 4.3. Cropping selection: (a) shows the typical damage modes in the analysed geometry (more details can be found in [22]); in (b) the 0^o layers are rotated and the cropped selection is shown in green, that will be used for an automated fibre break detection; in (c) an example of a pattern created by the fibre locations used to crop accurately all the scanned volumes to the same location within the coupon.

material in the intended scan volume is displaced due to the applied loading. However, by registering all the volumes to the same micro-structural reference points within the actual coupon, fibre breaks appearing at low strains will keep approximately the same coordinates within volume collected right up to failure. The same feature (i.e. the pattern created by the fibre positions on a transversal SRCT slice) is identified in all the scanned volumes – particle inclusions, voids, external peculiarities due to the manufacturing of the plates that are in the imaged area, as well as fibres in resin rich regions (for their misorientation with respect to the loading direction, represented by the z axis) are chosen. Accuracy in the use of such reference features is checked, and is found to always correspond to less than three voxels in the fibre direction from low to high applied loads. A pre-formatted Excel® sheet is filled with the z coordinates of the fibre patterns; as output, the range of slices to which to crop each volume to the smaller portion of volume that is equal for all the scan volumes is obtained. This range of slices is transferred via the GUI of the ImageJ$^{\text{TM}}$ script to allow user to crop the volumes.

The last collected scan (most damaged situation) is analysed first: the whole volume is rotated so as to orientate the composite layers orthogonal to the image (see Fig. 4.3a, then rotated in Fig. 4.3b). An identified fibre pattern is chosen, close to the edge between the delaminated area and the 0° split (more details on these damage modes for this coupon geometry can be found in [22]), as shown in Fig. 4.3c.

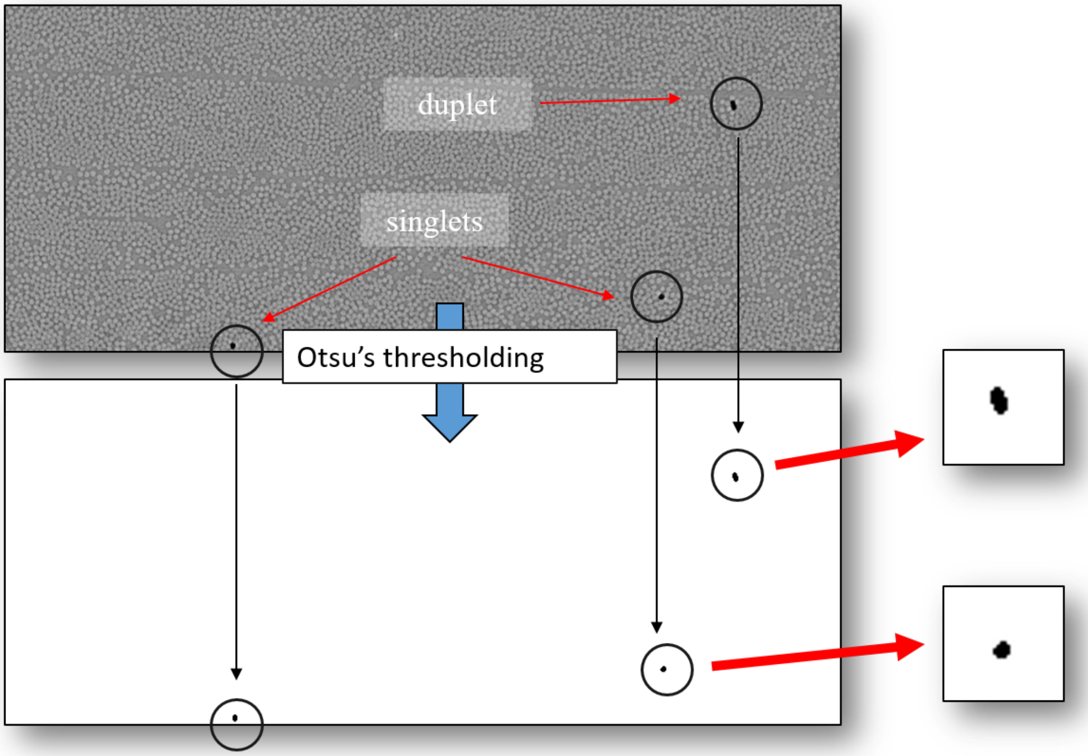

Figure 4.4. Segmentation approach for the break formation/accumulation evaluation. Scripts have been developed, using Otsu's threshold method [165]. From the binary images, all sites are recorded for coordinates, dimensions and volume.

A rectangular cropping selection is drawn, that contains the 0° layers and includes no delamination or 0° splits within the selected region (in green in Fig. 4.3b), as such cracks could represent false positives in the fibre break detection. At the end of this process, all the collected scans are cropped to smaller dimensions to ensure from unloaded to prior-to-failure conditions the same volumes are analysed. The same dimensions are used for all the cropped scans to ease the processing: it is checked that from 80% to 99% UTS, this corresponds to less than 20 slices being lost (corresponding to less than 15 µm in the z direction) in the last captured scan, which represents the most elongated condition. However, this translates into an error of below 0.5% in the fibre break evaluation, due to the fact that the spike in the fibre break formation happens at very high load levels, when less than 20% of the total elongation is left before failure. This allows the multiplets to be followed accurately, according to their appearance and evolution from low to high applied loads. Volumes

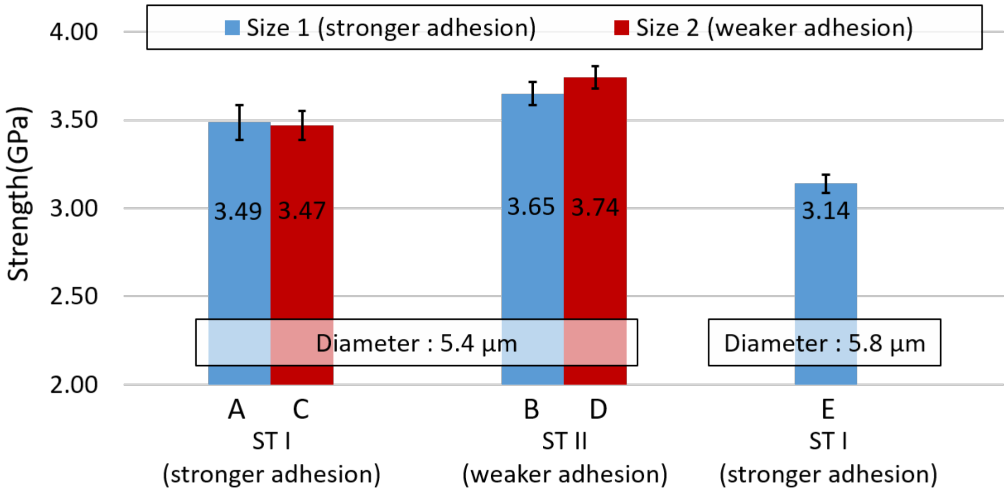

Figure 4.5. The average composite strength of the five configurations (based on 10 measurements per material) is reported. Materials are presented in order of fibre diameter (smaller to larger). The surface treatment (indicated as ST) has the greatest influence, with Materials B and D (surface treatment II) being the strongest. As can be seen, the strongest adhesion (configuration A) did not result in the highest composite strength. Also, a limited influence of the sizing is observed.

are binarised using Otsu's method [165]. An example of a binarised image is shown in Fig. 4.4, in which fibre break sites are identified, with data for their coordinates, dimensions and volumes recorded.

Single fibre breaks and multiplets are relatively easily distinguished by the feature volumes and linear dimensions. However, given:

- the low number of multiplets occurring within each volume (about 10-15 in scans prior to failure),
- the variation in multiplet geometry (for example a triplet can have a near-linear arrangement, or a more triangular geometry),

it was considered worthwhile for automated multiplet evaluation to be confirmed directly by visual inspection, given that the script provides their accurate position within the volume. As such, a high level of confidence is achieved in the current measurements of multiplet character (number of fibres, local spatial arrangement), having been carefully checked/confirmed for any false positives/false negatives during image processing.

4.3.1 Fibre volume fraction extraction

A macro written in ImageJ^{TM} was adopted to extract the fibre volume fraction from the high resolution scans. For each coupon, the scans collected at 100 N, i.e. containing no damage, were examined. Five images showing the top view of the fibres, similar to those adopted for the fibre break extraction shown in Fig. 4.4, were extracted from the main scanned volume at an axial distance of $\sim$250 μm from each other. From each image, all the fibre centres were extracted using the following image processing approach: a median filter was first used to reduce the general noise, followed by a sharpening to better define the edges of the fibres. An appropriate value for the thresholding was chosen to correctly binarise the fibres, followed by a watershed step to ensure that two fibres segmented as one (this is particularly likely to happen in highly packed regions), are divided into two entities; an eroding and dilating step is added to enhance the fibres separation. Following this, the 'ultimate points' function is adopted that provides the ultimate eroded points of the Euclidean distance map of the fibres in [23], which translates into only the centres of the segmented fibre being kept. The number of detected centres are multiplied by the nominal individual fibre section value provided by the manufacturer. The result is divided by the examined area from which the fibre centres have been extracted. This provides an approximate value for the fibre volume fraction, affected by an error for the approach adopted in this study of $\sim\pm1\%$, due to false positive and negative detection, and the omission in the centres count of the fibre centres at the edges of an image, centres that would have otherwise contributed with fractions of fibre sections.

4.4 Results

4.4.1 Macroscopic properties

In Table 4.2, for the five tested materials the fibre properties are presented. To a higher average fibre strength (calculated using the Weibull distribution) corresponds

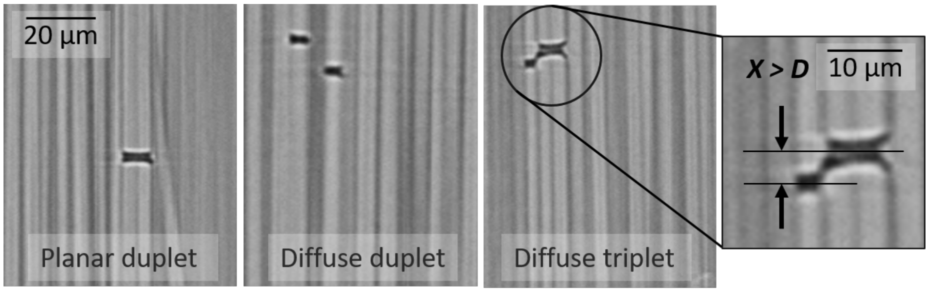

Figure 4.6. Example of planar and diffuse multiplets. Diffuse multiplets are defined as in [22].

to a higher composite strength.

The nominal fibre strength and the resulting measured average strength of the materials tested are summarised in Table 4.2, with the highest UTS fibres resulting in the highest composite strength. In Fig. 4.6, the average composite strength of the five configurations (based on ten measurements per material) is reported. The cross-sectional area was obtained through use of optical microscopy. The surface treatment appears to have the greatest influence, with materials B and D (surface treatment II) being the strongest. As can be seen, the strongest adhesion (configuration A) did not result in the composite having the highest strength. Also, a limited influence of the sizing is observed. The surface treatment seems to dominate the results, with B and D materials being stronger than A and C by at least ∼6%, corresponding in ∼200 MPa; the strongest surface treatment does not however translate into the highest strength. A limited influence of the sizing can be observed as well.

4.4.2 Multiplet arrangements

In this study, a distinction is made between planar and diffuse multiplets (see Fig. 4.6). In the absence of a generally accepted definition, multiplet definition follows that reported in [22, 24]. Planar multiplets were defined here as those having an axial separation of less than a fibre diameter, whilst diffuse multiplets have an axial separation lower than the estimated ineffective length of 70 μm reported by Scott *et al.* for the Hexcel Hexply T700/M21 system in [22]. It should be noted that this value of the ineffective length for the material systems analysed here could differ, but it is adopted in this instance for fibre break count comparison purposes only. An au-

Table 4.2. Summary of the nominal fibre strength of the fibres and the resulting measured average strength of composite in the tested geometry (extracted from ten measurements) with associated standard error values. The fibre volume fraction values are based on two measurements per configuration, based on the extraction procedure reported in Section 4.3.1, using the high resolution scans analysed in this study.

Mat.	Nominal fibre diameter (μm)	Fibre volume fraction (%)	Weibull shape factor (-)	Weibull scale factor (GPa)	Average fibre strength using Weibull (GPa)	Average composite UTS (GPa)	Standard error composite UTS (GPa)
A	5.4	47	5.11	11.35	8.05	3.49	0.10
B		52				3.65	0.07
C		50	5.47	11.29	8.07	3.47	0.08
D		46				3.74	0.06
E	5.8	59	6.31	9.7	7.55	3.14	0.05

tomated evaluation of the ineffective length is planned that follows the fibre shape, providing the length also for highly misaligned fibres.

The fibre break accumulation curves will be presented by separately plotting the total number of individual fibre breaks (including breaks that are part of diffuse multiplets), and the number of planar multiplets, to better assess the differences among the materials tested in terms of groups of individual and interacting fibre breaks, their formation and evolution[1].

4.4.3 Variability between coupons

In assessing the damage formation and propagation within the small sampling volumes in SRCT there are statistical aspects of damage that must be considered. In this case, these might be identified with local micro-structure variations, debonding

---

[1] This results in a lower number of breaks being presented, than was found in previous SRCT studies ([22, 24, 31]) that counted the total number of fibre breaks (i.e. all of the individual breaks in the planar multiplets were included in the count).

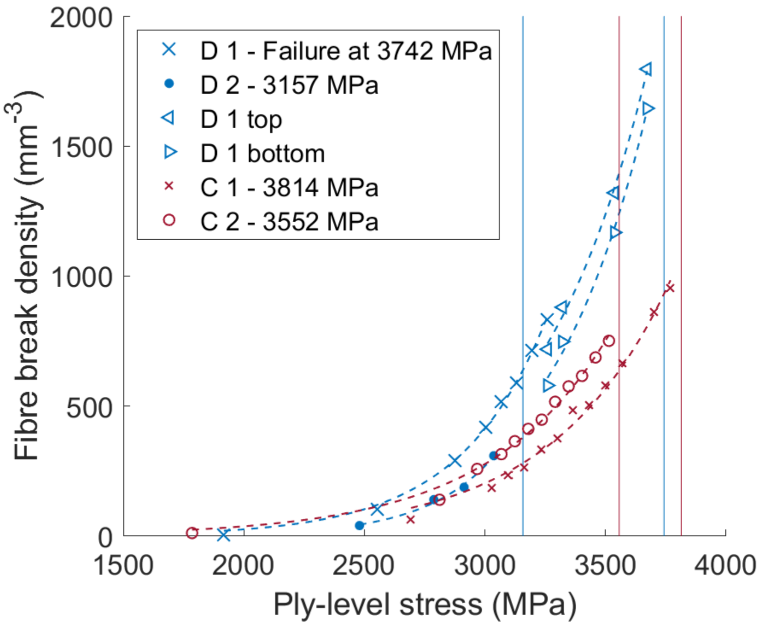

Figure 4.7. Comparison of coupons D 1 (scanned in multiple regions: D 1, D 1 top and D 1 bottom, as explained in Section 4.4.4), D 2, C 1 and C 2. Variability between coupons is estimated to be ~30% in fibre break density (planar multiplets not included). The error in stress is estimated to be ~5%.

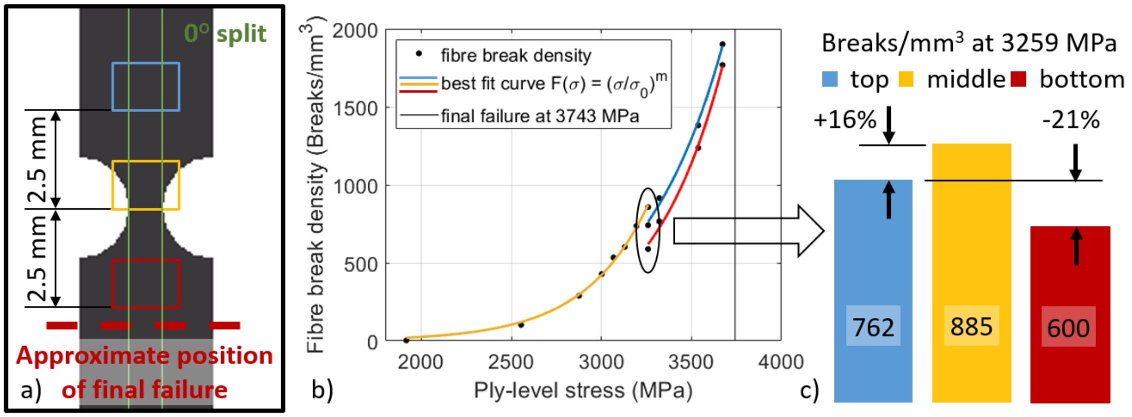

Figure 4.8. Coupon D 1, (a) tested geometry and imaged volumes to assess variability in fibre break accumulation within a coupon, highlighting the extensive 0^o ply splits, decoupling the central region from the initial notches; (b) the fibre break accumulation curves (planar multiplets not included); (c) the difference in breaks count at the same load level is assessed. Variation between different regions of the same coupon is ~30%.

between the plies and transverse ply crack (TPC) variability (damage modes extensively described in [22, 31]). As reported in Table 4.2, a variation in the fibre volume fraction is observed among the five material configurations, with values ranging from 46 to 59%. In Fig. 4.7, the number of fibre breaks as a function of the ply-level stress (the applied nominal stress in the reduced load-bearing section) is presented for material configurations C and D, with C representing the material with the best sampling (at least 10 data points collected for both coupons) and D the worst (4 data points vs. 10); this is associated with the stochastic nature of composite strength, as noted in Section 4.2.2. D 1, D 1 top and D 1 bottom indicate that the scans are collected at three different locations within the same coupon to assess levels of variability within individual coupons, as will be discussed in Section 4.4.4. For the material configurations tested in this study, variability between coupons has been estimated to be ~30% in fibre break density (planar multiplets not included). An error of ~5% in stress measurement is estimated.

4.4.4 Variability within a coupon

In order to assess volume sampling aspects of damage measurements (i.e. recognising the limited sampling volumes inherent to high resolution SRCT), fibre break measurement variations were analysed. Notwithstanding limitations on synchrotron access, this was achieved within one of the test coupons, thereby ensuring equivalent sample/material preparation influence and load bearing cross-section. Three positions along the coupon length and close to the notched area have been imaged as indicated in Fig. 4.8a, in which the approximate position of final failure with respect to the imaged regions is identified with a dotted line. At these loads 0^o plies are extensively debonded and mechanically uncoupled from the notches, i.e. equivalent and uniform loading is assumed for the three regions (observed 0^o splits indicated in green in Fig. 4.8a). The accumulation of fibre breaks with increasing ply-level stress is shown in Fig. 8b. For low stress levels, only the mid volume (in yellow) was scanned, as for all the other coupons imaged in this study. At a ply stress of 3259 MPa the three regions were scanned, and for higher stress levels the top and bottom regions were scanned. Fig. 4.8c shows the variability in break density for the three volumes at 3259 MPa. Variation between regions within the individual coupon is therefore in the range of ∼30% in terms of breaks, or ∼6% if considered in terms of stress, which might be attributable to the estimated ∼5% error in stress measurement.

4.4.5 Comparison 1: change in surface treatment (A to B)

In Fig. 4.9, the fibre break activity of the coupons with the highest number of collected scans is presented. As n-plets, the sum of the diffuse and planar multiplets is indicated; one n-plet is counted as one entity. This comparison could be equally made between materials A and B or C and D (sharing the same sizing type but adopting different surface treatments). However, although D 1 and D 2 exhibit a very similar singlet formation with stress, the truncation due to early failure of coupon D 2 results in this material being not to most suitable for drawing conclusions regarding fibre break accumulation. Hence, this comparison will be focused on materials A and B (with the exemplary coupons A 1 and B 1). Although the singlet formation with stress is very similar for the two materials, the higher average strength configuration (B) demonstrated a greater propensity for multiplet formation (particularly for n-plets with $n \geq 3$). The last scan collected for coupon B 1 appears at the final failure stress level (3629 MPa); this is due to the coupon being loaded to that level and the load (reduced by 10%) being held while scanning. When loading to the higher load step, the coupon failed before reaching the previous stress level, at 3606 MPa.

Modifying the surface treatment, obtaining a weaker adhesion, resulted in the coupons exhibiting a higher UTS (as shown in Fig. 4.5), while allowing more damage to be tolerated before failure (see Fig. 4.9). The size (n) of the largest observed multiplets doubled in coupon B 1, with a 5-plet captured in A 1 at ∼98% UTS and a 10-plet in B 1 at a similar stress level. Between materials A and B, the small multiplet activity is similar (2-plets and 3-plets), but more larger multiplets were observed in material B. A high multiplet susceptibility for a given stress level is evidently not a simple indicator of strength and the total defect content at failure is clearly material-dependent, with B being the more defect tolerant of the two materials compared here. As will be shown in Section 4.4.7 where a different fibre type is adopted, the reason for a similar single fibre break accumulation from low to high strains may be due to the fibre type that is kept the same for the two configurations A and B.

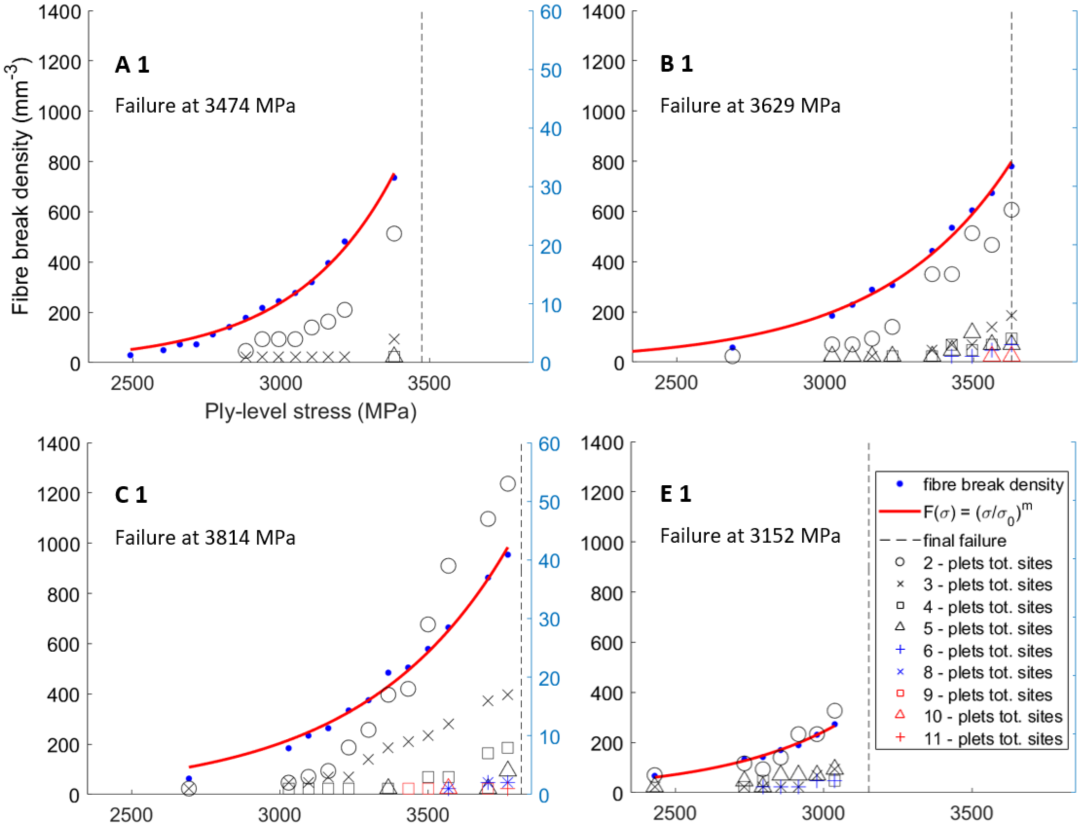

Figure 4.9. The fibre break accumulation activity is shown for individual coupons of the materials assessed in the three comparisons. The sum of diffuse and planar multiplets is represented, as the total of n-plet sites,, with a 2-plet counted as a single entity. In red symbols, the largest multiplets are represented, as they are believed to be the possible trigger for final failure [14, 32].

4.4.6 Comparison 2: change in sizing (A to C)

As for comparison 1 of Section 4.4.5 between materials using the same fibre type, the singlet formation vs. stress response is very similar. However, for an equivalent level of stress and immediately prior to failure, a very high susceptibility to multiplets for material C, adopting the sizing type 2 (allows a weaker adhesion than sizing type 1) is observed. The largest multiplet captured before failure for high strains is a 5-plet in A 1 and an 11-plet in C 1. The number of 2 plets observed in C 1 is two times higher than A 1, with C being the material configuration with the highest number of small multiplets (2-plets and 3-plets) observed in this test campaign. The high number of multiplet sites is clear and consistent for repeat coupons and as the two configurations are characterised by a similar average strength (the coupons A 1 and C 1 presented in Fig. 4.9 have different individual UTS values, but the average values are comparable, as shown in Fig. 4.5), the multiplet build-up and final state cannot simply be linked to the average UTS. An increased defect tolerance is observed when a weaker adhesion is obtained by a change in sizing type.

4.4.7 Comparison 3: change in fibre type (A to E)

Configuration E is characterised by a larger diameter and a lower nominal fibre UTS: 5.6 GPa of the fibres used in configuration E against 6.5 GPa of the fibre type used for the configurations A to D. The same fibre sizing and interface treatment are adopted as for both materials A and E. The average composite UTSs are 3.49 GPa for Material A and 3.14 GPa for material E. As shown in Fig. 4.9, the singlet formation with increasing stress in the two configurations is similar but different by coupon UTS level. However, a rapid onset of 2-plets/multiplets at low stresses as well as a truncation of the singlet accumulation curve by early failure can be observed for material E. In this case, susceptibility to multiplets is apparently coincident with a lower average UTS value.

4.4.8 Planar multiplets

Planar multiplets are best assessed in terms of 2-plets for the materials in this study as larger multiplets are too sparse for a simple comparison. The ratio of planar to diffuse 2-plets typically is in the 40-50% range, with the exception of configuration E as shown in Fig. 4.10, in which comparison 4 (A 1 vs. E 1 of Fig. 4.9) is repeated for planar multiplets only: coupon E 1 appears to be particularly susceptible to planar multiplet formation. It can be observed that a higher number of planar 2 plets form in E 1 in Fig. 4.10 in comparison to the number of total 2-plets of Fig. 4.9. This is explained with the planar defects being also counted within the larger diffuse clusters. Planar 2 plets and n-plets increased rapidly, appearing to be fibre controlled, as the two configurations share the same sizing and surface treatment. Overwhelmingly, the planar multiplets observed in this study have been seen to form at different UTS levels but not grow close to macroscopic final failure (as reported in [22–24, 31]). Details of the formation, evolution and local morphology of the planar multiplets observed in this study will be provided in a following publication.

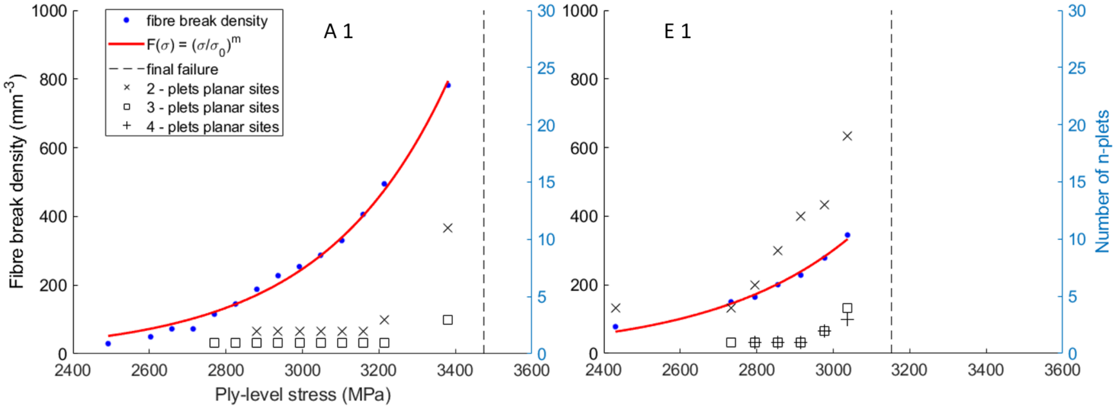

Figure 4.10. Materials A and E are compared in terms of single fibre break and planar multiplet accumulation. A certain degree of planar damage susceptibility is observed in material E. This phenomenon seems to be fibre controlled, as sizing type and surface treatment are unchanged between the two configurations.

4.4.9 Comparison summary

Across the supplied fibres, sizing and surface treatment types, a number of points are identified:

- the rate of singlet fibre break accumulation with ply stress appears relatively consistent for these composites (within the experimental scatter), and is independent of UTS and the multiplet behaviour;
- the incidence (onset and rate) of multiplet damage accumulation with applied ply stress does vary significantly within the test group;
- for material configurations A to C, the prevalence of multiplet formation increased from A to C, with B being the highest average UTS Material and A and C having a similar level of average UTS (see Fig. 4.10). A weaker adhesion obtained through different surface treatment (materials A to B) led to a comparable number of small multiplets (2- and 3-plets), but a higher number of large

multiplets (with a 10 plet formed in B). An even weaker adhesion (materials B to C) obtained by changing the sizing type led instead to a similar activity for large multiplets accompanied by a much larger formation of small multiplets (see Fig. 4.9).

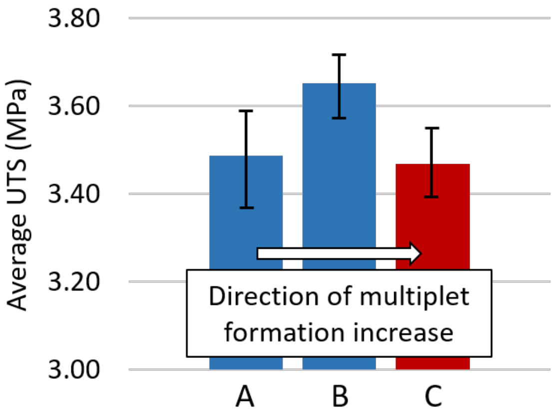

Figure 4.11. The average UTSs of the three materials which are the main focus of the comparisons, are represented in order of amount of multiplets accumulated before final failure (A to C). The multiplet behaviour appears to be independent of the average UTS value.

4.4.10 Conclusions

An extensive database of performance and damage behaviour at a deep micro-mechanical level has been generated in this study for a range of materials with different fibres, surface treatments and sizing, to an extent and detail the authors believe has not been achieved before. A semi-automated approach has been developed to precisely quantify the damage progression within in situ tested composite coupons and further areas of application can be considered (e.g. inter- and intra-laminar damage tracking). Automated quantification, repeatability and morphology measures (e.g. planar and diffuse multiplets) have been generated for a large number of SRCT scans. The following conclusions have been drawn from the results:

- the accumulation of singlets and multiplets indicates that single fibre breaks play no simple role in controlling the average UTS of the material;

- if a clustering behaviour is to be controlled, both surface treatment and sizing can be modified, consistently with some interface role in load shedding from break sites to intact neighbours;
- current materials behaviour appears most readily interpreted in terms of combined influence of:
  - multiplet susceptibility;
  - defect resistance (maximum scale/frequency of multiplet site that can be accommodated before failure);
- materials control/design aspects evident from the results suggest:
  - the same sizing types and surface treatments may be identified with detrimental influences on defect tolerance, but by different mechanisms: e.g. sizing type 1 and surface treatment II in the lower diameter, higher strength fibres configuration (M aterial A) has led to lower UTS than other configurations with the same fibres but to small/sparse population of multiplets, whilst in larger diameter, lower strength fibres configuration (material E) the same sizing/interface induced the formation of more planar multiplets, which are more detrimental to strength.

This work represents an experimental effort that is only a first step in the ongoing research to better understanding the key failure events in tensile loaded unidirectional composites. Further comprehensive experimental campaigns are suggested that can provide a better insight into the statistical coupon-level variability as well as the higher level of detail as to the different mechanisms occurring when modifying the fibre/matrix interface.

(This page was intentionally left blank)

CHAPTER 5

PLANAR FIBRE BREAK CLUSTER ASSESSMENT

A higher level of understanding is desirable in describing the micro-mechanisms leading to longitudinal tensile failure in fibre-reinforced polymers, as to whether the critical state of groups of interacting fibre breaks (clusters), thought to trigger unstable crack propagation, can be recognised and predicted, and whether models can be improved to enable better engineered and hence better performing components. In situ SRCT has been used to perform a detailed qualitative (and where possible quantitative) study of cluster morphology, obtained through careful comparison of different coupons made of the same material that include systematic variation in the fibre/matrix interface, believed to guide the cluster formation. The effects of different fibre types are also explored, and it is confirmed that stronger interfaces lead to cluster formation at lower stress levels. For the test matrix investigated herein, higher Weibull modulus fibres and a stronger interface seem to induce the highest multiplet (i.e. clusters containing multiple fibre breaks) to singlet break ratio (40/60). New hypotheses are also discussed as to the potential causes of stabilised clusters based on the level of damage that has been observed post-mortem.

5.1 Introduction

In many applications, a key design consideration for composite components is the tensile failure of their unidirectional plies, commonly controlling ultimate tensile strength [22]. Accurately predicting the failure of unidirectional composites is thus of importance but remains a challenging task due to the complex internal structure and hence the large number of model inputs needed. Furthermore, detailed experimental insight is lacking regarding the micro-mechanisms leading to failure [14]. In practice, predictive uncertainties commonly lead to components being often over-designed [24].

The longitudinal tensile failure of unidirectional composites is generally believed to be controlled by the following process: all fibres are loaded in their axial direction and begin to fail individually, based on the -fibre strength distribution. Fibres surrounding the broken ones experience a stress concentration that will increase their chance of failure. This leads to the formation of groups of fibre breaks that eventually coalesce and further intensify the stress concentrations on the neighbouring intact fibres. One of these groups of interacting fibre breaks (referred to interchangeably as clusters or multiplets) will become large enough to grow unstably, causing macroscopic failure [32].

Several models are available in the literature [27–30, 52, 101], that include different mechanisms and/or simplifications to the fibre failure phenomenon. As noted by [14], for elastic and well-bonded materials, the stress concentration in the portion of matrix surrounding a fibre break would be infinite, which is non-physical. Instead, one or more of the following phenomena can moderate the local stress: the matrix yields, micro-cracks form in the break plane or the fibre/matrix interface debonds. In the modelling exercise of [26], it is indicated that matrix cracks have a negligible influence on stress concentrations, ineffective length, multiplet development and failure strain.

Yielding of the matrix and interfacial debonding near the fibre fracture crack tip can instead lower the stress concentrations, thereby reducing the tendency of further fracture growth [63]. The wider distributions of stress resulting from the debonding (as well as the plasticity of the matrix) help spreading non-catastrophic failure modes enhancing the toughness of the material [63]. If the matrix yield stress in shear is much lower than the interfacial strength, it has experimentally demonstrated that plastic deformation of the matrix occurs rather than fibre to matrix debonding, with a longitudinal plastic region developing in the matrix at the crack tip [166, 167]. Within the modelling results of [100], the dimensions of the largest multiplets observed before failure reduce of approximately 70% for the material system simulated in the study (T700/M21, of which experimental data was extracted from [22]) when introducing matrix yielding (an elastic-perfectly plastic behaviour of the matrix is assumed), confirming the effect of the reductions in the stress concentration factor (SCF) on multiple fibre failure.

Debonding may be expected to be controlled by the interfacial shear strength, the strain energy release rate, the fibre/matrix friction, the matrix yield strength and the fibre stiffness [14]. Current *in situ* tensile tests performed on CFRPs, imaging thousands of fibres, such as the ones performed in this work and in [22, 24, 31], do not have a resolution high enough to capture the separation between fibre and matrix in CFRPs and alternative techniques that could capture the phenomenon are limited to surface measurements only [14]. This means the results for the fibre fracture geometries observed in single fibre composite tests ([70]) have not been proved to be transferable to coupons with thousands of fibres [14]. In [164] the effects of both matrix plasticity and interfacial debonding on the SCFs are shown. A matrix with a relatively low yield strength reduces the SCF values more than the fibre/matrix interfacial debonding; it is observed that modelling the matrix as elastic leads to an unstable interfacial debonding, while an elastic-plastic matrix allows a stable debonding and arrest.

Fibre fracture is a dynamic process that leads to a change in the stress level over time, leading to higher SCFs [14]. The failure of a fibre causes a compressive wave to develop in the neighbouring fibres, followed by a tensile wave, leading to a dynamic axial stress overshoot and higher dynamic SCF values [118]; a local plastic zone can be expected to form within the matrix in a region that is close to the break, due to the rapid spring-back of the fractured fibre. Considering the matrix as elastic-perfectly plastic, leads to a reduction in the peak SCF as well as acting as a damping mechanism for the stress wave produced when the fibre breaks (the oscillations are less pronounced and extend for shorter distances), thus reducing the dynamic SCF value. For both an elastic or elastic-plastic matrix, stress concentrations extend to much larger distances than in the static case [100, 164]. Hence, from a material design point of view, to reduce the peak dynamic SCFs and delay the dynamic formation of clusters, a resin system with relatively low yield strength could be adopted [164]: a matrix that plasticises at lower stress levels leads to the stresses being spread out over larger distances, while the peak SCF reduces.

To the best of the authors' knowledge, none of the quasi-static models retrievable in the literature, e.g. [27–30, 52, 101] predicts the sudden appearance of planar multiplets as well as their arrest in growth after formation, as observed in the experimental campaigns of [22–24, 31]. In [100], the dynamic effects of the instantaneous formation of groups of interacting fibre breaks are evaluated that provide an indication of the SCF increase due to the dynamic effects. However, in their study it appears to the authors that no indication is reported as to the number of planar multiplets (a) forming in the time windows associated with the dynamic phenomena and (b) arresting their growth after formation.

In the last decade, Synchrotron Radiation Computed Tomography (SRCT) has become a powerful source of new insight into the damage mechanisms of CFRPs and as a validation tool for predictive models [127, 168–170]. While no direct evidence has been provided, SRCT has suggested, through the studies reported in [22–24, 31] some implications of the dynamic stress concentrations in the failure processes of unidirectional composites, where further increases in load did not lead to further adjacent breaks. The current study uses SRCT with the aim of reporting on the local morphology of clusters, to better understand the effects of constituent parameters and micro-structural features on their initiation and accumulation (up to the point of macroscopic final failure of the tested coupons). Cluster formation is examined in detail in a significant number of coupons, addressing a number of fundamental variables, and this will be presented qualitatively and where possible quantitatively. Consistent systematic variations in materials parameters are considered, such as the fibre/matrix interface, as suggested in [14, 32] to guide further tests to provide the modelling community new experimental data to perform a model consistency check across a range of materials.

5.2 Materials and experimental procedure

5.2.1 Materials

Coupons made of five different material configurations were cut from $(90_2/0_2)_s$ prepreg panels fabricated by Mitsubishi Chemical Co. and tensile tested to failure to assess the effects of the fibre type, sizing type and the surface treatment on the fibre break accumulation. These materials in the same configurations were reported in Chapter 4. Whilst specific material and process conditions are proprietary, qualitative differences are provided in Table 5.1.

Table 5.1. Summary of the material configurations (as presented in Chapter 4, reported here for ease of reference). Two carbon fibre types are used. Two sizing agent types (with type 1 providing stronger adhesion than type 2) and two surface treatment configurations are used, with type I providing stronger adhesion than type II.

Configuration	Fibre diameter (μm)	Sizing agent type	Surface treatment type	Resin
A	5.4	1	I	# 350 series, amine curing epoxy
B			II	
C		2	I	
D			II	
E	5.8	1	I	

These materials can be classified in order of fibre/matrix adhesion:

- Materials A and E: the strongest adhesion is provided by sizing agent type 1 and surface treatment I. Material E is distinct from A in terms of fibre diameter (5.8 vs. 5.4 μm nominal average diameter respectively) and a lower average strength (more details in Table 5.2);
- Materials B and C: Material B has a lower fibre to matrix adhesion than A and E, obtained through a different surface treatment; Material C has a lower fibre to matrix adhesion than A and E through a different sizing type. The

Table 5.2. Summary of the nominal fibre strength of the fibres and the resulting measured average strength of composite in the tested geometry extracted from ten measurements with associated standard error values, as presented in Chapter 4, reported here for ease of reference). The fibre volume fraction values are based on two measurements per configuration, based on the extraction procedure reported in Section 4.3.1, using the high resolution scans analysed in this study.

Mat.	Nominal fibre diameter (μm)	Fibre volume fraction (%)	Weibull shape factor (-)	Weibull scale factor (GPa)	Average fibre strength using Weibull (GPa)	Average composite UTS (GPa)	Standard error composite UTS (GPa)
A	5.4	47	5.11	11.35	8.05	3.49	0.10
B		52				3.65	0.07
C		50	5.47	11.29	8.07	3.47	0.08
D		46				3.74	0.06
E	5.8	59	6.31	9.70	7.55	3.14	0.05

manufacturers identify A and C as having similar overall fibre/matrix adhesion strength;

- Material D: characterised by a lower adhesion sizing agent (type 2) and surface treatment (type II). The same aerospace grade fibres of Materials A, B and C are adopted.

1 mm thick double-edge notched coupons were machined via water-jet cutting, following Wright *et al.*'s procedure [127].

5.2.2 Experimental procedure

In situ tensile testing campaigns were carried out at the European Synchrotron Radiation Facilities (ESRF) in Grenoble, France, at beamline ID19, with the sample-detector distance being set to 50 mm, enabling near-field Fresnel diffraction (edge detection). The beam energy was 19.5 keV and a multilayer monochromator was adopted. The coupons were placed in a custom modified DEBEN CT5000® electromechanical compact rig, fixed on the rotating stage. The coupons were scanned initially in a near-unloaded state (100 N was applied to ensure no movement between the coupon and the grips, that could compromise the image quality) and then in a loaded state. To ensure no further damage was introduced while scanning, the load was reduced to ∼10% lower than the peak load applied at any specific load step, before each scan was performed. 2996 projections were collected during each tomographic scan, using a 2160x2160 pixel detector system, through a 180^o rotation. An exposure time of 50 ms was chosen, resulting in ∼2.5 min of total scan time. The optics adopted in the current study provided an isotropic voxel resolution of 0.65 μm, that allowed individual fibre and fibre break identification from the scans. Although the field of view of 1.3 mm was the same for all the ∼140 volumes collected in the test campaign, the examined volumes differ in dimensions. By registering all the volumes to the same position within the coupon length and by cropping out larger cracks (delamination, transverse ply cracks and 0^o splits) which may cause false fibre break detection, the analysed regions for fibre break assessment have volumes in the range of 0.3 to 0.5 mm^3, while typically including ∼8000 fibres in the 0^o plies. Due to the stochastic distribution of strength in these materials, it is not possible to precisely determine *a priori* the load steps as a percentage of UTS at which to scan a coupon. Hence, there are some discrepancies in terms of the intervals at which images were captured between the coupons.

Starting from the ∼90% UTS step, one coupon (Material D, Coupon 1) has been scanned at two locations positioned at an axial distance of ±2.5 mm from the location of all the other scans that were centred on the notched area, to assess multiplet activity variability within the same coupon. Scans are indicated as D 1 top and D 1 bottom. A second coupon (Material C, Coupon 1) was scanned post-mortem during a different test campaign at the same synchrotron facilities and using broadly similar settings. A value of 0.325 μm for the isotropic voxel resolution was adopted in this case, with a propagation distance of 14 mm and an exposure time of 5 ms. The typical geometry of the coupons analysed in the current work is reported in Fig. 5.1. Pull-out of the central 0^o layers was observed, for a length of ∼2-3 mm. As shown in Fig. 5.1a and Fig. 5.1b, this results in the mean failure plane not being captured within the field of view of the scans, which were located at the mid-section of the coupons and the region scanned post mortem being different from that scanned before failure. Nevertheless, imaging the crack profile and a volume below it, allowed the differences in terms of fibre breaks between the prior to-failure and the post-mortem conditions to be assessed.

5.3 Image analysis

Automated image processing was implemented in ImageJ$^{\text{TM}}$ and MATLAB$^{®}$, and has been outlined in Chapter 4; here the main steps are reported for clarity. When tensile strain is applied at such high resolution, appreciable specimen movement is to be expected, causing the imaged volume to shift slightly. As such a script has been developed that opens all the scans in ImageJ$^{\text{TM}}$ and allows the user to visualise each scanned volume and to find patterns created by the view of the fibres along the fibre direction, that are then used to crop all the volumes to the same dimensions and position within the coupon length. This is done to analyse fibre break formation and evolution from low to high strains with each break keeping the same coordinates in all the volumes. Fibre break segmentation follows, adopting Otsu's method [165]. Single and multiple fibre breaks are distinguished and catalogued by volume size using a MATLAB$^{®}$ script. Given the relatively low number of multiplets identified and the variation in cluster geometry (distinct multiplet geometries are observed, as will be shown in Section 5.4.3), it was possible for all multiplet identifications to be confirmed by visual inspection, with the automated measures being carefully checked for any false positives and false negatives.

5.4 Results

5.4.1 Individual multiplet formation and growth

In the first instance, planar multiplet formation is analysed here, as these features are considered most likely to constitute the critical damage that cause the final failure in tensile loaded unidirectional composites [14, 32]. SRCT evidence has shown that

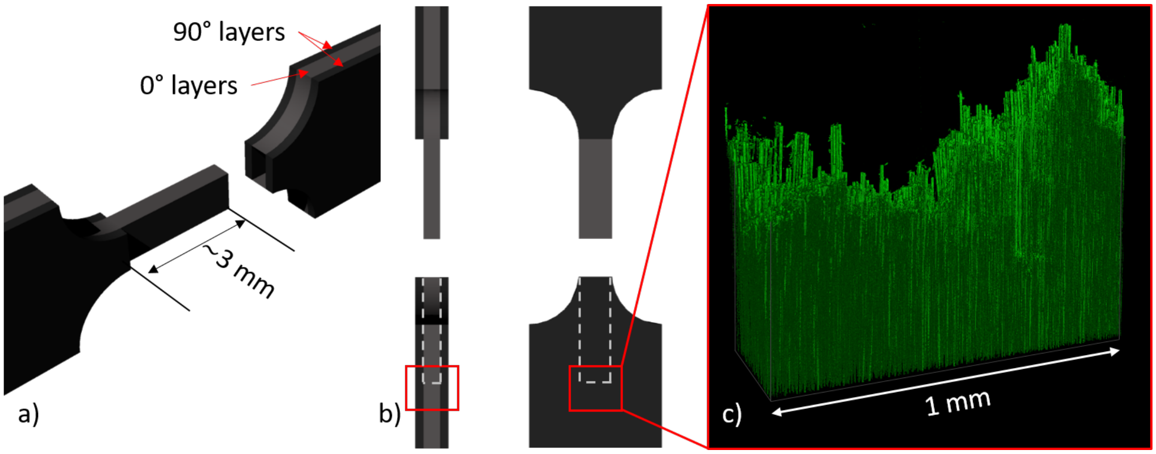

Figure 5.1. The geometry of a typical tensile failed coupon from this test campaign is shown in a) and b). The pull-out of the thinnest section composed of 0^o layers is observed for a length of ~2-3 mm for the great majority of the specimens. The scanned volume is shown in c). The fracture surface is characterised by fibre bundle pullout.

no more than 10% of fibres have failed in the micro-mechanical coupons used in the current work at 99% of the UTS, [22, 23, 31], implying the unlikeliness of final failure being caused by the catastrophic uniform weakening of a transverse section due to a non-localised, high density of fibre breaks. In the great majority of these studies, planar multiplets were seen to appear 'instantaneously' while performing the experiments, at least given the time required (~4 minutes) to capture an image by SRCT and the load steps used. An average of eight scans collected between ~90%UTS and the final tensile failure of the coupon were collected in the current study. As such, a given multiplet consisting of n breaks would appear at a specific load step: in the great majority of cases, subsequent loading did not give rise to any further fibre breaks at the site (n would be unchanged immediately prior to final fracture), potentially consistent with an influence of dynamic stress concentration being involved in their formation, as discussed in Section 5.1, or some form of SCF amelioration occurring during the initial multiplet formation event, such as fibre/matrix debonding and/or matrix plasticity.

In each tested coupon, only a handful of multiplets has been observed to grow in number of fractures with the applied stress. Based on noting samples/materials with the most consistent behaviour between individual tests, two coupons of Material C

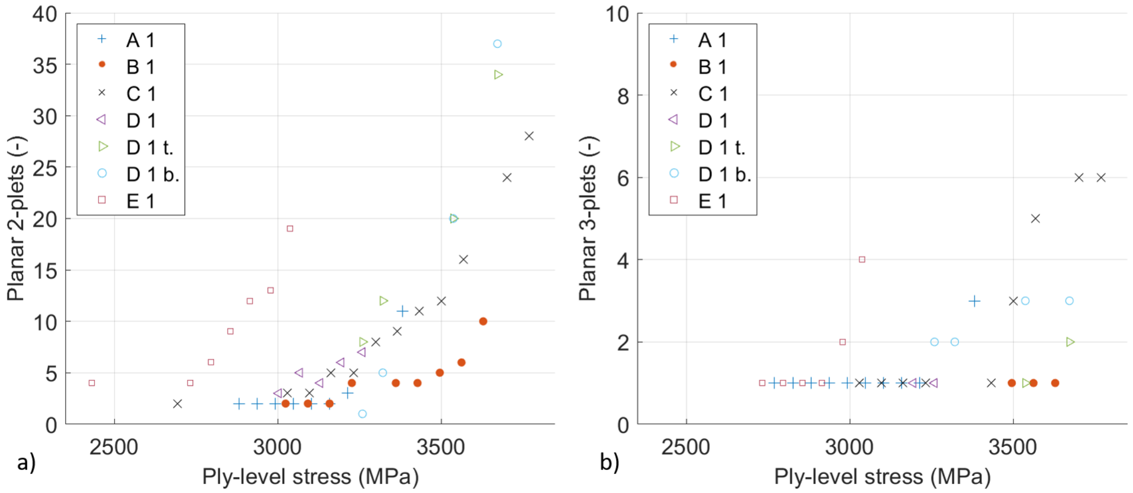

Figure 5.2. The total number of planar 2- and 3-plets as observed in the five materials plotted in terms of ply-level stress. The coupons chosen are those with the highest number of scans obtained (scans slightly differ in volume; values indicated in Table 5.2). Fibre breaks are seen to develop for lower levels of stress in Material E, which exhibits a lower average strength compared to the other material configurations. The remaining materials shows a more comparable accumulation of multiplets. This includes the D 1 t. and D 1 b. scans collected at the axial distance of ±2.5 mm from the location of all the other scans.

(C 1 and C 2) have been visually assessed for multiplet formation. Of the 37 multiplets observed in C 1 (the total number of multiplets is reported in Table 5.3), only one 3-plet originated from a pre-existing singlet with the appearance of a 2-plet within a single load step. Three more 2-plets formed from singlets, representing a total of less than 10% of multiplets growing. A similar trend was observed in coupon C 2.

Effects of material configuration were identified on multiplet formation behaviour. In most cases the 2-plets formation started at ∼80% coupon UTS and the 3-plet at ∼85% coupon UTS. The few larger multiplets observed (five 4-plets, three 5-plets and one 6-plet) formed at ∼90% coupon UTS and above. The only exception is represented by Material E, characterised as larger diameter, lower strength level fibres: 5.8 μm vs. 5.4 μm diameter, a higher Weibull shape factor, and a lower average fibre strength calculated using the Weibull distribution of 7.55 GPa vs. 8.05 GPa, as reported in Table 5.2. Material E exhibited the earliest planar multiplet onset of the tested materials.

Material E is also the material with the highest fibre volume fraction observed in this study (59%), while the remaining four configurations sharing the same fibre type had a volume fraction of ∼49%, see Table 5.2.

5.4.2 Multiplets accumulation

Notwithstanding the observation that multiplets generally do not grow under load, the accumulation of smaller (2-plets) and larger multiplets (3-plets and higher) under increasing load was seen to differ among the materials tested. In Fig. 5.2, the planar 2-plet and 3-plet accumulation plots for the four coupons with the highest number of collected scans are shown, with 2-plet and 3-plet representing the only multiplet configurations observed in significant numbers in the tested coupons. While an increase in 2-plet formation can be observed for larger strains, distinct plateaux are observed for the formation of 3-plets, particular on initial formation (in the 85 to 95% UTS range).

The material configurations are compared (using one exemplary coupon per material) in terms of planar multiplet formation and accumulation. It is observed that:

- the strongest interface materials (A and E, characterised by different fibre types, but the same sizing and surface treatment) behaved differently, with the lower fibre strength configuration (Material E) exhibiting higher numbers of 2-plet and 3-plet formation than Material A and at lower ply stress levels. At the highest load steps captured (at ∼97% UTS), Coupon E 1 showed a higher number of larger n-plets than in A 1: four 3 plets, one 4-plet and three 5-plets vs. one 3-plet (see Table 5.2). E represents the configuration with the highest propensity for multiplet accumulation (normalised to the ply stress). In the first instance, it is noted that E possessing the highest Weibull modulus (see Table 5.2), i.e. fibres are expected to break at stress levels closer to each other [14, 70];

- a change from a stronger to a weaker interface, through a variation in the surface treatment, is analysed when comparing Material A to B or C to D. Focusing on Material A and B, the same Weibull parameters were provided (see Table 5.2), indicating a similar likelihood of broken fibre at a given ply stress level based on the fibre strength distribution only. A slightly higher fibre fraction is observed in B if comparing to A (respectively 52% vs. 47%, with a ∼±1% of error in the estimates) as well as a slightly higher average composite UTS (3.65 vs. 3.47 GPa). The accumulation of 2-plets and 3-plets in terms of ply stress level is different: Fig. 5.2 shows a reduced propensity for multiplet format in the weaker interfaced Material B. This is consistent with the interface debonding enhancing damage tolerance [63], in that in Material B with multiplets being less able to extend for a given applied stress. The comparison of Materials C and D did not show such a consistent effect however, the 2- and 3-plet formation appearing to be broadly similar, suggesting that the sizing type was having a more dominant effect in this case (i.e. both employ Type 2 sizing).

In terms of the apparent fibre interface changes here, observations appear to be consistent with [23], in which it was reported that stronger interface materials showed a steeper multiplet accumulation rate.

5.4.3 Singlet to planar multiplet ratios

Among the scans collected before macroscopic failure for the tested coupons, ∼200 2-plets, 30 3-plets and 10 larger multiplets were visually checked. In Fig. 5.3a, the percentages of singlets and planar multiplets are compared for six material configurations, presented in order of fibre/matrix interface strength. The respective multiplet count is presented in Table 5.3. In counting the multiplet percentages, each break is considered, i.e. a 2-plet contributes two breaks to the overall count. The last two bars (identified by D 1 t. and D 1 b.), represent the data from two series of scans collected on coupon D 1 at an axial distance of ±2.5 mm from the position of all the other scans that were centred on the notched area. D 1 b. location, in red in Fig. 5.3b, is closer than the position of D 1 t. to the plane at which the final failure of the coupon occurred. The multiplet behaviour observed in these scans is consistent with those observed from scans in the notch region, as shown in Fig. 5.3a and Table 5.3.

Material E clearly demonstrated a different behaviour compared to the other five materials investigated: ∼40% of the fibre fracture locations were multiplets (vs. singlets), which was more than double the percentage in any of the other materials.

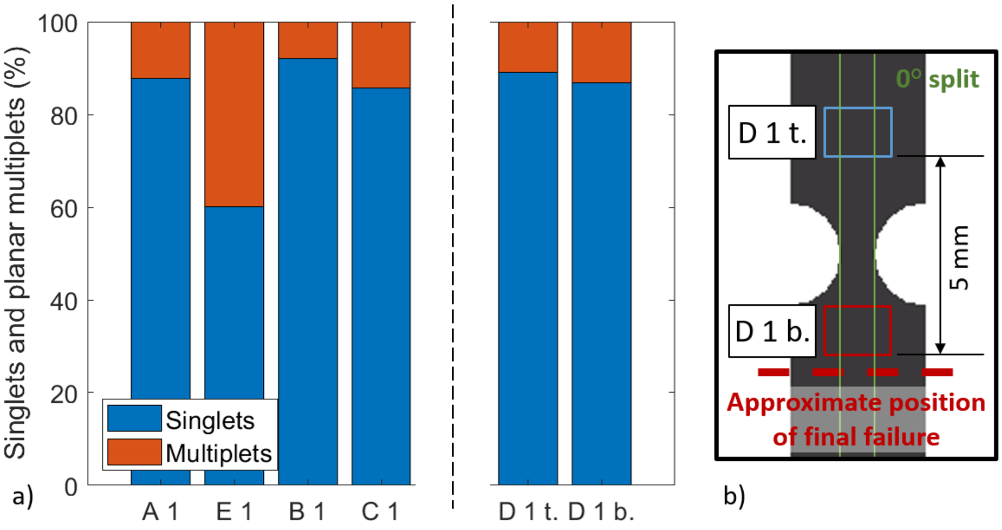

Figure 5.3. In a) the singlet and multiplet proportions plotted for the six exemplary coupons in the scans collected prior to failure, i.e. at ~96-99% coupon UTS (see Table 5.3). Material E is clearly significantly different in its behaviour from the others and shows the highest multiplet to singlet ratio of the materials tested; b) shows the two positions along the coupon length at which scans identified as D 1 t. and D 1 b. are collected. In light green the 0^o splits are indicated that isolate the central region (i.e. portion of coupon between the green lines in the figure) from the lateral parts that have been notched.

In Fig. 5.4, the development of the multiplet percentage from low to high stress levels is plotted. As shown in Fig. 5.4a, the majority of breaks appeared in the form of singlets, with the number and fraction of multiplets increasing with stress. This trend was observed for all the coupons and material configurations tested in the current work and is consistent with the response reported in [23, 31]. In Fig. 5.4b, the number of singlets and planar multiplets is shown, highlighting the contribution of 2-plets, 3-plets and 5-plets to the high multiplet percentages reported in Fig. 5.4a.

Table 5.3. Number of planar multiplets as observed from CT scans taken prior to failure. Multiplets are indicated for the coupons with the highest number of collected scans. Materials are presented in order of the level of adhesion: Materials A and E have the highest adhesion level.

Coupon	Ave. strength (GPa)[a]	Highest % UTS scanned	Volume analysed (mm^3)	2-plets	3-plets	4-plets	5-plets	6-plets
A 1	3.49	97.3	0.35	12	3	-	-	-
E 1	3.14	96.4	0.36	19	4	1	3	-
B 1	3.65	98.0[b]	0.43	10	1	-	-	1
C 1	3.47	96.4	0.54	28	6	3	-	-
D 1 t.	3.74	98.1	0.33	34	2	-	-	-
D 1 b.	3.74	98.1	0.33	37	2	-	-	-

[a]: composite average strength values as extracted from Section 4.4.1;

[b]: before scanning, load is reduced by ∼10% to avoid material movement (due to stress relaxation) and to avoid consequent artefacts. After scanning and while loading to the next load step, the coupon failed before reaching the load already reached at the previous step. Hence, a 98.0% indicative value is reported that could be affected by a ∼±2% of error, given the average UTS obtained for the material configuration.

5.5 Discussion

5.5.1 Multiplet geometries

In Fig. 5.5, examples of multiplet shapes are presented, as extracted from the CT scans collected prior to failure, on two orthogonal views. Planar multiplets were seen to arise in both locally highly and loosely packed regions, with different multiplet shapes. Compact, linear or 'quasi-linear' geometries were observed for the 3-, 4- and 5-plets. No evident patterns or preferred directions of development with respect to the in-layer or out-of-layer directions were found, with a significant number of multiplets having no specific orientation.

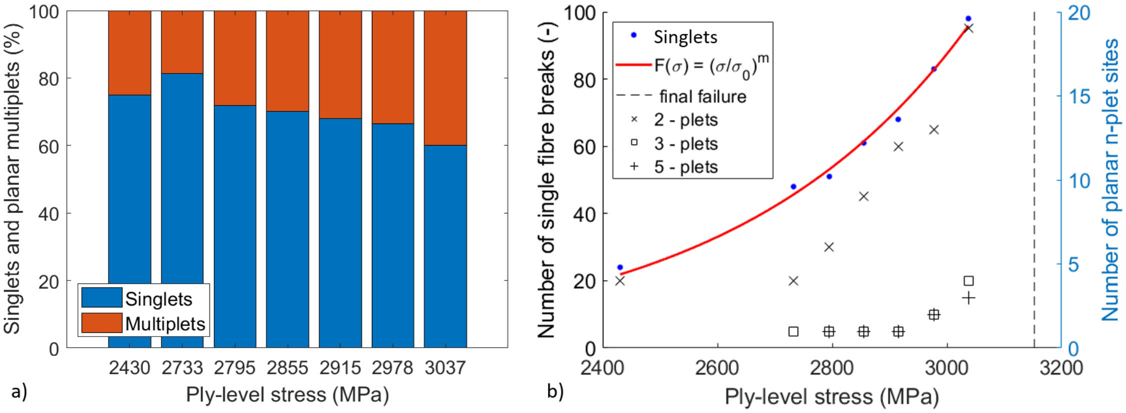

Figure 5.4. Coupon E 1 break behaviour as a function of ply-level stress: a) proportions of singlets and multiplets; b) singlet, 2-, 3- and 5-plet count.

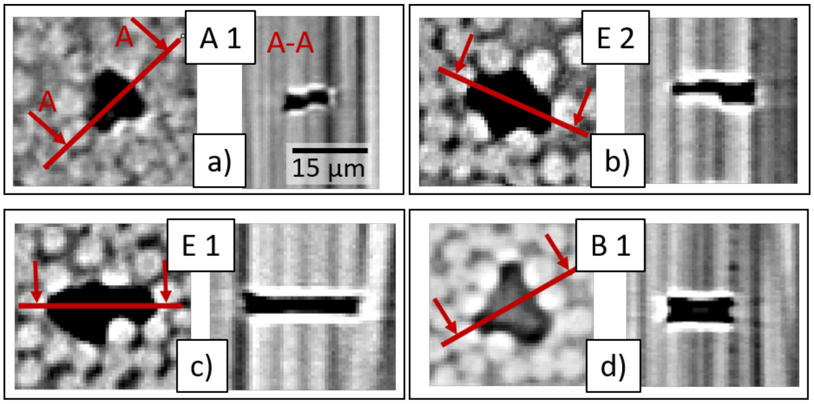

Figure 5.5. Examples of planar multiplets as extracted from the CT scans on two orthogonal views. In a) a 3-plets as seen in coupon A 1; in b) a 4-plet in coupon E 2, c) a 5-plet in coupon E 1 and in d) a 6-plet in coupon B 1 are shown.

5.5.2 Post-mortem coupon assessment

A qualitative and quantitative post-failure analysis of coupon C 1 has been performed (scan location and settings have been described in Section 5.2.2). In a volume of ∼0.1 mm^3, the singlet and planar multiplet counts have been evaluated and are discussed further in section Section 5.5.3. In the current section, a qualitative analysis of the multiplet geometries observed in the volume below the crack profile is reported. A few cases of multiplets connected to the main fracture surface (of which a 3D representation is reported in Fig. 5.1) are shown. In the majority of cases, 2-plets and 3-plets were the deepest break arrangements seen to directly connect to the main fracture surface, i.e. these represent the furthest point reached by the fracture surface, in the fibre direction. Several singlets were observed in the same region, but none connected to the main crack that showed only a few fibres pulled-out. In Fig. 5.6 and Fig. 5.7 respectively, examples of multiplets connected and not connected to the main crack surface are shown. The morphology appears as complex, with multiplets arising in both high and low local volume fraction regions, for 2-, 3- and 4-plets. In Fig. 5.7, a 4- and a 5-plet not connected to the main crack are shown. These appear in a quasi-linear arrangement, located in locally low volume fraction regions and close to the layer edges.

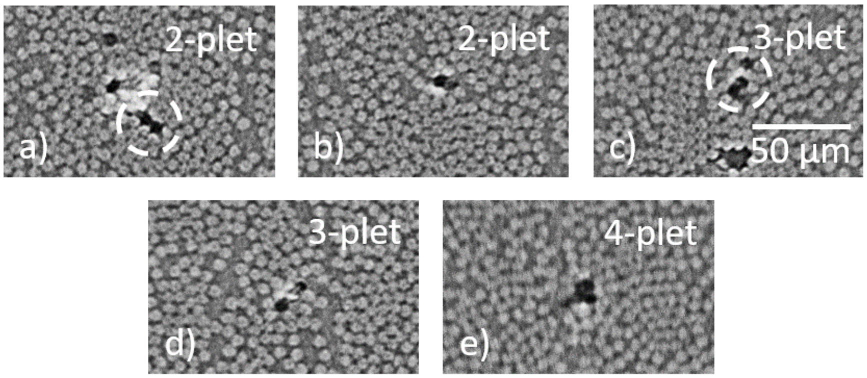

Figure 5.6. The morphology of the 2-, 3- and 4-plets connected to the main fracture surface appears as complex. High and low volume fraction regions can be observed.

Two more observations from the post-mortem scans are provided in Fig. 5.8 and Fig. 5.9. In Fig. 5.8a, an example of two multiplets connected to the main crack surface is shown. Moving towards the mean fracture plane in the fibre direction, the multiplets are seen to aggregate to form a larger crack. This crack enlarges to include tens of fibre breaks and joins cracks formed in other layers, as shown in Fig. 5.8b. In Fig. 5.9, image slices are shown at 50-100 μm intervals from a 2-plet seen at ~500 μm below the mean fracture plane, back to the mean fracture plane. In Fig. 5.9a to Fig. 5.9h, the same fibres are observed and the crack development followed. In Fig. 5.9a, a 2-plet is observed, that evolves into a 5-plet moving towards the mean fracture plane in Fig. 5.9b. In Fig. 5.9c, several small multiplets are observed in the vicinity, from which coalescence into a large crack originates, as shown in Fig. 5.9d. Moving 100 μm towards the main crack plane, in Fig. 5.9e a large crack is formed and

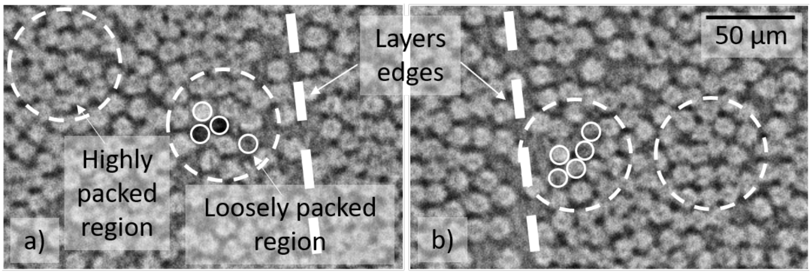

Figure 5.7. a) A 4-plet and a b) 5-plet not part of the final fracture surface, as observed in the post-mortem CT scans. The two multiplets share: i) a close-to-linear geometry, ii) a close-to-the-edge of the layer location and iii) are positioned in a relatively low volume fraction region. Fibres are circled in white as the breaks are not all on the same plane, hence visible on a same CT image (the distance between breaks is lower than a fibre diameter, allowing to catalogue these as planar multiplets).

stabilised in dimension (for tens of μm) and contained in a single prepreg layer. In Fig. 5.9f, 100 μm below the main crack plane, the large crack links to another crack formed within the same layer, through a resin rich area as shown in the enlargement of Fig. 5.9f (size is 130x130 μm). In Fig. 5.9g, the crack connects to other cracks outside the layer of formation, as better shown in Fig. 5.9h), at the mean fracture plane.

The implications of these examples are not clear. As observed in [23] for the T700/M21 configuration, weaker interfaces can lead to more dispersed failure, resulting in a brush-like fracture surface. A fracture profile that develops in the axial direction, as shown in these images, represents a relatively diffuse failure profile suggesting a weak interface. However, as shown in Fig. 5.10, the crack profile seen in both the in-layer and out-of-layer views, shows several cases of bundle debonding that can arise when the interface is too strong for individual debonding to occur. A complex crack path is related to fibre strength variation and fibre/matrix debonding.

Conversely, the small multiplets that represented the furthest points reached by the crack profile away from the mean failure plane, could have formed before the final failure, and represented a lower energy path, combined with extensive debonding and splitting, for the macroscopic crack to propagate across the whole cross-section of the coupon. This uncertainty regarding mechanisms emphasises the importance of future work to capture the actual macroscopic failure region prior to final failure.

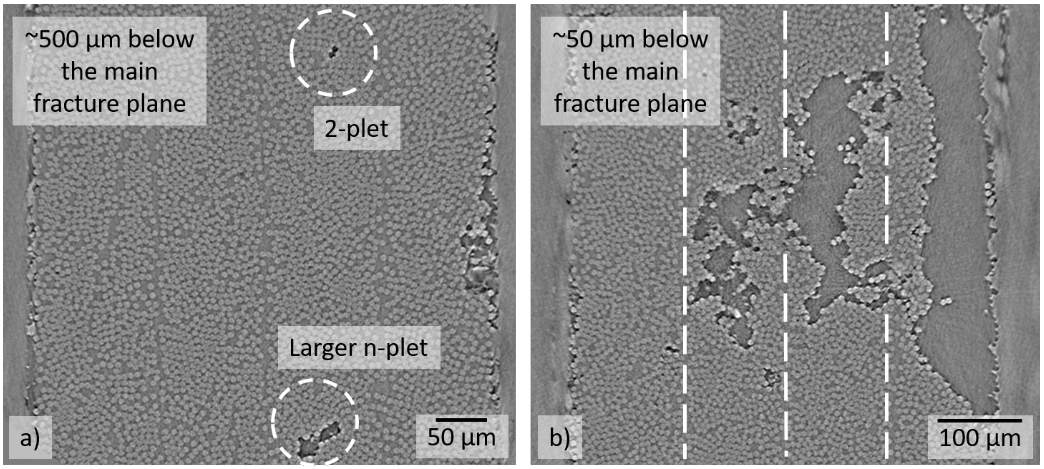

Figure 5.8. a) Multiplets connected to the main fracture surface, located in high volume fraction regions, ∼500 μm below the mean fracture plane. 2 plets are the most common features observed in the farthest damage sites from the mean failure plane measured parallel to the the fibre direction. N-plets, such as those shown in a), have not been observed to propagate over the layer edges (white dotted lines in b)) moving in the axial direction towards the main crack surface, until not fully developed as in b).

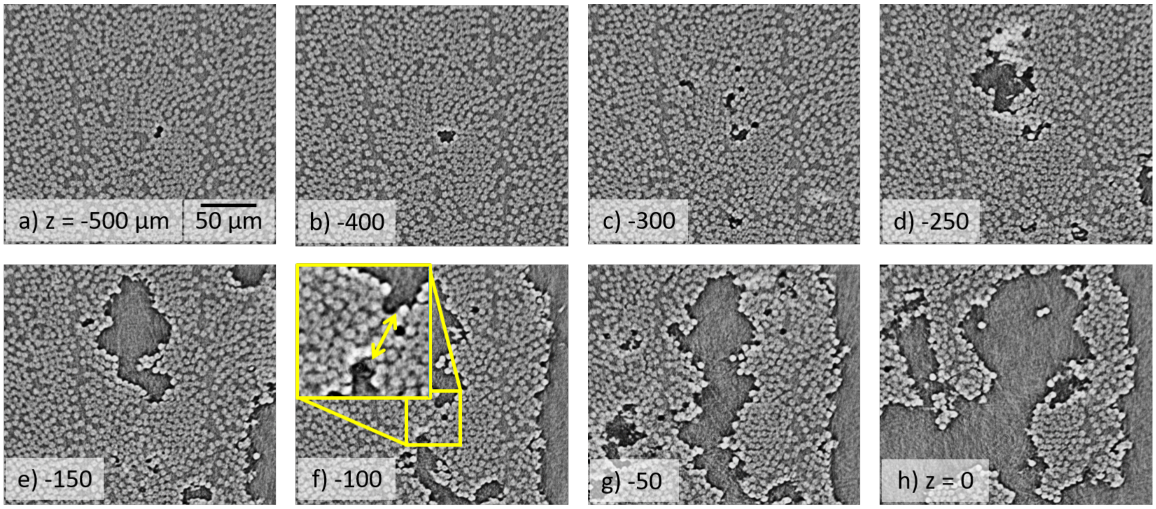

Figure 5.9. How a 2-plet connects to the main fracture surface of the coupon at a distance of 500 μm below the crack surface.

This requires a certain amount of good fortune and persistence as the exact failure plane is not known *a priori*, and the fields of view are small if individual fibre breaks are to be imaged.

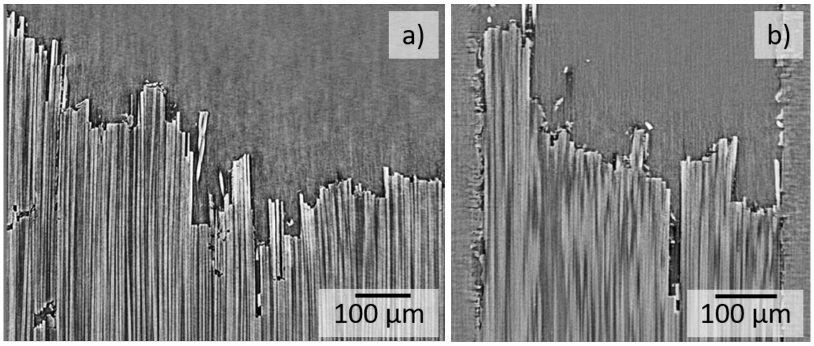

Figure 5.10. The crack profile has been assessed in the two orthogonal directions: a) in-layer direction and b) out-of-layer profile. The profile indicates that there are relatively few individual pulled out fibres, with most steps on the fracture surface composed of at least two adjacent broken fibres.

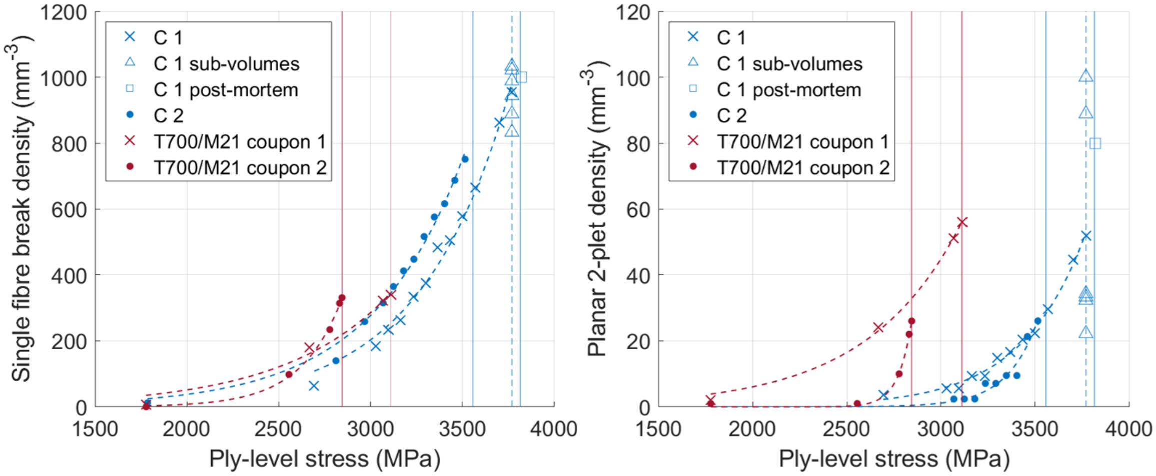

Figure 5.11. The fibre break (planar multiplet sites not included) and the planar 2-plet densities as a function of the stress in the load-bearing reduced cross section are plotted for the Material C and the T700/M21 material configuration studied by Garcea *et al.* and Scott *et al.* in previous SRCT test campaigns ([22, 31]). T700/M21 data is extracted from [22] and has been obtained through continuous monotonic loading and scanning, while 90% of the applied load was held during the scan duration (approx. 2.5 min) on the C coupons.

5.5.3 Fibre break assessment in the post-mortem coupon

Fibre breaks were counted in the post-failure volume, obtained by scanning coupon C 1 below the macroscopic failure surface. No automated fibre break extraction was possible in this case, as no load was applied on the failed coupon and the residual fibre-break opening displacement is greatly reduced. This leads to most fibre breaks assuming a grey scale value close to that of the surrounding matrix rather than being completely dark and easily detectable, as in the *in situ* scans. In a volume of ~0.1 mm^3, a total of 93 breaks was detected after three manual counts. Twelve planar multiplets have been observed of which eight were 2-plets, three 4-plets and one 5-plet. This is translated to an average density of ~1000 breaks/mm^3 and ~80 2-plets/mm^3 observed in the analysed volume below the main crack profile. These values are higher than those observed in the site scanned before failure at 96.4% coupon UTS located in the notched region, ~3 mm far from the post-mortem scan location, in the axial direction, as shown in Fig. 5.1. In Fig. 5.11, the accumulation of singlets and 2-plets is reported for coupons C 1 and C 2 and two coupons cut from a T700/M21 prepreg plate. Coupon UTS values are indicated with a vertical line: respectively at 3814 MPa and 3557 MPa for C 1 and C 2, and 2844 MPa and 3111 MPa for T700/M21 coupons 1 and 2. Denoted by the squared symbol, are the singlet and planar 2-plet densities extracted from the post-mortem volume.

The data from the commercial aerospace-grade thermoplastic particle toughened carbon/epoxy T700/M21 from Hexcel HexPly is compared to the fibre break accumulation curves of Material C. The first dataset on the accumulation of fibre break of T700/M21 was reported in [22], then in [31], and several models were tested against it ([24, 100, 101, 112]). Hence, the accumulation trends for the singlets and planar 2-plets are reported here as extracted from [31]: the *in situ* tensile tests were performed using a similar geometry to that used in the current study, tested through a continuous monotonic loading and scanning (while 90% of the applied load was held during scanning time of ~2.5 min on the coupons tested in the current study).

The higher acquisition frequency has the advantage of allowing better damage progression tracking: scans in [31] have been collected until 99.9% UTS, very close to the last moment preceding the macroscopic failure of the coupons. The drawback is a compromise in signal to noise ratio, due to less projections being acquired [31, 143]. Since the purpose of the present test campaign was to obtain a high fidelity representation of the local morphology in the fibre break sites, a step wise acquisition was preferred over this technique, as it provides higher quality images. The continuous approach adopted in [31], by avoiding interruptions and hold-at-load, would ensure no additional damage is introduced while scanning. This additional damage has been extensively described in [27], but it should be noted that the load has been systematically reduced by $\sim$10% (i.e. always kept below 90% coupon UTS) before scanning to reduce the effects of the matrix relaxation while keeping the broken fibre ends apart and thus ensuring that breaks are easily detectable and the coupons compared in this study have a comparable number of scans collected, i.e. kept loaded for a similar amount of time, leading to similar testing conditions in the analysed batch.

Adding the two coupons continuously scanned (with focus on the last two data points prior to failure) allows us to suggest that the accumulation of both singlets and planar 2-plets follows a power law curve until 99.9% UTS is reached. Therefore, the jump in 2-plet count observed for coupon C 1 between the prior-to-failure and post-mortem scans (last two points of the 2 plets accumulation of coupon C 1 in Fig. 5.11) might be related to some dynamic stress release due to the catastrophic failure and not only to the accumulation of 2-plets missed between the scan collected at 96.4% coupon UTS and 99.9% coupon UTS.

The smaller dimensions of the post-mortem scans (volume of $\sim$0.1 mm^3 vs. 0.54 mm^3 for the prior to failure scans) might have affected the results. Hence, the prior to failure scan volumes have been divided into six smaller sub-volumes, of the same volume of the post-mortem scan. In these, the density of fibre breaks is evaluated: the six values are plotted with a triangle symbol in the plots of Fig. 5.11. It is observed that while the singlet count does not vary much, with a standard deviation of 79 fibres/mm^3 (representing the 8.3% of the total break count), in the planar 2-plet counts a wider scatter is observed with a standard deviation of 33 2-plets/mm^3 (representing 64% of the 2-plet count). This means the value observed post-mortem could be reasonable for a locally higher break density region. However, the question remains open and larger volumes and more coupons should be scanned post-mortem to clarify whether final failure is a smooth extension of damage accumulation or whether there is a burst of additional damage at the point of catastrophic failure.

During the macroscopic failure process, the energy release involved is likely to cause additional damage in the composite micro-structure. The jump in the number of 2-plets, that is not seen in the singlet count, could be explained by the hypothesis that this final multiplet formation is a consequence of a rate effect. The failure of the fibres involved in 2-plets is likely to happen at a high rate and it could be speculated that the rate of the final failure at the fibre/matrix interface does not provide sufficient time for the interface to debond and slide, leading to an increased likelihood of neighbouring fibre breakage. Instead, when loading with a slower elongation rate, this could be less likely to happen. The singlet formation could be more associated with incremental loading (hence the comparable number of singlets ante- and post-mortem observed in Fig. 5.11a), where the formation of planar multiplets could be more related to the rate of debonding and sliding. ‘Stabilised’ multiplets can form:

(a) as a natural statistical consequence of the fibre strength distribution, i.e. most fibres have a sufficient strength to withstand the applied stress and only the weakest fibres break, and occasionally these happen to be near to each other;

(b) due to the existence of some mechanism by which the stress concentration factor (SCF) around the broken fibres can change from a high to a low value. This could be attributed to a:

    (i) dynamic stress wave, which exists for a few nanoseconds when the first fibre breaks, but then dissipates, or

    (ii) fibre/matrix interface shear or separation which occurs once the multiplet reaches some critical length.

Processes i. and ii. might be coupled, i.e. interface shear or de-cohesion are time dependant as they involve the matrix (which is visco-elastic). The following phenomenon could then potentially occur: dynamic loading allows a multiplet to grow to some specific size. It then stops, and the resultant multiplet ’edge’ (which is highly loaded) undergoes time dependent matrix processes, further shielding the adjacent fibres from stress concentration.

5.6 Conclusions

The major contribution of the present work is to make quantitative data and qualitative observations of the micro-mechanisms related to the longitudinal tensile failure of fibre-reinforced polymers available to the modelling community. About 250 multiplet clusters of fibre breaks have been examined in tensile loaded micromechanical coupons prior to failure and post-mortem. Coupons cut from prepreg laminates made of similar materials adopting controlled variations of surface treatment, sizing agent and fibre type have been analysed and the multiplet accumulation has been tracked to characterise these critical features.

Variations in the multiplet topology have been identified as an indication of how damage accumulation is sensitive to small variations in specific parameters. Of the multiplet geometries analysed in this study, only 2-plets and 3-plets have been observed in sufficient numbers to merit detailed quantitative analysis, with a 6-plet being the largest multiplet detected in any of the materials tested prior to failure. The multiplet formation seems to be primarily influenced by the fibre type and the level of adhesion at the fibre/matrix interface, with the highest percentage of multiplets being observed in the material featuring the strongest fibre/matrix interface and the highest Weibull modulus fibres, which is consistent with the higher values of local stress concentrations expected on the plane of the fibre breakages and the fibres being more likely to break at closer stress levels to each other [14, 70].

Of the four configurations adopting the same fibre type, the configuration containing the strongest interface exhibits the highest level of multiplet formation at the lowest stress level, corresponding to its lower average UTS. It is shown that within the configurations tested, a change in fibre surface treatment is more critical than the sizing, in that for a given applied stress multiplets are less extended and larger multiplets are accepted without necessarily leading to final failure of the coupon.

One of the analysed coupons (coupon C 1) has been scanned post-failure adjacent to the macroscopic fracture surface and a fibre break assessment has been performed in the imaged volume. The post-mortem fibre break count agrees to with that estimated by extrapolating a power law curve fitted to the fibre fracture accumulation prior to failure.

(This page was intentionally left blank)

CHAPTER 6

STATISTICAL MEASUREMENTS OF THE LOCAL MORPHOLOGY

Models are still deficient in accurately reproducing the mechanisms that trigger tensile failure in unidirectional composites, highlighting a lack of direct experimental evidence. In this study, emphasis is given to the identification of connections between local fibre misorientation, packing and Weibull strength distribution in causing tensile failure. Synchrotron Radiation Computed Tomography (SRCT) and automated image processing techniques are adopted to segment individual fibres from loaded carbon fibre coupons. Subtle indications in the misorientation of local damaged sites are assessed in novel statistical detail for systematic differentiation from non-damaged sites. It is observed that the morphology of the surrounding environment of damaged sites statistically differs from that of non-damaged sites, even though locally damaged sites (containing single or coupled breaks) do not exhibit a peculiar fibre packing arrangement. For adjacent coupled breaks, the statistical nature of fibre separation distances is also reported.

6.1 Introduction

Polymer matrix composites represent a diverse class of materials widely used in transport applications for their high specific properties and adaptability. Models predicting the failure performance of such materials for engineering purposes are not well established however, leading to over-engineered and hence heavier, larger and more expensive components [52]. This has been attributed to the complex micro-mechanical interactions within and between the matrix, reinforcing fibres and multi-orientation laminar layups, engendering multiple potential damage modes within any given component, e.g. matrix cracking, fibre/matrix debonding, micro-buckling, delamination and fibre failure [32]. Attempts to predict the failure of multi-directional composites under different loading conditions have been extensively tested within the World Wide Failure Exercises (WWFE) I, II, III [12, 171] in which numerous modelling strategies have been assessed in detail and compared to reference experimental data sets. The results showed a significant spread in the predictions, highlighting the need for many model input properties (often difficult to measure), as well as challenging experimental validation [52]; a simpler approach might be preferred to capture correctly the fundamental mechanisms. Within a multi-orientation laminate, it can be expected that the ultimate tensile strength will be limited by essentially simple tensile separation of the 0^o plies (i.e. plies aligned with the primary tensile load) [14, 32]. This process has been analysed historically, with various modelling strategies reported in the literature based on essentially the same fundamental assumed mechanisms [76, 83]:

- Within a given 0^o ply, as the longitudinal stress increases, failure of the weakest fibres occurs (according to a statistical strength distribution [48]), generating stress concentration on immediately neighbouring intact fibres.
- As loads increase, fibres neighbouring breaks are more likely to fail than those in the surrounding micro-structure, leading to local clustering of breaks.
- From this, a cascade effect is eventually achieved, where a critical cluster of broken fibres grows in an unstable, self-sustaining manner.

In this context, the local role of the matrix is to load in shear and transfer the stress back onto the broken fibre, as well as to transfer stress onto the fibres surrounding the broken one, generating stress concentration on these for a certain distance from the break position along their length. In the literature, this is indicated as the ineffective length [37] with experimental measurements for carbon fibre reinforced polymers (CFRPs) provided by Scott et al. [22], as an example.

Although the process of fibre break accumulation can be seen as conceptually simple, various issues arise in the corresponding predictive models, for example, the experimental determination of appropriate Weibull distribution parameters and the approximations used to model the fibre and matrix mechanical behaviour. The latter commonly entails the assumption of the fibre and matrix being linear elastic, and the fibre/matrix interface being intact, in the simplest case. In reality, the matrix shear yields or cracks and fibre/matrix interface debonding is often observed in composites with poor adhesion [52]. Commonly made assumptions in strength models are extensively described by Swolfs *et al.* in [14], including alternative representations of fibre packing, stress redistribution around single and multiple fibre breaks, and the potential influence of dynamic stress concentrations. Other assumptions that have received little attention in the literature until now may also be identified in stress variation within the cross-section of intact fibres surrounding breaks, the incidence of planarity (or non-planarity) of groups of breaks (some models assume full planarity of groups of breaks [79]). Assumptions vary regarding the onset of unstable break clustering causing final failure (whether it should be a fracture mechanics approach rather than a stress-based one), whilst Swolfs *et al.* further identify the absence of local fibre micro-structure in contemporary models.

Models that predict the accumulation of interacting fibre breaks can be retrieved in the literature and to be cited are the hierarchical scaling law [101]; the spring element models [90, 95, 172] (inspired by the Zhou and Curtin's lattice Green's function model [87]) and following evolutions of this model that include dynamic effects on the break formation, such as [99, 100]; the direct numerical simulation method that used a fibre-bundle model similar to the above-mentioned spring element model [26, 52, 173]; the multi-scale FE^2 model that uses the FE analysis of composites at the micro-scale and includes time-dependent visco-elastic effects and homogenisation methods [28–30, 60, 111]. These models have been tested against experimental results and in some cases a good agreement with the single fibre break predictions is reached (as reported in [32, 99]), while the clustering prediction is still inaccurate, suggesting a higher level of understanding of the features governing the longitudinal tensile failure of composites is needed. Despite fibre strength distributions clearly playing a key role in strength models, the significance of the assumptions outlined above is not clear. Hence, in this study we have performed a detailed analysis of local fibre micro-structures, with a view to providing statistically significant indications of potential influence on the formation of single fibre breaks, and groups of closely interacting breaks. Focus is given to planar coupled breaks: since they are available in a good amount in the collected data to draw statistical conclusions, and since, according to the majority of models, should play a crucial role in increasing the stress concentration around a break site and the recovery length if compared to diffuse clusters of breaks [120], and as predictive models are still deficient in accurately tracking their formation and evolution, as noted in [24] where the results of an SRCT experimental campaign were compared to the modelling predictions. In this respect, in situ X-ray SRCT has emerged in the last decade as a unique tool to quantify micro-structure and damage in composite materials, and follow the chronology of damage progression, providing the modelling community with novel experimental validation opportunities at a micro-mechanical level.

In studying the morphology of continuous fibre composites via computed tomography, previous studies have assessed the presence of misorientation in carbon fibre reinforced polymers (CFRPs). A multiple field image analysis method was adopted in [174], well suited for coupons with pronounced waviness, while a method applicable to small volumes with limited amount of fibres was adopted in [175]. However, no results are presented on *in situ* following the damage accumulation. Emerson *et al.* ([176]), have reached a fibre-by-fibre detection level, characterising orientation in glass and carbon fibre composites from relatively low contrast images, and presented quantitative results on the axial compression of composites in [21]. Where Emerson's algorithm comprises a training process to generate a dictionary that reduces the degree of false centre detection, in this study a simple Otsu's threshold ([165]) has been shown to track fibres accurately. Although in both cases about 7 pixels covered a fibre diameter, the approach used in the present work can be justified by the better quality of the scans obtained through SRCT rather than laboratory-CT (beam is brighter, monochromatic, more coherent and parallel providing less noisy images, with a higher level of phase contrast and absence of beam hardening artefacts [143]). However, where Emerson's algorithm is proven to accurately track fibres over lengths of millimetres and focus on larger lengths to analyse the fibre orientations, focus is here given to shorter lengths (below 100 μm) and to the centre detection accuracy within the cross-section of a fibre, checking at a sub-micron level with a meticulous error trapping approach. In this study we exploit previously presented damage monitoring methods (see [22, 31, 127], and, to the authors knowledge, provide the first automated approach to quantify at the individual fibre level the local micro-structure at single and groups of adjacent fibre breaks locations in statistically significant numbers. By combining for the first time SRCT, automated image processing techniques and statistical tools, the study represents a first step towards a full micro-structural analysis of composite coupons in situ tested using SRCT, that can inform on the geometry of large groups of interacting fibre breaks, believed to drive the longitudinal tensile failure mechanisms in composites. The damage progression is not only followed in terms of fibre breaks from low to high applied strains but also the morphology of all the fibre break sites is captured prior to failure. The results of the method adopted for the analysis in this study show that it is possible to capture subtle indications in the fibre misorientation and spacing distributions in the single fibre break and intact sites, as these are features available in sufficient amount in the analysed material. Nevertheless, where possible results will be also presented on coupled planar breaks, that represent the planar features still observable in a small-to-average amount to draw statistical conclusions. The final aim will be to perform a test campaign that captures a higher number of large n-plets, believed to drive the longitudinal tensile failure mechanisms in composites and statistically observe their morphology comparing it to the morphology presented in this study of non-damaged, single and coupled fibre break sites. This could benefit future experimental analyses, e.g. in recognising a priori areas of peculiar morphologies that could be in situ followed from low to high strain for group of interacting fibre break formation that could lead to the failure and inform the modelling community on uncharacteristic morphologies (e.g. regions of fibre waviness, entanglement or resin rich regions) that should be included in the models to fully capture the mechanisms leading to longitudinal final failure of composites.

6.2 Materials and experimental procedure

6.2.1 Materials

$(90_2/0_2)_s$ laminates were produced from Mitsubishi Chemical Co. carbon fibre pre-preg to the manufacturer's specifications; the nominal fibre diameter was 5.4 μm and the tensile modulus 289 GPa. The tensile strength follows a Weibull distribution, with a shape factor of 5.47 and a scale factor of 11.29 GPa, at a gauge length of 5 mm (see Table 4.2). The average strength calculated by Weibull distribution is of 8.07 GPa. This matches the experimental average strength of 7.76 GPa. 1 mm thick double edge notched tensile test coupons were realised via water-jet cutting, as indicated in Wright *et al.* [127]. Aluminium tabs were carefully glued to ensure alignment of the sample during tensile loading in the electro-mechanical rig. The average ultimate tensile stress (σ_f) measured across the notched section was 3.47 GPa. Two coupons were investigated in this study (identified as Coupon 1 and Coupon 2), to assess levels of reproducibility. About 8000 fibres were present within the notched region, with a gauge length of ~1.3 mm being imaged in the field of view of the scans.

6.2.2 Experimental procedure

In situ tensile tests were performed at the European Synchrotron Radiation Facility (ESRF) in Grenoble, France (ID19 micro-tomography beamline). A modified DEBEN CT5000® tensile stage was used to carry out the tests, as reported previously [169]. The central notched region of the coupons was initially scanned at ~50% and ~80% of the nominal average ultimate tensile strength (UTS) for the coupon geometry, with at least ten more scans being collected between ~80% UTS and final tensile failure of the coupon. Tests were carried out at a displacement rate of 0.2 mm/min, being halted briefly for each scan (individual scan duration was ~2.5 min), the tensile force was backed off by ~10% during the scan, for mechanical stability and to optimise image quality for subsequent quantitative analysis.

Voxel resolution provided by the optics in this study was ∼0.65 μm (sufficient to observe individual fibre breaks) with a field of view of ∼1.3 mm, in which a 3D representation of the imaged volume for all the scans is shown. Exposure time was 50 ms and the number of projections 2996. A multi-layer monochromator was used ($\delta E/E \sim 10^{-2}$) at an energy of 19.5 kV and sample-to-detector propagation distance of 50 mm (near-field Fresnel/edge enhancement regime). Crack opening due to fibre breaks was well in excess of the voxel size for all the collected volumes of scans, with breaks being readily detected via automated approaches.

6.3 Image Analysis

Automated image processing was carried out in ImageJ^{TM} and MATLAB®. Fig. 6.1 illustrates the approach adopted to observe fibre misorientation at individual damaged sites, as explained below.

6.3.1 Individual fibre tracking and sub-volumes extraction

An ImageJ^{TM} ([177]) macro is used to load the last collected volume of a given set of sample scans, just prior to failure, which thresholds the fibre break sites and save information on their morphology (spatial coordinates, dimensions, volume, orientation, etc.). Based on this, a MATLAB® script catalogues the breaks into singlets and planar duplets (see Section 6.4). Given the number of planar multiplets observed (∼3 to 5% of all break sites) and their complex geometry, a final visual inspection of these sites allows the user to visually confirm the automated measurement of the number of fibres associated with each site. A second MATLAB® script that uses the Image Processing Toolbox [178], takes the last collected scan volume prior to failure and extracts for each fibre break site a sub-volume centred on the break that includes some 30 to 50 fibres surrounding the broken one, ∼0.65 μm long, as shown in the blue box in Fig. 6.1a. The script also extracts sub-volumes at coupled fibre break locations and a randomly selected set of intact locations, separate from break locations and from each other to be reasonably uniformly distributed through the whole volume (see Fig. 6.1a,b). Measurements at the intact locations are used to characterise as the 'background' micro-structure of the material. Thus, sub-volumes

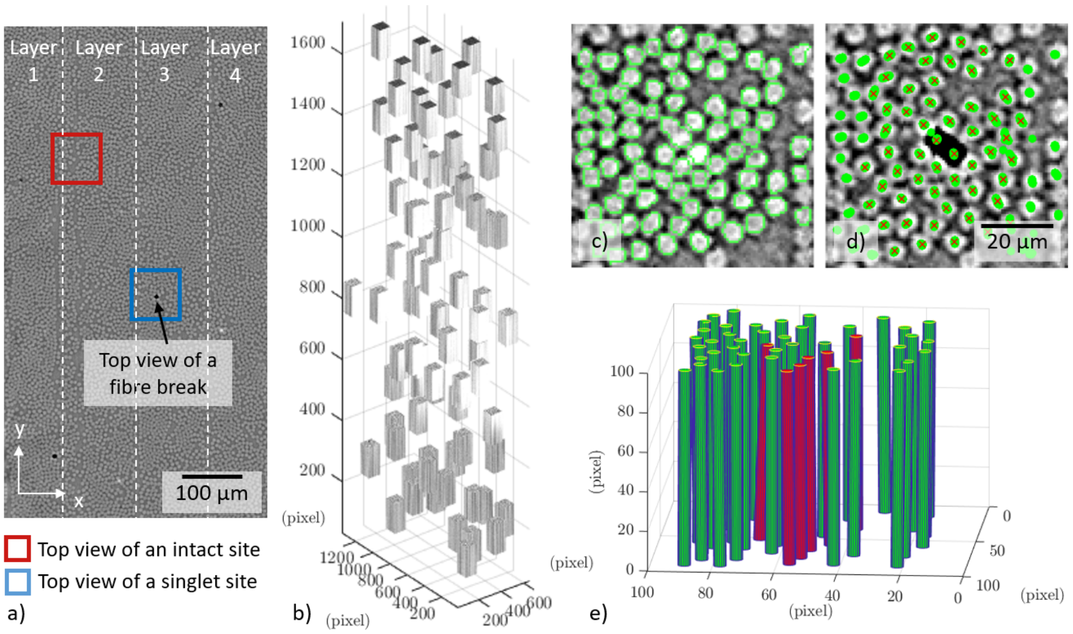

Figure 6.1. Misorientation data extraction methodology: (a) Single top view slice of 0^o ply at high strains (immediately prior to macroscopic failure of the coupon). Locations for sub-volume extraction are centred appropriately between single, coupled fibre break sites or random non-damaged sites. (b) 3D sub-volumes extracted from the scanned volume. (c) Fibre tracking: on a single top view slice of a sub-volume, an image enhancement approach is adopted to segment the fibres. After this, an algorithm recognises and catalogues one by one all the fibres centres in a sub-volume, tracing continuity between all slices, which effectively removes occasional false detection on a single slice or occasional small group of slices. (d) in black at the centre of the image, two co-planar breaks - red crosses indicate candidate fibres location used in the tracing analysis. (e) Fibres in a sub-volume are visualised: more misaligned fibres (misorientation greater than 1.50^o with respect to loading direction) are here represented in red; in green, fibres having a lower degree of misorientation.

are divided into: sub-volumes centred on a single fibre break (hereafter indicated as ‘singlet sites’), damaged sub-volumes centred on two planar adjacent breaks (‘duplet sites’) and sub-volumes containing non-broken fibres (‘intact sites’).

Within a sub-volume, the ‘imadjust’ function is used to enhances the contrast of the images containing the top views of the fibres prior filtering with the ‘imgaussfilt’ function: a 2-D Gaussian filter that reduces the contrast but at the same time lowers noise within the resin regions, which is the principal cause of false fibre detection.

The fibres are then morphologically opened with the ‘imopen’ function: an erosion followed by a dilation, using the same disk-shaped structuring element to facilitate the fibre thresholding. After this, the ‘imbinarize’ function is adopted to threshold the fibres by means of a globally determined threshold value obtained with Otsu’s method [165]. Finally, the ‘regionprops’ function provides the centre of each fibre detected in the 2-D slice. Fibres are segmented on every tenth slice (perpendicular to the fibre direction, as indicated in Fig. 6.1c), for a total of ten steps spaced 6.5 μm from each other. The ‘rangesearch’ function is adopted that works as follow: for each fibre centre in slice i, its correspondent is found in slice i+1 that has a difference in coordinates of less than a certain distance (initial tests showed 2 pixels, equivalent to 1.3 μm was a good compromise for the analysed material). Two centres of a same fibre detected at an axial distance of 6.5 µm that have a transversal distance larger than 1.3 μm are rejected, i.e. an angle with the vertical loading direction of more than 12^o is not accepted: fibres in this study have been observed to have a degree of misorientation that can reach up to 8^o with respect to the vertical direction of the CT scans.

If a centre is missed on one slice, the script keeps the same coordinates of the centre and moves to the next slice. The ‘regionprops’ function provides the coordinates of the centre of a fibre with four decimal digits. If these digits do not change for at least half the number of slices investigated, then this fibre candidate is rejected. The results of the script have been visually checked for 40 sub-volumes containing an average of 55 fibres each on a total of about 2200 analysed fibres, showing the following errors: 7 false negatives and 7 false positives, representing an error of 0.006% in fibre detection. Detected fibre centres are connected by linear interpolation, and fibres recognised and catalogued individually. Sub-volumes are slightly larger than needed to ensure fibres in the area of interest are well tracked as shown in Fig. 6.1d, where the fibres assessed in relation to the central duplet (in black at the centre of the image) are indicated with a red cross. Fig. 6.1e illustrates fibres from a typical single sub-volume, where fibres with a misorientation greater than 1.5^o (with respect to the coupon loading direction) have been distinguished in red from their more closely aligned neighbours (green).

6.3.1.1 Estimation of fibre orientation errors

Sub-pixel accuracy in fibre tracking is achieved by fitting to centroids measured on multiple slices, following the fibre trajectory and, ameliorating local errors/noise in the centre detection on any one slice of within a sub-volume. Linear regression is adopted to get the best fit of the fibre centres. The linear regression is separately applied to the x coordinates of the fibres and then to the y coordinates obtaining a smooth straight shape for each fibre. Mean R^2 values evaluated for a sample of 2500 fibres extracted from Coupon 1 were of 0.65 and 0.71, respectively in x and y directions, with a standard deviation of 0.30 and 0.31. However, the correction given by the linear regression approach was always well below a pixel size. A visual approach was adopted for which fibres have been checked in the scanned volume and within a length of about 100 μm (well in excess of the 65 μm of the sub-volume length): fibres appeared as straight and did not show any signs of waviness. This was checked on a large number of sites (∼40). As a further error check step, the sub-volume length is changed from 65 to 52 and then 78 μm. If fibres are correctly detected, their misorientation should be identical if detection is done on a smaller or larger length, i.e. detection performed on a lower or higher number of slices should lead to the same fibre misorientation. An example is shown in Fig. 6.2a: varying lengths of fibre are presented for single broken fibre sites. Over 100 sites with 40 by 40 μm cross-sections were assessed. Circular selections centred on the fibre breaks were assessed, containing an average of 7 fibres per site. Fibre misorientation was checked separately in the in-layer and out-of-layer directions, using the displacement between the two ends of the centres of the fibres at the top and at the bottom faces of the sub-volumes, i.e. considering the coordinates (x1, y1, z1), (x2, y2, z2) and calculating for the in-layer direction:

$$\theta_y = \tan^{-1} \frac{y_2 - y_1}{z_2 - z_1}$$

where z_2 - z_1 equals the sub-volume length.

The histograms of the fibre misorientation angles in the in-layer direction for the three different-length sub-volumes centred on the same fibre breaks showed clear superposition. A two-sample Kolmogorov-Smirnov (KS) test has been used to compare

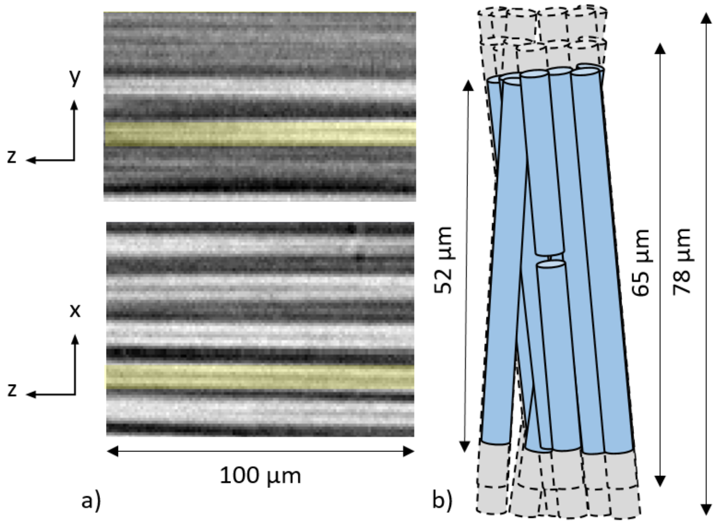

Figure 6.2. The length of the same sites centred on a single broken fibres is varied from 52 to 78 μm. Over 100 sites with a 60 by 60 pixel (about 40 by 40 μm) cross-section were assessed. Fibres were detected in circular selections centred on the fibre breaks, containing an average of 7 fibres per site.

the three distributions of data, being a non-parametric method to compare samples, sensitive to differences in location and shape of the samples cumulative distribution functions [179]. The distributions were confirmed to be drawn from the same statistical population (with a p-value of 1.0), i.e. more confidence can be given to the fibre centre detection, as changing the tomographic slice at which the centre is detected does not change the fibre orientation value obtained. In this study, the number of observations played a relevant role in maximising the statistical value of the work: choosing long sub-volumes effectively reduced space available in the main volumes to extract separate sub-volumes for comparison. Hence, a length of 100 pixels (equivalent to 65 μm) was chosen, allowing a good number of sub-volumes to be extracted from the main scans, but still permitting accurate representation of local fibre orientations.

6.3.1.2 Identification of local micro-structure length scales

For the two analysed coupons, a total number of 199 singlet sites and 23 planar duplet sites were extracted from the main scanned volumes. Given the amount of volume left after the singlet and duplet sites extraction, it was possible to extract a slightly lower number of intact sites (specifically, 183) which did not overlap with any of the break sites.

The length-scale over which patterns of fibre misorientation may or may not affect fibre break events is considered to be unknown here. For example, is one ‘rogue’ near-neighbour fibre sufficient to influence failure, or may disruptions or intersections at tow level lead to local changes in compliance and hence local overload of fibres. Thus, different micro-structural sampling scales have been tested, presuming that too small a sampled region may not capture enough local structure to be mechanistically meaningful, but too large may statistically overwhelm the real micro-structural influence with surrounding unrelated measurements.

In the first instance, a rectangular cross-section was chosen for local micro-structural assessment, for its simple shape and reflection of some expected difference in how in-layer and through-thickness misorientation arise. To assess length scales, different region widths in the through-thickness direction are assessed here, from two fibre diameters (‘Width 1’) to eight fibre diameters (‘Width 4’), see Fig. 6.3. Although all width steps were analysed, focus was given here to Width 2. The rationale for this choice can be found in Section 6.4.3.1.2 where it is shown that this step seems to be enough at a local scale to capture variations between damaged and not-damaged sites When not specified, the following considerations will be based on data extracted from sites having this width. Misorientation angle values were recorded for: the single broken fibres and the fibres surrounding these, the planar coupled broken fibres and the fibres surrounding these, the intact fibres at the centre of the ’intact’ sites and the fibres surrounding these.

6.4 Results and discussion

As noted above, image analysis was carried out for two representative coupons cut from the same CFRP panel (Coupon 1 and Coupon 2). Qualitative observations suggested some influence of fibre misorientation and coordination on damage processes: Fig. 6.4 for example, shows a site of particularly intense damage (2D slice views in Fig. 6.4a-c) where 7 closely associated fibres have been segmented and coloured for clarity (Fig. 6.4d,e). The 3 fibres highlighted in green in Fig. 6.4d all break at 4 sites

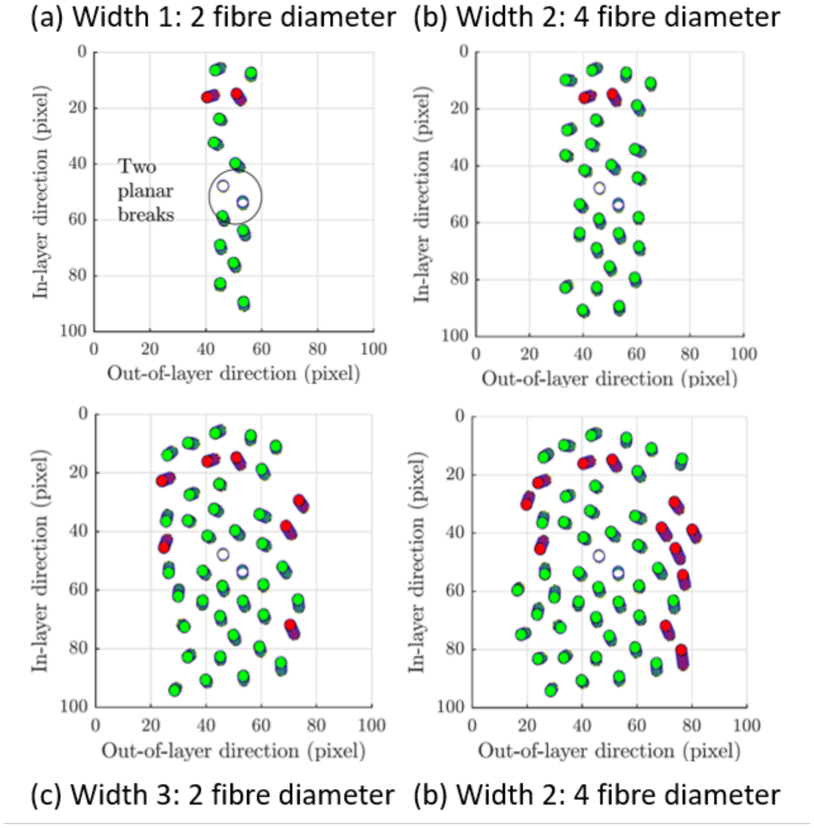

Figure 6.3. Different micro-structural sampling scales have been analysed within a sub-volume (with a different number of fibres being extracted from rectangular cross-sections having the larger dimension parallel to the in-layer direction). Width 1 is of two fibre diameters, increasing of 2 fibre diameters up to Width 4, 8 fibre diameters wide. Although all the width-steps were analysed, width 2 was chosen for the results section, being at a scale local enough to capture variability in the fibre misorientation between damaged and intact sites. Rationale of the choice is described in Section 6.4.3.1.2.

along their length (field of view ∼1.3 mm): as a group, these 3 fibres are seen to be twisted around a number of their neighbours (in yellow), but are in themselves closely packed and retain a consistent coordination with each other. A further fibre that is highlighted in blue is initially separate from green group, but at a point of close approach with the green group, experiences breaks at these same locations. The above-mentioned represent two of the four 4 plets captured in the prior-to-failure scans of the two analysed coupons. No larger multiplets were observed in the analysed scans and for this material configuration. The influence of such specific fibre arrange-

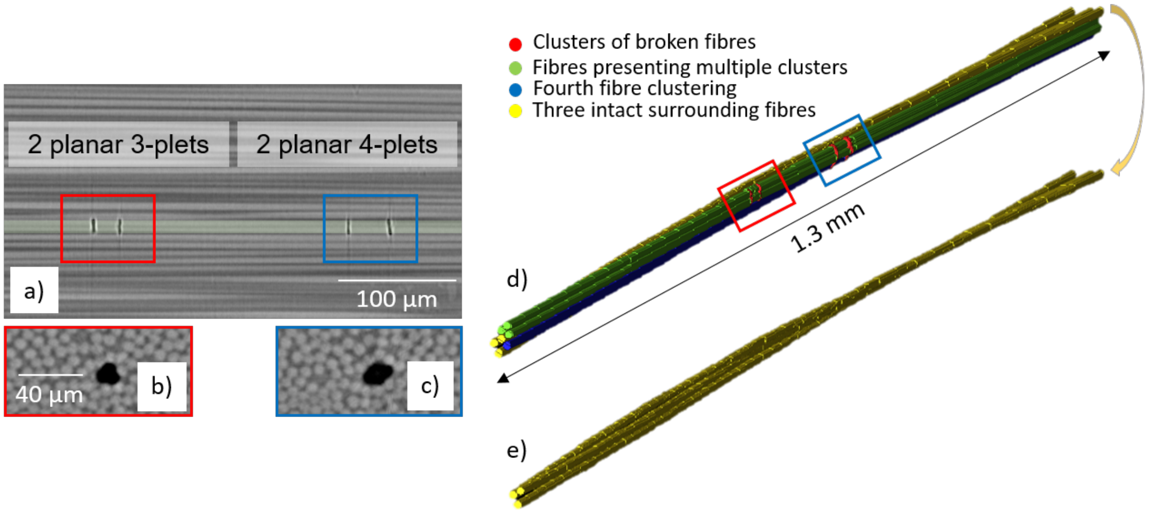

Figure 6.4. Three fibres break four times along their captured length in the field of view of the scans. A fourth fibre breaks twice with them when touching them. In (a-c), the lateral and top view of the adjacent multiplets; in (d) damaged site as segmented from tomographic scans. In green the three fibres breaking four times, in blue the fibre breaking twice with the green ones, when in close proximity (e) the yellow surrounding intact fibres are shown, with their distinctive twisting.

ments might of course be taken forward and investigated by direct micro-structural finite element (FE) simulation [26]. In the first instance, we note that: (a) by eye, there is a high level of self-similarity within the micro-structure, making it difficult to discern if behaviour at a site such as Fig. 6.4 is indeed truly distinctive from the surroundings, and (b) the statistical variability of fibre strengths may be anticipated to superimpose upon local micro-structural influence, complicating apparent causality. As such we believe that break behaviour merits quantitative, statistical analysis of micro-structure at damage sites against what might be considered 'background' undamaged micro-structure, as outlined in Section 6.2. A hypothesis-led approach is therefore adopted. In the first instance, we outline five main comparisons here, as illustrated in Fig. 6.5.

- Hypothesis 1: The orientation of the individual fibres that actually break is distinctive from the general, undamaged micro-structure. As such the fibres that break (i.e. those at the centres of the singlet/duplet sites described in Section 6.3.1), are statistically compared to fibres within intact sites.

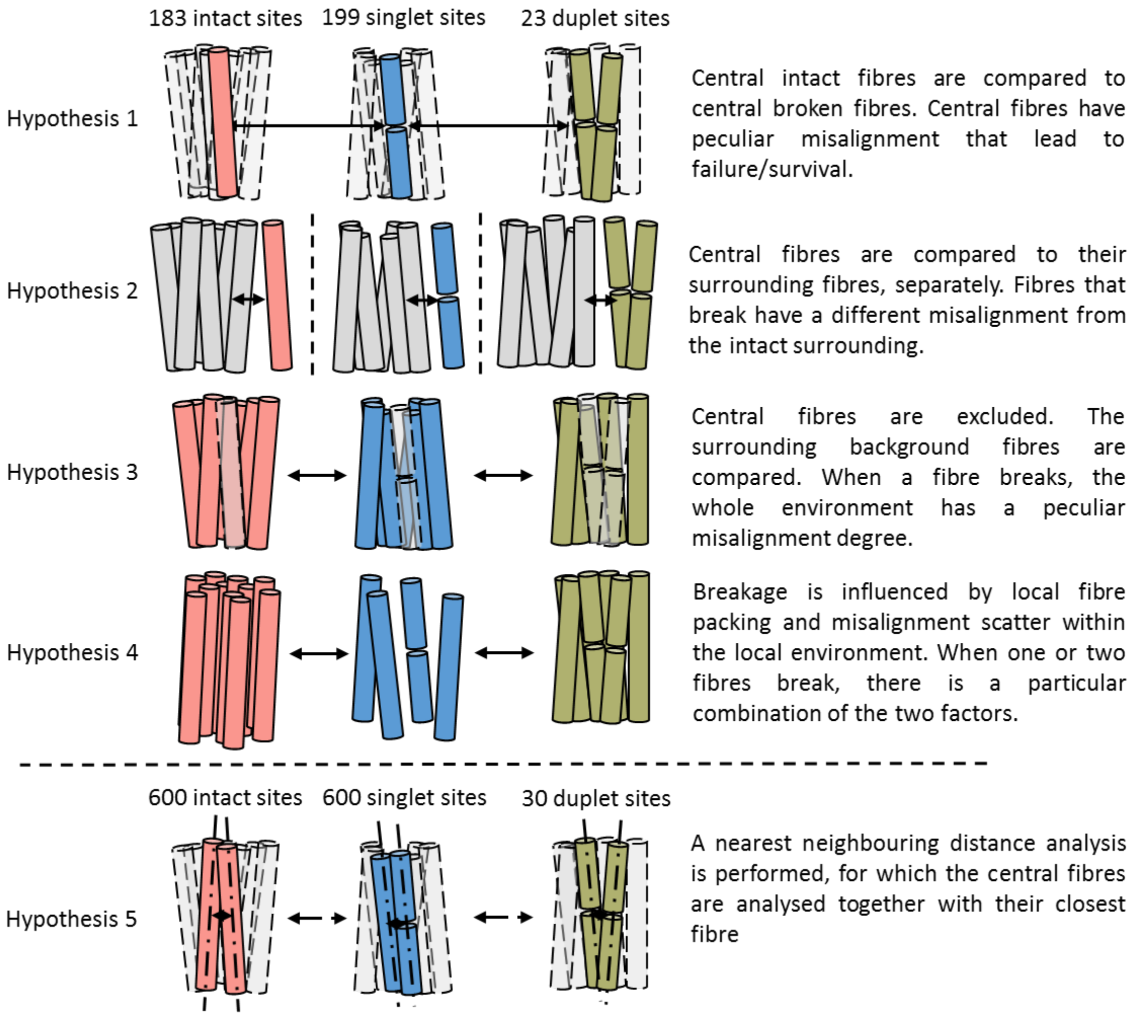

Central intact fibres are compared to central broken fibres. Central fibres have peculiar misalignment that lead to failure/survival.

Central fibres are compared to their surrounding fibres, separately. Fibres that break have a different misalignment from the intact surrounding.

Central fibres are excluded. The surrounding background fibres are compared. When a fibre breaks, the whole environment has a peculiar misalignment degree.

Breakage is influenced by local fibre packing and misalignment scatter within the local environment. When one or two fibres break, there is a particular combination of the two factors.

A nearest neighbouring distance analysis is performed, for which the central fibres are analysed together with their closest fibre

Figure 6.5. The five comparisons are illustrated. Comparison 1 to 3 looks at the fibre orientation differences between the three classes of fibres, aiming at indications in the misorientation of the central broken fibres or the surrounding environments that can imply different morphologies for locally damaged sites. Comparison 4 accounts for the local fibre packing and misorientation scatter within sub-volumes. Lastly, comparison 5 investigates the nearest neighbouring distance between the same classes of fibres.

- Hypothesis 2: The orientation of fibres that break is distinctive from their immediate environment. For example, indicating if an otherwise well aligned fibre surrounded by a region of misorientation is more likely to break. As such, the orientation characteristics of fibres that break are compared to their immediately surrounding environment.

- Hypothesis 3: The environment surrounding singlet/duplet sites is distinctive from equivalently proportioned regions where breaks have not occurred. As such, the orientation characteristics of fibres within singlet/duplet sites are compared to those within intact sites.

- Hypothesis 4: The local fibre packing and the scatter in the local fibre misorientation influence the failure process. The number of fibres within a site and the standard error of their misorientation are quantified to identify a peculiar combination of the two factors.
- Hypothesis 5: This focusses on the incidence of coupled fibre break duplets, testing if the nearest-neighbour fibre separation at duplet sites is distinctive from nearest-neighbour distances where either a single fibre break has been recorded, or the nearest-neighbour distances drawn from the general unbroken micro-structure.

With the many thousands of individual fibre measurements that are readily derived from the fibre segmentation, many other tests/hypotheses are possible – four are considered here for brevity. As stated in Section 6.2.2, it is noted that measurements presented here are based on the final load step (between 98 and 99% of coupon UTS). Even at such high relative loads, the number of high multiplet sites (n $\geq$ 3) is limited: as such, only the statistics associated with duplets has been examined here, representing at least an initial stage in progressing from single fibre break to critical cluster formation.

Table 6.1. Hypothesis 1: the mean (μ) and standard deviation (σ) of the intact and singlet fibres are shown for the in-layer direction. For both the assessed coupons, σ of the singlet fibres is higher. In the two columns on the right, the Kolmogorov-Smirnov test results are indicated: the distributions of misorientations are drawn from a same population.

Coupon	**μ misorientation (deg)**		**σ misorientation (-)**		K-S test value	p-value (-)
	Intact fibres	Singlet fibres	Intact fibres	Singlet fibres		
1	-0.13	-0.16	0.90	1.11	0	0.52
2	0.22	0.38	0.86	1.09	0	0.73

6.4.1 Hypothesis 1: broken fibres to intact fibres

The misorientation angles for the in-layer and out-of-layer directions are presented in Fig. 6.6 for broken and non-broken fibres.

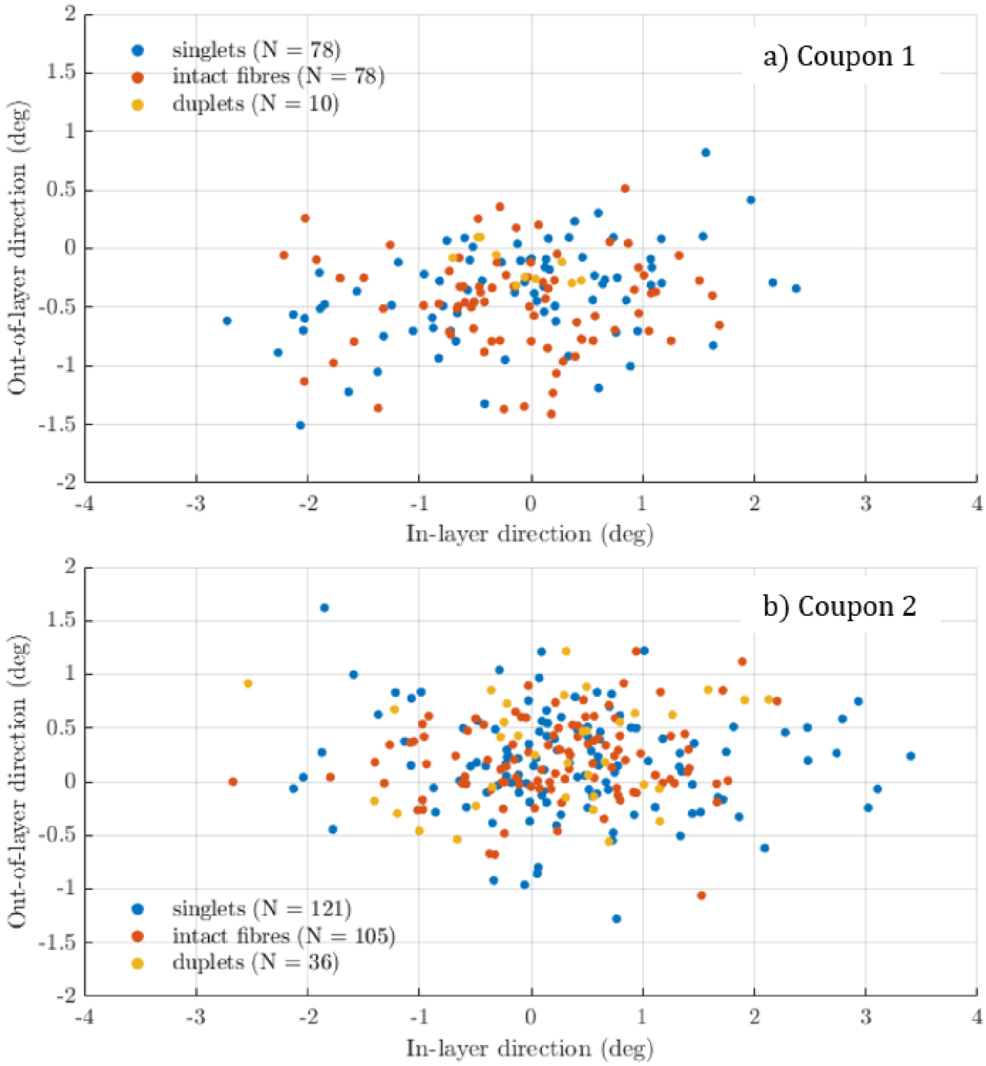

Figure 6.6. Scatter plot of the fibre orientation of the individual fibres the sub-volumes at the intact, singlet and duplet sites.

In the first instance, it may be seen that the spread of fibre misorientation is distinctly wider in the in-layer direction. The maximum range of in-layer orientations of the unbroken fibres (i.e. randomly selected micro-structure) is ∼4-5^o, while out-of-layer range is ∼2^o, the corresponding standard deviations are ∼0.4^o and ∼1.1^o. Whilst samples were cut from the same as-manufactured plate, and care was taken to cut and align samples prior to testing, there is a slight divergence of alignment between the two: Coupon 1 presents a slight out-of-layer tilt in the order of 0.5^o, whilst Coupon 2 shows an in-layer tilt from the loading direction in the order of 0.2^o.

While by looking at the mean value (μ) of the intact and singlet fibre misorientation distributions no difference is evinced, a consistent larger value is observed for the standard deviation (σ) of the singlet fibres (see Table 6.2) of both coupons. A K-S test run to better discern the differences between the two distributions of data has indicated that these are drawn from the same population. K-S test results with associated p-values are reported in Table 6.2, where 0 indicates the distributions are drawn from the same population and 1 that the populations are statistically distinct, with a threshold probability of 0.05.

Table 6.2. Summary of the resampling analysis, carried out to check whether the duplet smaller sample size affected the comparison results. K-S and A-D tests are performed before implementing the resampling approach. Each of the 1000 samples randomly extracted from the singlet and intact sites, is K-S and A-D tested and the proportion of values below the 5% p-value threshold is indicated.

	Coupon 1		**Coupon 2**	
Test performed	Duplet intact	Duplet singlet	Duplet intact	Duplet singlet
K-S before resampling	0.59	0.31	0.57	0.66
A-D before resampling	0.44	0.18	0.90	0.80
K-S p-value proportion <0.05	0.00	0.02	0.00	0.00
A-D p-value proportion <0.05	0.03	0.09	0.00	0.00

6.4.1.1 Unbalanced sample size comparison statistical tests

Given that the duplet fibres sample size is significantly smaller than the intact and singlet samples (across both coupons total duplets N = 46, as opposed to N ~200 measured for intact fibres and singlets), sub-sampling of the singlet and intact fibre datasets to ensure an equal sample size in the K-S and A-D tests. Multiple random subsamples were considered, to account for variation in results between subsamples.

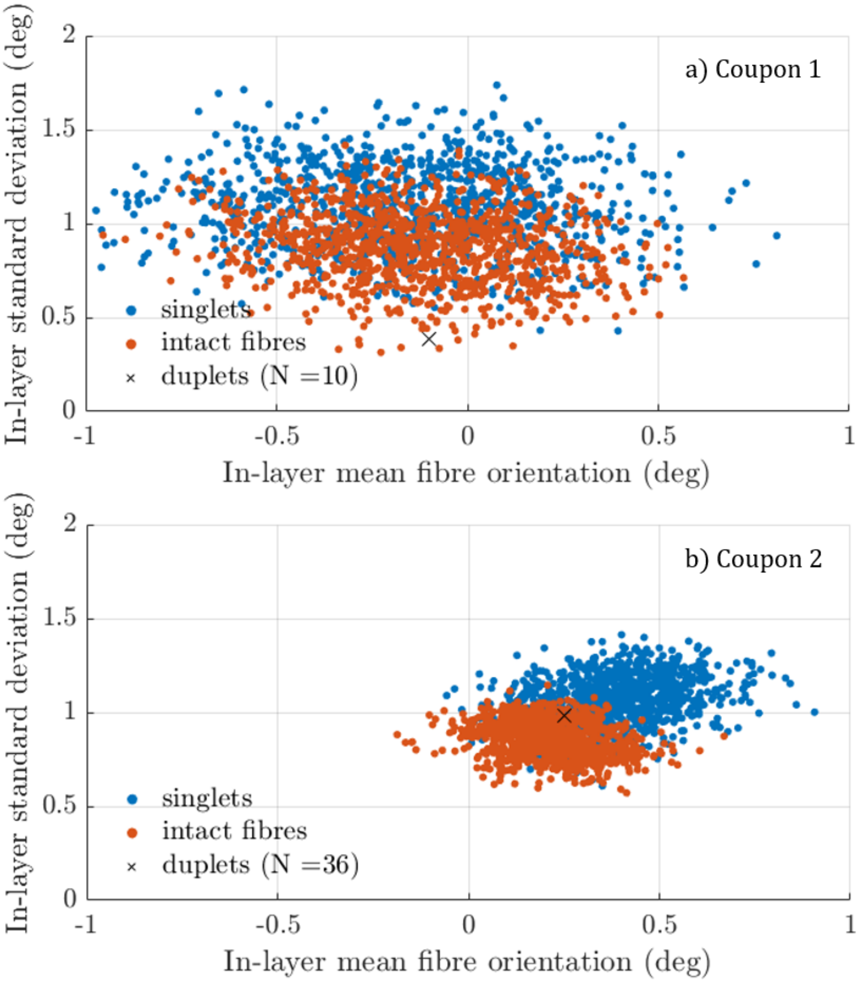

Figure 6.7. Scatter plot of the 1000 resamples to the smallest sample dimension (duplet samples of respectively 10 and 36 measurements).

Subsampling was used as statistical tests for unbalanced samples often result in bias. The same approach is implemented for all the comparisons presenting an unbalanced sample size.

The software environment for statistical computing and graphics R ([180]) is adopted to check whether the unbalanced sample sizes affect the comparison results. Both an Anderson Darling (A-D) and K-S tests are used, where A-D is more sensitive to the tails of the distributions than K-S [179]. The same statistical tests (K-S and A-D tests) are performed before and after carrying out the resampling to the smallest sample dimension, and results are compared. Resampling is performed by randomly extracting without replacement 1000 samples of data extracted from the intact and singlet sites of the dimension of the duplet sites, i.e. for Coupon 1 and 2, 1000 samples made of respectively 10 and 36 values of singlet and intact fibre misorientation angles.

Each sub-sample of data is compared to the sample of duplet fibre angles using the K-S and A-D tests. The proportion of p-values below 0.05 (indicating statistically significant difference between the distributions of the data) is reported in Table 6.2. For both coupons and comparisons (duplet to singlet fibres and duplet to intact fibres), the proportion below 0.05 is low enough to confirm that the smaller duplet sample size does not statistically affect the observed results: there is statistical evidence to suggest that the duplet fibre misorientation distribution is drawn from the same population of fibre misorientation as that of the singlet/intact fibres.

In Fig. 6.7, for Coupon 1 and 2, the mean and standard deviation values for the extracted singlet and intact sub-samples and duplet samples is shown. As can be seen, the in-layer standard deviation is slightly higher for the singlet sites than for the intact sites.

6.4.2 Hypothesis 2: broken fibres to their surrounding environment

The fibre orientation of the singlet fibres and their surrounding environment is analysed. For Coupon 1, 78 singlet fibre orientations are compared to the 2054 background surrounding fibres extracted from the same singlet sites (121 to 3400 for Coupon 2), see Fig. 6.8. Given that the two samples of data are unbalanced, a resampling approach is adopted, as done for Section 6.4.1.1. The proportion of p-values of the 1000 extracted sub-samples is observed being about 1%, providing no statistical evidence to suggest that the distributions of the fibre misorientations differ. The same comparison is performed for the duplet and the intact sites, showing no statistical evidence for a difference; and hence suggesting that the fibres broken in a duplet or singlet fashion do not have a different orientation if compared to their background environment.

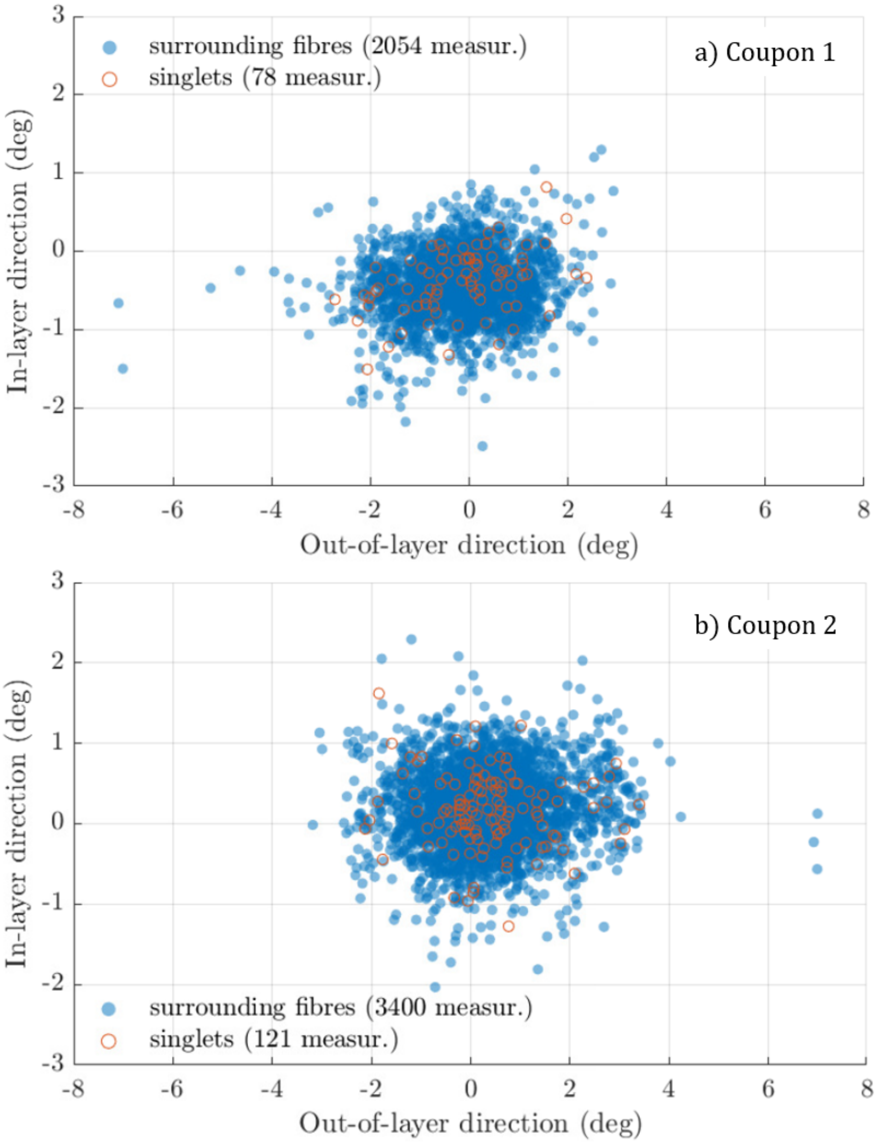

Figure 6.8. For Coupon 1 and 2, the misorientation angles in the in-layer and out-of-layer directions are plotted for the singlet fibres and the surrounding environment. The results of the K-S tests run for the distributions in the two separate directions are shown (zero meaning distributions are drawn from the same population).

6.4.3 Hypothesis 3: the background environments

The distributions of fibre orientations in the in-layer direction are compared for the singlet and intact background fibres (central fibres are excluded from the comparison). To better compare the misorientation values of the two coupons, the average fibre orientation (calculated considering all sites) of a single coupon is evaluated. This value is subtracted from each fibre misorientation value, providing the distributions are centred on the zero (representing the vertical loading direction). Coupon 2 appeared to be overall more misaligned in the in-layer direction and on the opposite direction of Coupon 1 (by a fraction of degree). This could be introduced from the manufacturing of the coupon. For this reason, the signs of the values for Coupon 2 are reversed in the histograms shown in Fig. 6.9. Having a lower number of measurements and to better visualise the different activities in the tails of the distributions, the duplet environment distributions are not included in the histogram plots. A K-S test carried out on the background fibre distributions of the singlet and intact sites provided statistical evidence to suggest that the distributions are drawn from different populations. Very similar results are obtained if comparing the duplet to the intact environment. The mean μ of the singlet and intact environments are different, as well as the standard deviation σ, which is fractionally higher in the singlet environment distribution (see Table 6.4 in Section 6.4.3.1.2).

6.4.3.1 Analyses of the tails of the background environment distributions

In the two following sections, statistical tools are implemented to better highlight dissimilarities between the distributions of data of the background environments. In Section 6.4.3.1.1, the outliers of the distributions are detected and removed to assess their influence on the statistical comparison. Following this, Kurtosis and Skewness analyses ([181]) are employed to further discern the distributions. These tests also allow a better definition of the length-scale over which patterns of fibre misorientation may or may not affect fibre break formation, as will be discussed in Section 6.4.3.1.2.

6.4.3.1.1 Outliers detection and removal through the Pukelsheim three sigma rule

An outlier detection technique is adopted to better understand if the differences observed for μ and σ in Section 6.4.3 are related to the different tails of the distributions. The aim is to assess the impact of outliers on the results of the K-S test and A-D test and the standard deviations of the samples of data. Outliers can be detected in a number of different ways. In this study, a Pukelsheim three sigma rule is used to detect the outliers [182]. This rule states that 95% of the density of unimodal distributions lies within three standard deviations of the mean, hence the outliers are treated as those which fall outside this range. Initial analysis of this dataset suggests that the distribution of misorientation data is unimodal. If removing these values makes a difference to the analysis, then the outliers should be checked to identify if they are errors or points of interest. For the in-layer directions, two comparisons are made: duplet to intact and singlet to intact environments. Table 6.3 shows the results for the first three width steps to show how values change when moving from width 2 to thicker or thinner cross-sections, i.e. including more or less fibres surrounding a broken one.

Table 6.3. K-S and A-D tests to estimate dissimilarities between the distributions of fibre misorientation before and after removal of outliers using the Pukelsheim three sigma rule. A p-value below 0.05 represents a statistically significant difference between the compared distributions.

Singlet to intact **Duplet to intact**	**Coupon 1**			**Coupon 2**		
Width	1	2	3	1	2	3
K-S p-value before outliers removal	0.01	0	0	0	0	0
	0.2	0.1	0.02	0.12	0.03	0.02
A-D p-value before outliers removal	0.01	0	0	0	0	0
	0.08	0.02	0	0.09	0.03	0.04
Number of outliers detected	4, 1	13, 7	17, 24	8, 14	16, 27	27, 36
	1, 1	2, 7	2, 24	0, 14	4, 27	4, 36
K-S p-value after outliers removal	0.01	0	0	0	0	0
	0.22	0.05	0.01	0.13	0.04	0.02
A-D p-value after outliers removal	0.01	0	0	0	0	0
	0.06	0.01	0	0.08	0.03	0.03

In Table 6.3, the number of outliers removed from the left and the right side of the distributions are indicated. The K-S and A-D tests are used to compare the distributions before and after the outlier removal. For all the analysed cases, the p-values of the K-S and A-D tests before and after outlier removal reveal no evidence of outliers effects on the results of the statistical tests. No firm conclusions can be

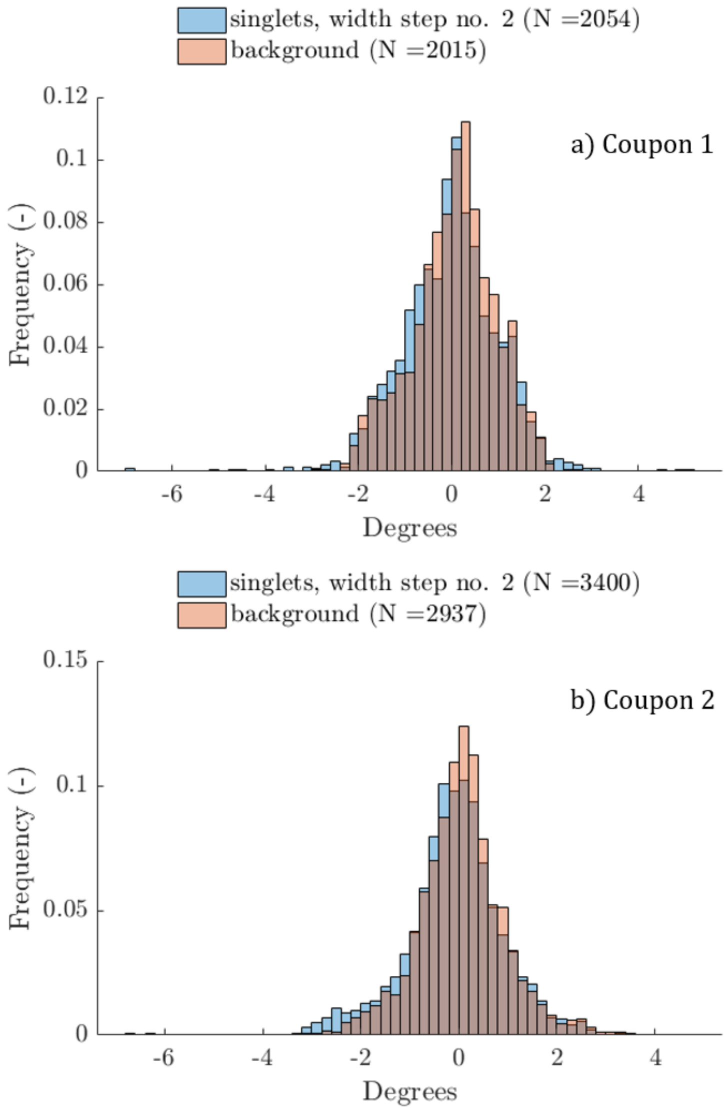

Figure 6.9. The distributions of the misorientation angles on the in-layer direction are shown. To better compare the misorientation values of the two coupons, the distributions are shifted of the average coupon fibre orientation. For Coupon 2, the sign of the orientation values is inverted to better compare the two distributions. Statistical assessments are made using the original distributions of data.

drawn from the comparison between duplet and intact sites, with width 3 being the only step at which statistical differences between the distributions are observed for both coupons. This can be related to the particularly low number of duplet sites available. As to the singlet to intact environment comparison, for both coupons it is there is statistical evidence to suggest that the two distributions are drawn from different populations, according to both K-S and A-D tests, before and after outlier removal, meaning the difference between the background environments of singlet and intact sites cannot be attributed to the extreme values of the distributions but there is evidence to suggest it is related to an intrinsic dissimilarity.

6.4.3.1.2 Kurtosis and Skewness analyses and justification of the length-scale choice

Kurtosis is a measure of how outlier-prone a distribution is. Where the kurtosis of the normal distribution is 3, distributions that are more outlier-prone than the normal distribution have kurtosis greater than 3 and distributions that are less outlier-prone have kurtosis less than 3. As shown in Fig. 11, with the exception of width 1, all the analysed widths provide distributions of fibre misorientation that are more outlier-prone than a normal distribution. Skewness is a measure of the symmetry of a distribution. The normal distribution is a symmetric distribution, and its skewness value is zero. A negative skewness value means the distribution is asymmetrical and its values are skewed to values below the mean. The opposite is valid for positive skewness values [181, 183]. Of all the analysed width steps, width 2 shows the greatest difference between the kurtosis values. This lead us to give more interest to width 2, being the area around the central fibres at which the difference between damaged and intact sites was the greatest. Results are shown for Coupon 1 which of the two coupons, is the most aligned to the loading direction. The results of the Skewness analysis indicate how the singlet background fibre distribution is slightly more skewed left on widths 2, 3 and 4. In Table 6.4, the results of the K-S tests for both coupons, surrounding environment fibres distribution in the in-layer direction are shown. With a p-value equal to 0, there is strong statistical evidence to suggest that the two distributions representing the environments in the singlet and intact sites are different.

6.4.4 Hypothesis 4: Local fibre packing and misorientation scatter within sub-volumes

When a fibre breaks, the surrounding fibres experience a stress increase. This is quantified using the stress concentration factor (SCF), which is the relative increase in stress these fibres will perceive [14]. Fibre packing affects the SCF and starting

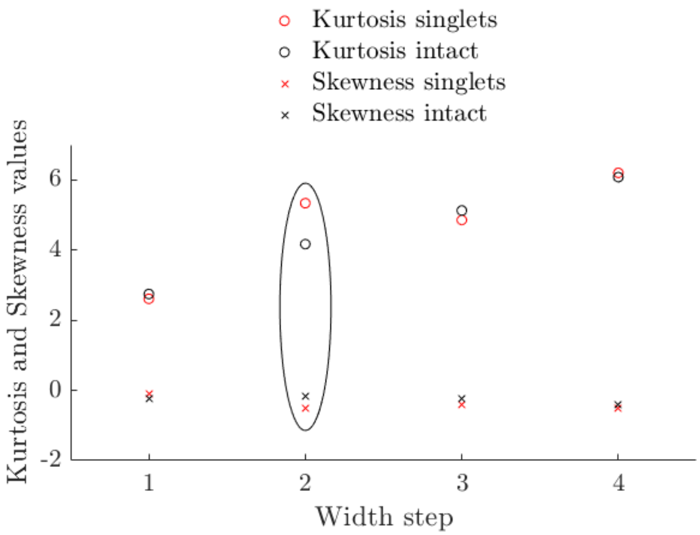

Figure 6.10. The distributions of the misorientation angles on the in-layer direction are shown. To better compare the misorientation values of the two coupons, the distributions are shifted of the average coupon fibre orientation. For Coupon 2, the sign of the orientation values is inverted to better compare the two distributions. Statistical assessments are made using the original distributions of data.

Table 6.4. Hypothesis 3: μ and σ of the intact and singlet environment fibres are shown for the in-layer direction. For both the assessed coupons, σ of the singlet fibres is higher. In the two columns on the right, the Kolmogorov-Smirnov test results are indicated: the distributions of misorientations are proven to be statistically different with a p-value equal to zero.

Coupon	**μ misorientation (deg)**		**σ misorientation (-)**		K-S test value	p-value (-)
	Intact fibres	Singlet fibres	Intact fibres	Singlet fibres		
1	-0.09	-0.18	0.92	1.01	1	0
2	0.18	0.33	0.92	1.01	1	0

from the 1960's modellers have considered different fibre arrangements moving from a regular 1D to a random 2D configuration and quantified the effect of these packing arrangements on the SCF values [84, 94, 184]. Using a finite element approach, Swolfs *et al.* showed random packing leads to higher SCF values if compared to regular arrangements [25]. This provides further significance to the examination of the local fibre packing in the analysed coupons to understand if fibre failure is affected by local volumetric fibre distribution. Only fibres fully contained within the analysed volume (of width 2 cross-section described in Section 6.3.1.2) were tracked in this study. Hence, the parameter presented below will be identified as a fibre volume fraction 'factor', obtained as a classic fibre volume fraction value but not accounting for portions of fibres falling within the edges of volume, i.e. this factor is equal to or lower than the fibre volume fraction. In Fig. 6.11, for Coupon 2 (presenting the highest number of sites) the factor is plotted against the standard error of the misorientation of the fibres comprised in a sub-volume. Each point is indicative of a full sub-volume condition. A sub-volume with a higher fraction factor is expected to have a lower misorientation standard error due to the fibres being closely packed together, where the opposite is likely to happen for a sub-volume with a low fraction factor. The mean and the standard deviation of the values for the three sub-volume categories are reported in Table 6.5, highlighting that no major differences are observed. K-S tests run separately on the two parameters comparing the distributions singlet-intact, singlet-duplet and intact-duplet suggest no statistical differences can be evinced (p-values in the range of 0.5-0.7). Similar results are obtained for Coupon 1.

Table 6.5. μ and σ of the fibre fraction factor (FFF) and misorientation standard error (MSE) shown in Fig. 6.11. No statistical differences are evinced among the three site categories.

	μ			σ		
	Intact fibres	Singlet fibres	Duplet fibres	Intact fibres	Singlet fibres	Duplet fibres
FFF (-)	0.63	0.63	0.65	0.08	0.09	0.11
MSE (-)	0.12	0.12	0.13	0.07	0.07	0.06

6.4.5 Hypothesis 5: Nearest neighbour distance analysis

A statistical assessment of the nearest-neighbour distances is carried out. Two different break clusters patterns are observed. In Fig. 13 (a, b) an example of planar

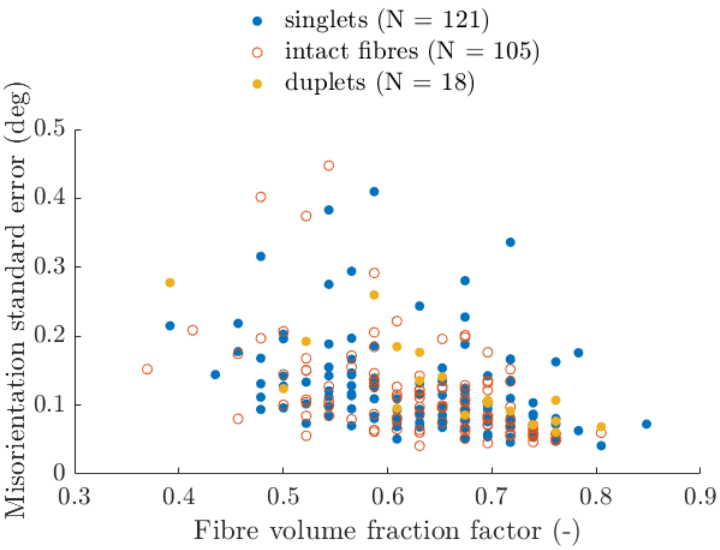

Figure 6.11. The sub-volumes fibre volume fraction factors (number of entire fibres per sub-volume cross-sectional area times the average nominal fibre cross-section) against the standard error of the misorientation of the fibres within the sub-volumes of Coupon 2 (showing the highest number of sub-volumes), width 2. K-S tests show no statistical differences between the three categories. Similar results are obtained for Coupon 1.

clusters and diffuse clusters is shown. Planar (or adjacent) clusters (focus of the study) are considered as groups of fibre breaks with a distance less than a fibre diameter. Fibre breaks with a distance less than the ineffective length are catalogued as diffuse clusters [14, 24]. In Fig. 6.12c-f, examples of planar clusters are presented. As shown, clusters arise both in locally high volume fraction regions, and mixed regions, where a linear pattern is commonly observed. Except for two cases, fibre break clusters have not been observed to grow under increased loading, as illustrated in [22, 24, 31].

With a distance of 1.65 fibre diameter, the only case of a large nearest-neighbouring distance between two planar broken fibres is shown in Fig. 6.13. This experimental finding confirms what would be intuitively indicated by a load shedding behaviour: clustering should happen mostly between close neighbours (higher load is seen by an intact fibre that is closer to a break). In Fig. 6.14, the nearest neighbouring fibre distance values collected for the two coupons is shown. For the singlet and intact locations, about 600 values have been collected, against 25 values for the duplet sites (related to the highest number of clusters observed in the prior-to-failure scans). With

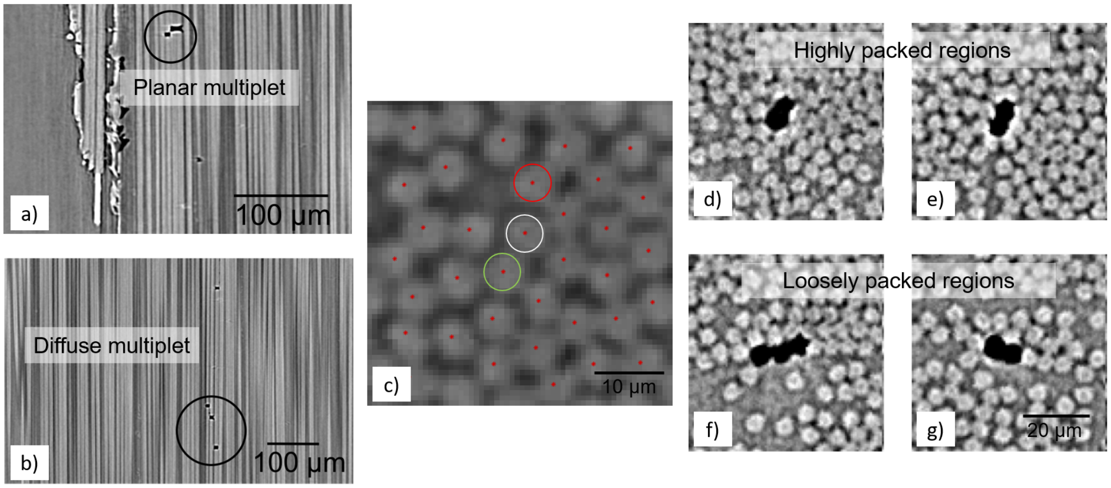

Figure 6.12. (a) Example of a planar multiplet, (b) diffuse multiplet. In (c): in the white circle the fibre breaking in a duplet fashion. Circled in green its closest fibre, preferred for duplet formation; among all the neighbours, in red the furthest (typically not involved in multiplet formation) is highlighted. In (d, e), planar duplets in a high fibre volume fraction region whereas in (f, g) triplet and duplet are shown in a 'mixed' volume fraction region.

a few cases of fibres having the nearest neighbour at a distance greater than 1.5 fibre diameter, the mean nearest neighbouring distance observed value is for all the three cases of ∼1.1 fibre diameter, meaning that even in low packed regions, the great majority of fibres tend to have at least one very close nearest neighbour. This is in contrast to 1.35 fibre diameter, the nearest neighbouring distance that is calculated assuming a 2D hexagonal packing with same fibre volume fraction (of 50% in this study) and according to that indicated by Swolfs *et al.* [14]: having random packings much closer fibres to the broken ones, these see an increase in the stress concentration factors when compared to regular packings. A K-S test is performed to compare the three groups of data, and it suggests that there are no statistical differences between the distributions shown in Fig. 6.14.

6.5 Conclusions

In situ synchrotron X-ray computed tomography was performed to investigate the morphology of local damaged sites in untoughened aerospace grade carbon-epoxy

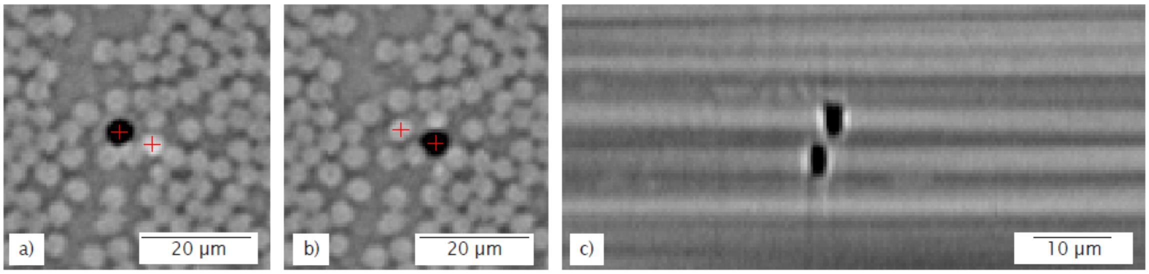

Figure 6.13. (a, b) Top view and (c) lateral view of the duplet with the largest detected distance observed in the two analysed coupons. Separation distance between the centres of the break was of ~3 μm.

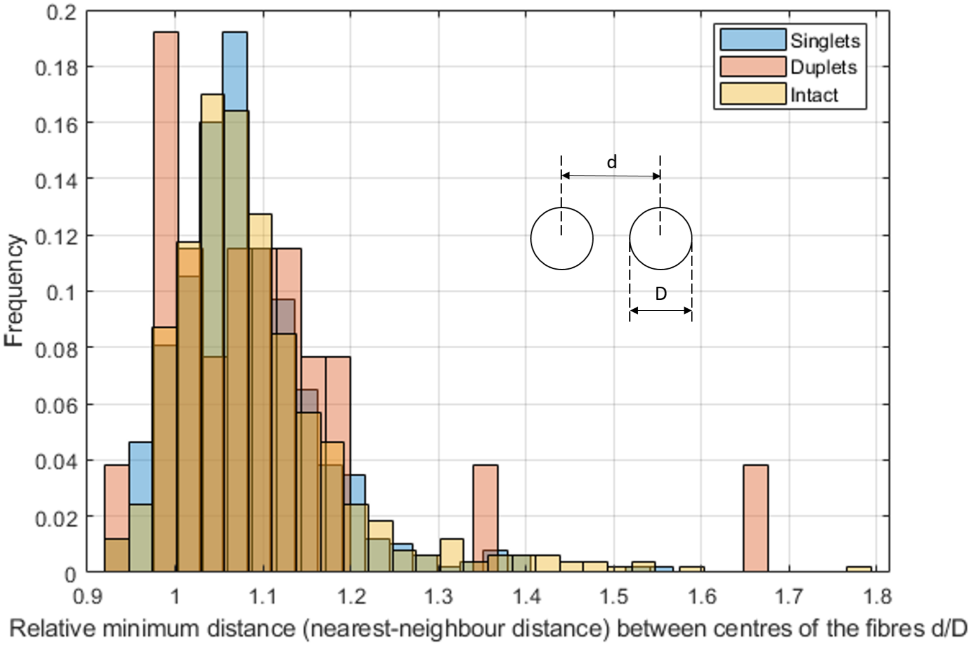

Figure 6.14. Histogram of the relative distances between two broken fibres recorded a fibre diameter below the failure plane (duplets); relative distances between a broken fibre to its nearest neighbouring intact fibre (singlets); closest distance between random intact fibres (intact locations). Values are obtained combining the data of the two analysed coupons, cut from the same CFRP panel.

coupons under quasi-static tensile loading. It is well known that carbon fibre tensile strength distributions follow a Weibull probabilistic model. However, local fibre misorientation and packing needs to be assessed to clarify their effects on the failure processes. To the best of the authors knowledge, this is the first time an automated approach was developed that uses image analysis and statistical tools to investigate at a micro-scale level single and adjacently coupled fibre break locations, assessing differences in the misorientation of the fibres and in the nearest neighbouring distances between fibres, both in damaged and non-damaged local sites. Great attention is given to the quality of the fibres segmented from low contrast images with high fibre volume fraction, with a detailed error trapping approach.

Statistically assessed experimental observations of the fibre misorientation angle distributions provide subtle indications on the existence of different morphologies among these sites. For the carbon fibre pre-preg composite coupons object of this study, there is statistical evidence to suggest that the local background environment of singlet sites and intact sites differ, providing input for further investigations. The single broken fibre orientation distribution shows a consistent higher standard deviation value, when compared to the intact fibre orientation distribution. In contrast, no statistically significant differences are observed regarding the fibre packing in locally damaged sites. The nearest neighbouring distances are evaluated for the cases of two intact fibres, one broken and one intact fibre and two adjacent broken fibres, showing that two fibres prefer to break in a nearest neighbouring fashion. These observations suggest that the morphology of fibre break sites appear as complex. By a simple visual assessment of a few sites, contrasting and incorrect conclusions could be reached, e.g. a fibre is more likely to fail if surrounded by misoriented, hence less loaded fibres or fibres break in a duplet fashion when close to each other and near a resin rich region, experiencing a higher stress than expected.

It is suggested in the literature that the singlet density is not likely to be the cause of longitudinal final failure of composites [14, 22, 24], while the large multiplets might have a stronger role instead, suggesting a failure criterion driven by the Fracture Mechanics could be preferred over the Strength of Materials [32]. However, reliable models predicting both the damage development and the final failure of unidirectional composites should include and correctly describe the mechanisms leading to the accumulation of these features, that strongly escalates prior to final failure. The fibre strength is typically described using the Weibull strength distribution. However, measuring the Weibull distributions remains challenging and studies have shown that better distributions, more challenging to implement in models but more suitable to describe the strength variability could be adopted ([45, 185]). Hence, model overestimations in the singlet prediction are often attributed to the distribution errors, as done in [24]. However, by combining:

- *in situ* SRCT, allowing the damage to be fully captured in 3D in a prior-to-failure condition,
- automated image processing techniques, that enable the comprehensive morphology of damaged and non-damaged local regions to be extracted in low computational times from CT scans, with an error trapping approach that reduces the fibre centre detection error to a negligible level,
- reliable statistical tools, such as Kolmogorov-Smirnov tests, Anderson-Darling tests, Kurtosis and Skewness tests as well as a Pukelsheim three sigma rule, used to capture subtle differences in the distributions of the data extracted from self-similar micro-structures difficult to discern by eye, recognise the variability in the sizes of the distributions of data and investigate the influence of the tails of the distributions, typically indication of errors or peculiar cases of interest,

it can now be suggested that the local morphology might have a role in the formation of fibre breaks as it is shown that statistically the background environment of singlet sites has some peculiarities that should be further explored by including the real fibre geometry as extracted from the analysed sites into finite element (FE) predictive models. The analysis presented in this chapter represents a first step towards a full characterisation of the large multiplet local morphology that can provide the modelling community more information on the influence that these features have on the final failure events. However, larger experimental campaigns are needed that test a greater amount of coupons of the same material, as in this study a total of four 4-plets have been captured in the prior-to-failure scans from the two analysed coupons, i.e. tens of coupons should be tested to obtain statistically approachable data.

The tools are now developed, with a high level of confidence in the basic measurements and other application areas can be envisaged where micro-structural influence may be important: e.g. compression/micro-buckling, and materials with non-ideal unidirectional alignment. In addition to the applications on particular materials, the work presented in this chapter illustrates an approach, consistent with the philosophy of “data rich mechanics” whereby very high levels of utilisation of experimental studies can be used to extract data by which to inform model development and validation.

(This page was intentionally left blank)

CHAPTER 7

CONCLUSIONS AND FURTHER WORK

In situ synchrotron radiation computed tomography has been used to analyse the effects of fibre/matrix properties and manufacturing parameters on the accumulation of individual fibre breaks and groups of interacting fibre breaks. Overall, the work has successfully captured the variations in the tensile behaviour when the fibre/matrix interfacial properties are modified in five aerospace grade configurations of $(90_2/0_2)_s$ *carbon-epoxy notched coupons as well as underlined in an original approach the peculiarities in the morphology of locally damaged sites. Semi-automated approaches have been developed to capture the damage behaviour at a deep micro-mechanical level for a range of materials with different fibres, surface treatments and sizing. Statistical tools have been adopted to explore single and adjacently coupled fibre break locations, measuring subtle alterations in the fibre misorientation and in the nearest neighbouring distances between fibre. Quantitative data and qualitative observations have been presented that are consistent with the philosophy of "data rich mechanics" by which to inform model development and validation.*

7.1 Summary

An extensive database of performance and damage behaviour at a deep micromechanical level has been presented in Chapters 4 to 6 for a range of materials with different fibres, surface treatments and sizing. In Chapters 4 and 5 the fibre damage progression is followed in five tested material configurations, while in Chapter 6 focus is given to the material configuration that is most consistent for repeat coupons and statistical measurements are performed in damaged sites to capture local morphology peculiarities that could influence the damage development.

In Chapter 4, the material properties, the experimental procedure adopted and the semi automated tools developed to reduce the processing time of the ∼140 volumes collected during the main test campaign performed at the European Synchrotron Radiation Facilities are presented. The fibre volume fraction and the average composite UTS for the tested geometries are calculated, showing a difference in the UTS values in the materials adopting the same fibre type that could be attributed to the different fibre/matrix interface treatments. As the discussion focuses on the planar multiplets, believed to drive the micro-mechanisms leading to final failure, the reader is introduced to the typologies of multiplets reported in the literature ([22, 24, 31]), i.e. planar and diffuse multiplets, as observed in the materials assessed in this study.

Statistical aspects of the damage should be considered when analysing very small sampling volumes in assessing the damage development. Hence, the variability in fibre break density between coupons and within different locations in an individual coupon is estimated to be within a range of ∼30%. The main comparisons are presented and individual fibre break accumulation with ply stress is shown to be relatively consistent within the tested batch, where the opposite is observed for the multiplet accumulation. Sizing type and surface treatment are not seen to induce multiplet accumulation to the same extent as changing fibre type does, as extrapolated from the comparisons between materials A and E (differing for the fibre type adopted) and materials A and C (differing for sizing type). The multiplet formation is seen to increase when moving from material A to C, i.e. from a stronger to a weaker fibre/matrix interface. Weakening the interface through a change in surface treatment (materials A to B) led to a comparable formation of small multiplets, but higher formation of large multiplets, while an even weaker interface through different sizing type (B to C) did not increase the large multiplet formation but noticeably increased the small multiplet count.

In Chapter 5 the analysis of ∼250 planar multiplet is reported. Planar multiplets have been followed from the formation to the prior to failure conditions of the coupons, and for one coupon in post-mortem conditions. Of the multiplet geometries analysed in this study, only 2-plets and 3-plets have been observed in sufficient numbers to merit detailed quantitative analysis, with a 6-plet being the largest multiplet detected in any of the materials tested prior to failure. The highest planar multiplet formation is observed in the material (configuration E) with the strongest fibre/matrix interface and the highest Weibull modulus fibre, consistent with the higher stress concentration factors (SCFs) in the multiplet plane as well as the potential of higher amount of fibres failing at the same given stress.

For the remaining configurations (A to D) sharing the same fibre type, it is observed that a change in surface treatment is more critical than a change in sizing type, as defect resistance of the material is enhanced, with the coupon able to withstand a higher density of planar multiplets before failure. A post-mortem fibre break count performed below the crack surface, has revealed potential agreement to that predicted using a power law curve fitted to the fibre fracture accumulation from low to high applied stress levels, although a slightly higher value for the post-mortem multiplet count is observed that needs clarification, on whether it is related to the small post-mortem volume analysed (∼0.1 mm^3 vs. 0.54 mm^3 of the before failure scans), hence due to a locally higher break density region, or on the energy release involved in the macroscopic failure that could cause additional damage in composite micro-structure. Considerations are made on the possible mechanisms leading to stabilised multiplets that after formation are not growing in size with the applied stress, with a hypothesised interaction of the dynamic loading leading to a multiplet of a certain size, that potentially would stop in growing in size for increased applied stresses for time dependent matrix processes that would further shield the adjacent fibres from stress concentration.

In Chapter 6, the morphology of local damaged sites was investigated in great detail. An automated approach adopting image processing techniques and reliable statistical tools (such as Kolmogorov-Smirnov tests, Anderson-Darling tests, Kurtosis and Skewness tests and a Pukelsheim three sigma rule), was developed to investigate at a micro-scale level single and adjacently coupled fibre break locations and clarify the local fibre misorientation and packing effects on the tensile failure processes. Subtle indications on the existence of different morphologies among damaged and non-damaged local sites were obtained, suggesting that local background environment of singlet sites and intact sites statistical differ, providing input for further investigations. Furthermore, while no statistically significant dissimilarities are detected on the fibre packing in locally damaged sites, a consistently higher standard deviation value is observed for the single broken fibre orientation distribution when compared to the intact fibre orientation distribution. A method of investigation is developed, with a high level of confidence in the basic measurements and other areas of application can be considered in which micro-structure characterisation has a role, such as compression/micro-buckling, and materials with non-ideal unidirectional alignment.

7.2 Conclusions

The main observations that can be extracted from the work are reported below.

- A higher fibre strength does not necessarily translate into a stronger composite. A high level of understanding is needed to capture the interaction between constituents and the failure mechanisms when developing materials. A stronger composite can potentially be obtained by accurate selection of treatments than can enhance the fibre/matrix interface properties, leading to higher defect resistance, such as a higher scale/frequency of multiplet sites that can be accommodated before failure.

- Single fibre breaks play no simple role in controlling the average UTS of the material. For the material configurations tested in the study, the rate of singlet fibre break accumulation with ply stress appeared as relatively consistent (within the experimental scatter, and independent of the multiplet behaviour).

- The incidence (onset and rate) of multiplet damage accumulation with applied ply stress varies significantly with modifications on the surface treatments and sizing types adopted for the fibres, consistently with different mechanisms happening by which the SCFs around the broken fibres change.

- The same sizing type and surface treatment can affect differently the defect tolerance. Sizing type 1 and surface treatment II is seen to lead to material A (lower diameter, higher strength fibres and) exhibiting the lowest UTS value of the materials sharing the same fibre type, with a relatively low number of multiplets observed, whilst in material E (larger diameter, lower strength fibres), the same sizing and surface treatment induced the formation of a higher number of multiplets, potentially detrimental to the strength.

- Within the configurations tested, a change in fibre surface treatment appears as more critical than a change in sizing type, with the planar multiplets being less extended and larger multiplets being accepted without necessarily leading to macroscopic failure.

- A statistical assessment of the local morphologies of composites extracted from CT scans is a valuable approach that can lead to new insights not accounted before and is suggested for future investigations studying micro-structural features in composites to avoid incorrect conclusions due to simple visual assessment of a few micro-scopic sites. For the aerospace grade materials tested in this study, it emerged that the local background environment of singlet sites and intact sites statistically differ providing input for further investigations.

- The nearest neighbouring distances are evaluated for the cases of two intact fibres, one broken and one intact fibre and two adjacent broken fibres, showing that two fibres are more likely to break in a nearest neighbouring fashion, consistent with a load shedding behaviour: clustering should happen mostly between close neighbours. Also, the mean nearest neighbouring distance observed value for the three cases is of $\sim$1.1 fibre diameter, meaning that even in low packed regions, the great majority of fibres tend to have at least one very close nearest neighbour.

7.3 Further work

The current research has highlighted areas for further investigation, predominantly in the experimental and image processing methods.

7.3.1 Experimental method

- Size effects are well recognised in the literature [186–188]. The work of Scott *et al.* [34] showed that notched coupons exhibited similar damage mechanisms to pressure vessels coupons. However, more work is needed to understand what the influence of size effects are on the fibre break and multiplet formations, as these are not retrieved in the literature. Scaling the coupons to 2x, 4x, 8x the cross sectional area (or equivalently the number of 0^o plies, leading to thicknesses in the notched region in the order of 2, 4 and 8 mm, while keeping the 1 mm width) would give more insight to this phenomenon. As found by Borstnar *et al.* ([189]), it would be assumed that coupons of larger dimensions and higher thickness to width ratios (a 20 mm x 3 mm cross section is mentioned in the study) could cause photon starvation at certain rotation positions while SRCT scanning. However, this was found to be incorrect and hence larger coupon geometries (that those analysed in this study) can be scanned using high resolution SRCT, while keeping a spatial resolution not far from that achieved here.

- The number of high multiplet sites ($n \geq 3$) observed in this study was limited: as such, only the statistics associated with duplets has been examined. A larger number of coupons should be tested to better quantify the variations in the morphology of large multiplet sites. Hence, the following areas of improvement in the testing procedures are suggested that could help testing a larger number of coupons:

  - in the current study, a few coupons have failed prematurely, due to coupon-level variability and inaccuracies in the smallest load bearing cross-sectional area evaluation. A voxel size of 75 µm (leading to errors in the area estimation in the range of 30%), was adopted to accommodate a large number of coupons; ∼60 coupons were imaged in one scan. A more precise cross-

  section evaluation of the coupons prior SRCT testing with higher resolution CT scans could help reducing the difference between the expected failure load and real value and lead to higher chances of capturing a comparable number of scans per coupons;
  - without collecting intermediate load step scans, coupons could be loaded to ∼95-97% expected coupon UTS and scanned (with ∼90% or less of load applied to keep cracks open). At these stress levels, large planar multiplets observed in this study have already formed in a sufficient amount. This would allow testing time reductions while increasing the number of tested coupons, considered the limited scanning time availability at the synchrotron facilities;

- The importance of the matrix relaxation and its effects on tensile tests of composites is discussed in the literature [14, 29, 31]. Providing experimental evidence of the effects that models (such as the one of [29]) predict, could be potentially obtained by performing *in situ* SRCT with both continuous and interrupted scanning. If this was not possible (compact loading rigs specifically optimised for the fast rotation speeds typical of the continuous scanning are needed that might not always be available), the tests suggested above could be performed to at least in part clarify the effects of matrix relaxation: a number of coupons could be scanned collecting multiple scans at several load steps as done in the current study, while a similar number of scans could be obtained loading to very high percentages of the expected coupon UTS and scanning, holding ∼90% of the load.

- Analysing the post-mortem conditions of the tested coupons could provide novel findings. Further investigations (following the approach taken in Chapter 5) are suggested to clarify the effects of the energy release involved in the macroscopic failure processes that can potentially introduce additional damage in the composite micro-structure.

7.3.2 Image processing

Automated image processing techniques that have allowed comprehensive morphology information to be extracted in low computational times from CT scans could be further implemented to allow more data to be extracted from the scans. The full length of the fibres could be extracted and by associating the fibre breaks to the actual full fibre shapes, precise estimates of the ineffective lengths could be extracted and statistically assessed. Furthermore, extracting larger fibre lengths would allow the fibre waviness in damaged and un-damaged local regions to be statistically assessed. If statistical evidence of fibre waviness is obtained from the comparisons (adopting an approach similar to that used in this study), the effects of the fibre waviness on the tensile failure of composites could be assessed, by extracting the fibre shapes in damaged and un-damaged volumes and use these volumes as representative volume elements (RVEs) to be studied through finite element (FE) simulations.

BIBLIOGRAPHY

[1] The Paris Agreement, [Last accessed: June 2019].
https://unfccc.int/process-and-meetings/the-paris-agreement/the-paris-agreement

[2] EU 2020 Climate and Energy Package, [Last accessed: June 2019].
https://ec.europa.eu/clima/policies/strategies/2020

[3] The 2030 climate and energy framework, [Last accessed: June 2019].
https://www.consilium.europa.eu/en/policies/climate-change/2030-climate-and-energy-framework/

[4] The research requirements of the transport sectors to facilitate an increased usage of composite materials. Part I : The composite material research requirements of the aerospace industry, GMbH, EADS Deutschland [Last accessed: June 2019].
https://trimis.ec.europa.eu/project/future-use-composites-transport/

[5] Composite UK, [Last accessed: June 2019].
https://compositesuk.co.uk/composite-materials/applications

[6] A. Gupta, A. Kumar, Composites Materials: Addressing the Climate Change, Asia Pacific Business Review 6 (1) (2013) 78–89. doi:10.1177/097324701000600107.

[7] V. Giurgiutiu, Chapter 5 - Damage and Failure of Aerospace Composites, in: V. Giurgiutiu (Ed.), Structural Health Monitoring of Aerospace Composites, Academic Press, Oxford, 2016, pp. 125–175. `doi:10.1016/B978-0-12-409605-9.00005-2`.

[8] Magma Global, [Last accessed: June 2019].
`https://www.magmaglobal.com/about/`

[9] J. Jortner, 6.03 - Applications of Carbon/Carbon Composites, in: A. Kelly, C. Zweben (Eds.), Comprehensive Composite Materials, Pergamon, Oxford, 2000, pp. 29–45. `doi:10.1016/B0-08-042993-9/00192-3`.

[10] M. Martins, R. Gomes, L. Pina, C. Pereira, O. Reichmann, D. Teti, N. Correia, N. Rocha, Highly Conductive Carbon Fiber-Reinforced Polymer Composite Electronic Box: Out-of-Autoclave Manufacturing for Space Applications, Fibers 6 (4) (2018) 92. `doi:10.3390/fib6040092`.

[11] Luxfer cylinders, [Last accessed: June 2019].
`https://www.luxfercylinders.com/`

[12] A. S. Kaddour, M. J. Hinton, P. A. Smith, S. Li, The background to the third world-wide failure exercise, Journal of Composite Materials 47 (20-21) (2013) 2417–2426. `doi:10.1177/0021998313499475`.

[13] A. S. Kaddour, M. J. Hinton, P. A. Smith, S. Li, The background to the third world-wide failure exercise, Journal of Composite Materials 47 (20-21) (2013) 2417–2426. `doi:10.1177/0021998313499475`.

[14] Y. Swolfs, I. Verpoest, L. Gorbatikh, A review of input data and modelling assumptions in longitudinal strength models for unidirectional fibre-reinforced composites, Composite Structures 150 (2016) 153–172. `doi:10.1016/j.compstruct.2016.05.002`.

[15] B. Budiansky, N. A. Fleck, Compressive failure of fibre composites, Journal of the Mechanics and Physics of Solids 41 (1) (1993) 183–211. `doi:10.1016/0022-5096(93)90068-Q`.

[16] A. M. Waas, C. R. Schultheisz, Compressive failure of composites, Part II: Experimental studies, Progress in Aerospace Sciences 32 (1) (1996) 43–78. `doi:10.1016/0376-0421(94)00003-4`.

[17] M. R. Wisnom, J. W. Atkinson, Fibre Waviness Generation and Measurement and Its Effect on Compressive Strength, Journal of Reinforced Plastics and Composites 19 (2) (2000) 96–110. `doi:10.1177/073168440001900201`.

[18] K. Niu, R. Talreja, Modeling of compressive failure in fiber reinforced composites, International Journal of Solids and Structures 37 (17) (2000) 2405–2428. `doi:10.1016/S0020-7683(99)00010-4`.

[19] S. T. Pinho, P. Robinson, L. Iannucci, Fracture toughness of the tensile and compressive fibre failure modes in laminated composites, Composites Science and Technology 66 (13) (2006) 2069–2079. `doi:10.1016/j.compscitech.2005.12.023`.

[20] S. Pimenta, R. Gutkin, S. T. Pinho, P. Robinson, A micromechanical model for kink-band formation: Part I - Experimental study and numerical modelling, Composites Science and Technology 69 (7-8) (2009) 948–955. `doi:10.1016/j.compscitech.2009.02.010`.

[21] M. J. Emerson, Y. Wang, P. J. Withers, K. Conradsen, A. B. Dahl, V. A. Dahl, Quantifying fibre reorientation during axial compression of a composite through time-lapse X-ray imaging and individual fibre tracking, Composites Science and Technology 168 (April) (2018) 47–54. `doi:10.1016/j.compscitech.2018.08.028`.

[22] A. Scott, M. Mavrogordato, P. Wright, I. Sinclair, S. Spearing, In situ fibre fracture measurement in carbon–epoxy laminates using high resolution computed tomography, Composites Science and Technology 71 (12) (2011) 1471–1477. `doi:10.1016/j.compscitech.2011.06.004`.

[23] H. Morton, 3D imaging of the tensile failure mechanisms of carbon fibre composites, Ph.D. thesis, University of Southampton (2014) [Last accessed: June

2019].
https://eprints.soton.ac.uk/366506/

[24] Y. Swolfs, H. Morton, A. Scott, L. Gorbatikh, P. Reed, I. Sinclair, S. Spearing, I. Verpoest, Synchrotron radiation computed tomography for experimental validation of a tensile strength model for unidirectional fibre-reinforced composites, Composites Part A: Applied Science and Manufacturing 77 (2015) 106–113. `doi:10.1016/j.compositesa.2015.06.018`.

[25] Y. Swolfs, L. Gorbatikh, V. Romanov, S. Orlova, S. V. Lomov, I. Verpoest, Stress concentrations in an impregnated fibre bundle with random fibre packing, Composites Science and Technology 74 (2013) 113–120. `doi:10.1016/j.compscitech.2012.10.013`.

[26] Y. Swolfs, R. M. McMeeking, I. Verpoest, L. Gorbatikh, Matrix cracks around fibre breaks and their effect on stress redistribution and failure development in unidirectional composites, Composites Science and Technology 108 (2015) 16–22. `doi:10.1016/j.compscitech.2015.01.002`.

[27] A. Thionnet, H. Y. Chou, A. Bunsell, Fibre break processes in unidirectional composites, Composites Part A: Applied Science and Manufacturing 65 (2014) 148–160. `doi:10.1016/j.compositesa.2014.06.009`.

[28] A. Thionnet, H. Y. Chou, A. Bunsell, Fibre Break Failure Processes in Unidirectional Composites. Part 1: Failure and Critical Damage State Induced by Increasing Tensile Loading, Applied Composite Materials 22 (2) (2014) 141–155. `doi:10.1007/s10443-014-9398-z`.

[29] A. Thionnet, H. Y. Chou, A. Bunsell, Fibre Break Failure Processes in Unidirectional Composites. Part 2: Failure and Critical Damage State Induced by Sustained Tensile Loading, Applied Composite Materials 22 (2) (2014) 141–155. `doi:10.1007/s10443-014-9398-z`.

[30] A. Thionnet, H. Y. Chou, A. Bunsell, Fibre Break Failure Processes in Unidirectional Composites. Part 3: Unidirectional Plies Included in Lami-

nates, Applied Composite Materials 22 (2) (2014) 157–169. `doi:10.1007/s10443-014-9399-y`.

[31] S. C. Garcea, I. Sinclair, S. M. Spearing, P. J. Withers, Mapping fibre failure in situ in carbon fi bre reinforced polymers by fast synchrotron X-ray computed tomography, Composites Science and Technology 149 (2017) 81–89. `doi:10.1016/j.compscitech.2017.06.006`.

[32] A. Bunsell, L. Gorbatikh, H. Morton, S. Pimenta, I. Sinclair, M. Spearing, Y. Swolfs, A. Thionnet, Benchmarking of strength models for unidirectional composites under longitudinal tension, Composites Part A: Applied Science and Manufacturing 111 (March) (2018) 138–150. `doi:10.1016/j.compositesa.2018.03.016`.

[33] R. M. Jones, Mechanics of composite materials, 2nd Edition, Taylor & Francis Ltd, London, 1999.

[34] A. Scott, Analysis of a hybrid composite pressure vessel using multi-scale computed tomography techniques, Ph.D. thesis, University of Southampton (2011) [Last accessed: June 2019].
`https://eprints.soton.ac.uk/196517/`

[35] L. Mishnaevsky, P. Brondsted, Three-dimensional numerical modelling of damage initiation in unidirectional fiber-reinforced composites with ductile matrix, Materials Science and Engineering A 498 (1-2) (2008) 81–86. `doi:10.1016/j.msea.2007.09.105`.

[36] A. A. Griffith, G. I. Taylor, VI. The phenomena of rupture and flow in solids, Philosophical Transactions of the Royal Society of London. Series A, Containing Papers of a Mathematical or Physical Character 221 (582-593) (1921) 163–198. `doi:10.1098/rsta.1921.0006`.

[37] B. Rosen, N. Dow, Z. Hashin, Mechanical Properties of Fibrous Composites, General Electric Co Philadelphia PA, Tech. rep. (1964).

[38] K. L. Pickering, T. L. Murray, Weak link scaling analysis of high-strength carbon fibre, Composites Part A: Applied Science and Manufacturing 30 (8) (1999) 1017–1021. `doi:10.1016/S1359-835X(99)00003-2`.

[39] S. Camara, A. R. Bunsell, A. Thionnet, D. H. Allen, Determination of lifetime probabilities of carbon fibre composite plates and pressure vessels for hydrogen storage, International Journal of Hydrogen Energy 36 (10) (2011) 6031–6038. `doi:10.1016/j.ijhydene.2010.12.069`.

[40] S. L. Phoenix, I. J. Beyerlein, Statistical Strength Theory for Fibrous Composite Materials, no. May, 2000. `doi:10.1016/B0-08-042993-9/00056-5`.

[41] W. Weibull, A statistical theory of the strength of materials, Vol. 151, IVB-Handl., 1939.

[42] W. Weibull, A statistical distribution function of wide applicability, Journal of applied mechanics 18 (1951) 293–297.

[43] T. Okabe, N. Takeda, Size effect on tensile strength of unidirectional CFRP composites experiment and simulation, Composites Science and Technology 62 (15) (2002) 2053–2064. `doi:10.1016/S0266-3538(02)00146-X`.

[44] M. H. Berger, D. Jeulin, Statistical analysis of the failure stresses of ceramic fibres: Dependence of the Weibull parameters on the gauge length, diameter variation and fluctuation of defect density, Journal of Materials Science 38 (13) (2003) 2913–2923. `doi:10.1023/A:1024405123420`.

[45] W. A. Curtin, Tensile Strength of Fiber-Reinforced Composites: III. Beyond the Traditional Weibull Model for Fiber Strengths, Journal of Composite Materials 34 (15) (2000) 1301–1332. `doi:10.1106/0gu5-lmta-9r99-2w8k`.

[46] J. W. Hitchon, D. C. Phillips, The dependence of the strength of carbon fibres on length, Fibre Science and Technology 12 (3) (1979) 217–233. `doi:10.1016/0015-0568(79)90032-0`.

[47] E. G. Stoner, D. D. Edie, S. D. Durham, An end-effect model for the single-filament tensile test, Journal of Materials Science 29 (24) (1994) 6561–6574. `doi:10.1007/BF00354022`.

[48] I. J. Beyerlein, S. L. Phoenix, Statistics for the strength and size effects of microcomposites with four carbon fibers in epoxy resin, Composites Science and Technology 56 (1) (1996) 75–92. `doi:10.1016/0266-3538(95)00131-X`.

[49] S. L. Phoenix, R. G. Sexsmith, Clamp Effects in Fiber Testing, Journal of Composite Materials 6 (3) (1972) 322–337. `doi:10.1177/002199837200600311`.

[50] J. Watanabe, F. Tanaka, H. Okuda, T. Okabe, Tensile strength distribution of carbon fibers at short gauge lengths, Advanced Composite Materials 23 (5-6) (2014) 535–550. `doi:10.1080/09243046.2014.915120`.

[51] J. L. Thomason, On the application of Weibull analysis to experimentally determined single fibre strength distributions, Composites Science and Technology 77 (2013) 74–80. `doi:10.1016/j.compscitech.2013.01.009`.

[52] Y. Swolfs, I. Verpoest, L. Gorbatikh, Issues in strength models for unidirectional fibre-reinforced composites related to Weibull distributions, fibre packings and boundary effects, Composites Science and Technology 114 (2015) 42–49. `doi:10.1016/j.compscitech.2015.04.002`.

[53] T. A. Parthasarathy, Extraction of Weibull Parameters of Fiber Strength from Means and Standard Deviations of Failure Loads and Fiber Diameters, Journal of the American Ceramic Society 84 (3) (2001) 588–592. `doi:10.1111/j.1151-2916.2001.tb00703.x`.

[54] A. S. Watson, R. L. Smith, An examination of statistical theories for fibrous materials in the light of experimental data, Journal of Materials Science 20 (9) (1985) 3260–3270. `doi:10.1007/BF00545193`.

[55] M. Ibnabdeljalil, S. L. Phoenix, Scalings in the statistical failure of brittle matrix composites with discontinuous fibers-I. Analysis and Monte Carlo simulations, Acta Metallurgica Et Materialia 43 (8) (1995) 2975–2983. `doi:10.1016/0956-7151(95)00017-P`.

[56] K. K. Phani, Strength distribution and gauge length extrapolations in glass fibre, Journal of Materials Science 23 (4) (1988) 1189–1194. `doi:10.1007/BF01154577`.

[57] P. T. Curtis, A computer model of the tensile failure process in unidirectional fibre composites, Composites Science and Technology 27 (1) (1986) 63–86. `doi:10.1016/0266-3538(86)90063-1`.

[58] S. Mahesh, S. L. Phoenix, I. J. Beyerlein, Strength distributions and size effects for 2D and 3D composites with Weibull fibers in an elastic matrix, International Journal of Fracture 115 (1) (2002) 41–85. `doi:10.1023/A:1015729607223`.

[59] M. Y. Matveev, A. C. Long, I. A. Jones, Modelling of textile composites with fibre strength variability, Composites Science and Technology 105. `doi:10.1016/j.compscitech.2014.09.012`.

[60] H. Y. Chou, A. Thionnet, A. Mouritz, A. R. Bunsell, Stochastic factors controlling the failure of carbon/epoxy composites, Journal of Materials Science 51 (1) (2016) 311–333. `doi:10.1007/s10853-015-9390-5`.

[61] H. Okuda, R. J. Young, F. Tanaka, J. Watanabe, T. Okabe, Tensile failure phenomena in carbon fibres, Carbon 107 (2016) 474–481. `doi:10.1016/j.carbon.2016.06.037`.

[62] W. J. Cantwell, J. Morton, The impact resistance of composite materials — a review, Composites 22 (5) (1991) 347–362. `doi:10.1016/0010-4361(91)90549-V`.

[63] I. J. Beyerlein, S. L. Phoenix, Stress concentrations around multiple fiber breaks in an elastic matrix with local yielding or debonding using quadratic influence superposition, Journal of the Mechanics and Physics of Solids 44 (12) (1996) 1997–2036. `doi:10.1016/S0022-5096(96)00068-3`.

[64] A. Paipetis, C. Galiotis, Effect of fibre sizing on the stress transfer efficiency in carbon/epoxy model composites, Composites Part A: Applied Science and Manufacturing 27 (9) (1996) 755–767. `doi:10.1016/1359-835X(96)00054-1`.

[65] M. Guigon, Interface and interphase in carbon-epoxy composite materials. Study by transmission electron microscopy, Microsc. Microanal. Microstruct. 2 (1) (1991) 15–25. `doi:10.1051/mmm:019910020101500`.

[66] C. Ageorges, K. Friedrich, L. Ye, Experiments to relate carbon-fibre surface treatments to composite mechanical properties, Composites Science and Technology 59 (14) (1999) 2101–2113. `doi:10.1016/S0266-3538(99)00067-6`.

[67] C. I. Wang, Fracture mechanics of single-fibre pull-out test, Journal of Mate Rials Science 32 (2) (1997) 483–490. `doi:10.1023/A:1018534323464`.

[68] D. Tripathi, F. Jones, Review Single fibre fragmentation test for assessing adhesion in fibre reinforced composites, Journal of Materials Science 33 (1998) 1–16. `doi:10.1023/A:1004351606897`.

[69] R. M. Jones, Mechanics of composite materials, no. 2, 1999. `doi:10.1007/BF00611782`.

[70] F. M. Zhao, N. Takeda, Effect of interfacial adhesion and statistical fiber strength on tensile strength of unidirectional glass fiber/epoxy composites. Part II: Comparison with prediction, Composites Part A: Applied Science and Manufacturing 31 (11) (2000) 1215–1224. `doi:10.1016/S1359-835X(00)00086-5`.

[71] G. C. Shih, L. J. Ebert, Theoretical Modelling of the Effect of the Interfacial Shear Strength on the Longitudinal Tensile Strength of Unidirectional Composites, Journal of Composite Materials 21 (3) (1987) 207–224. `doi:10.1177/002199838702100302`.

[72] M. S. Madhukar, L. T. Drzal, Fiber-Matrix Adhesion and Its Effect on Composite Mechanical Properties: II. Longitudinal (0°) and Transverse (90°) Tensile and Flexure Behavior of Graphite/Epoxy Composites, Journal of Composite Materials 25 (8) (1991) 958–991. `doi:10.1177/002199839102500802`.

[73] P. W. van den Heuvel, S. Goutianos, R. J. Young, T. Peijs, Failure phenomena in fibre-reinforced composites. Part 6: A finite element study of stress concentrations in unidirectional carbon fibre-reinforced epoxy composites, Composites

Science and Technology 64 (5) (2004) 645–656. `doi:10.1016/j.compscitech.2003.06.003`.

[74] N. Lachman, B. J. Carey, D. P. Hashim, P. M. Ajayan, H. D. Wagner, Application of continuously-monitored single fiber fragmentation tests to carbon nanotube/carbon microfiber hybrid composites, Composites Science and Technology 72 (14) (2012) 1711–1717. `doi:10.1016/j.compscitech.2012.06.004`.

[75] L. Mishnaevsky, P. Brøndsted, Micromechanical modeling of damage and fracture of unidirectional fiber reinforced composites: A review, Computational Materials Science 44 (4) (2009) 1351–1359. `doi:10.1016/j.commatsci.2008.09.004`.

[76] C. Zweben, B. W. Rosen, A statistical theory of material strength with application to composite materials, Journal of the Mechanics and Physics of Solids 18 (3) (1970) 189–206. `doi:10.1016/0022-5096(70)90023-2`.

[77] C. Zweben, Tensile strength of hybrid composites, Journal of Materials Science 12 (7) (1977) 1325–1337. `doi:10.1007/BF00540846`.

[78] M. R. Nedele, M. R. Wisnom, Three-dimensional finite element analysis of the stress concentration at a single fibre break, Composites Science and Technology 51 (4) (1994) 517–524. `doi:10.1016/0266-3538(94)90084-1`.

[79] S. Behzadi, P. T. Curtis, F. R. Jones, Improving the prediction of tensile failure in unidirectional fibre composites by introducing matrix shear yielding, Composites Science and Technology 69 (14) (2009) 2421–2427. `doi:10.1016/j.compscitech.2009.06.010`.

[80] M. R. Wisnom, D. Green, Tensile failure due to interaction between fibre breaks, Composites 26 (7) (1995) 499–508. `doi:10.1016/0010-4361(95)96807-I`.

[81] H. D. Wagner, A. Eitan, Interpretation of the fragmentation phenomenon in single-filament composite experiments, Applied Physics Letters 56 (20) (1990) 1965–1967. `doi:10.1063/1.103012`.

[82] H. E. Daniels, The statistical theory of the strength of bundles of threads, Proc. R. Soc. A 183 (1945) 405–435.

[83] J. M. Hedgepeth, Stress Concentrations In Filamentary Structures, NASA Technical Note D-882 (May) (1961) 36.

[84] J. M. Hedgepeth, P. V. Dyke, Local Stress Concentrations in Imperfect Filamentary Composite Materials, Journal of Composite Materials 1 (3) (1967) 294–309. `doi:10.1177/002199836700100305`.

[85] H. Fukuda, K. Kawata, On the stress concentration factor in fibrous composites, Fibre Science and Technology 9 (3) (1976) 189–203. `doi:10.1016/0015-0568(76)90003-8`.

[86] H. Zweben, B. Bell, Tensile Failure Criteria for fiber composite material, NASA Contractor Report vi, 12, 13 (August) (1972) 166.

[87] S. J. Zhou, W. A. Curtin, Failure of fiber composites: A lattice green function model, Acta Metallurgica Et Materialia`doi:10.1016/0956-7151(95)00003-E`.

[88] C. M. Landis, I. J. Beyerlein, R. M. McMeeking, Micromechanical simulation of the failure of fiber reinforced composites, Journal of the Mechanics and Physics of Solids 48 (3) (2000) 621–648. `doi:10.1016/S0022-5096(99)00051-4`.

[89] T. Okabe, N. Takeda, Y. Kamoshida, M. Shimizu, W. A. Curtin, A 3D shear-lag model considering micro-damage and statistical strength prediction of unidirectional fiber-reinforced composites, Compos Sci Technol 61 (2001) 1773–1787. `doi:10.1016/S0266-3538(01)00079-3`.

[90] T. Okabe, H. Sekine, K. Ishii, M. Nishikawa, N. Takeda, Numerical method for failure simulation of unidirectional fiber-reinforced composites with spring element model, Composites Science and Technology 65 (6) (2005) 921–933. `doi:10.1016/j.compscitech.2004.10.030`.

[91] M. J. Hinton, A. S. Kaddour, P. D. Soden, Evaluation of failure prediction in composite laminates: background to 'part C' of the exercise, Composites

Science and Technology 64 (3) (2004) 321–327. `doi:https://doi.org/10.1016/S0266-3538(03)00216-1`.

[92] A. S. Kaddour, M. J. Hinton, P. A. Smith, S. Li, A comparison between the predictive capability of matrix cracking, damage and failure criteria for fibre reinforced composite laminates: Part A of the third world-wide failure exercise, Journal of Composite Materials 47 (20-21) (2013) 2749–2779. `doi:10.1177/0021998313499476`.

[93] A. S. Kaddour, M. J. Hinton, Maturity of 3D failure criteria for fibre-reinforced composites: Comparison between theories and experiments: Part B of WWFE-II, Journal of Composite Materials 47 (6-7) (2013) 925–966. `doi:10.1177/0021998313478710`.

[94] W. A. Curtin, N. Takeda, Tensile Strength of Fiber-Reinforced Composites: II. Application to Polymer Matrix Composites, Journal of Composite Materials 32 (22) (1998) 2060–2081. `doi:10.1177/002199839803202204`.

[95] T. Okabe, M. Nishikawa, N. Takeda, H. Sekine, Effect of matrix hardening on the tensile strength of alumina fiber-reinforced aluminum matrix composites, Acta Materialia 54 (9) (2006) 2557–2566. `doi:10.1016/j.actamat.2006.01.044`.

[96] J. Noda, M. Nakada, Y. Miyano, Temperature Dependence of Accumulation of Fiber Breakages under Tensile Loading for Unidirectional CFRP Laminates, Journal of Reinforced Plastics and Composites 27 (10) (2008) 1005–1019. `doi:10.1177/0731684407086628`.

[97] T. Okabe, K. Ishii, M. Nishikawa, N. Takeda, Prediction of Tensile Strength of Unidirectional CFRP Composites, Advanced Composite Materials 19 (3) (2010) 229–241. `doi:10.1163/092430409X12605406698273`.

[98] S. Pimenta, S. T. Pinho, Hierarchical scaling law for the strength of composite fibre bundles, Journal of the Mechanics and Physics of Solids 61 (6) (2013) 1337–1356. `doi:10.1016/j.jmps.2013.02.004`.

[99] R. P. Tavares, F. Otero, A. Turon, P. P. Camanho, Effective simulation of the mechanics of longitudinal tensile failure of unidirectional polymer composites, International Journal of Fracture 208 (1-2) (2017) 269–285. `doi:10.1007/s10704-017-0252-9`.

[100] R. P. Tavares, F. Otero, J. Baiges, A. Turon, P. P. Camanho, A dynamic spring element model for the prediction of longitudinal failure of polymer composites, Computational Materials Science 160 (2019) 42–52. `doi:10.1016/j.commatsci.2018.12.048`.

[101] S. Pimenta, A computationally-efficient hierarchical scaling law to predict damage accumulation in composite fibre-bundles, Composites Science and Technology 146 (2017) 210–225. `doi:10.1016/j.compscitech.2017.04.018`.

[102] W. I. Newman, A. M. Gabrielov, Failure of hierarchical distributions of fibre bundles. I, International Journal of Fracture 50 (1) (1991) 1–14. `doi:10.1007/BF00035165`.

[103] A. Kelly, R. Tyson, W, Tensile Properties of Fibre.Reinforced Metals: Copper/-Tungsten and Copper/Molybdenum, J. Mech. Phys. solids 13 (1965) 329–350.

[104] Y. Swolfs, L. Gorbatikh, I. Verpoest, Stress concentrations in hybrid unidirectional fibre-reinforced composites with random fibre packings, Composites Science and Technology 85 (2013) 10–16. `doi:10.1016/j.compscitech.2013.05.013`.

[105] Y. Swolfs, R. M. McMeeking, I. Verpoest, L. Gorbatikh, The effect of fibre dispersion on initial failure strain and cluster development in unidirectional carbon/glass hybrid composites, Composites Part A: Applied Science and Manufacturing 69 (2014) 279–287. `doi:10.1016/j.compositesa.2014.12.001`.

[106] Y. Swolfs, I. Verpoest, L. Gorbatikh, Maximising the hybrid effect in unidirectional hybrid composites, Materials and Design 93 (2016) 39–45. `doi:10.1016/j.matdes.2015.12.137`.

[107] M. R. Wisnom, G. Czél, Y. Swolfs, M. Jalalvand, L. Gorbatikh, I. Verpoest, Hybrid effects in thin ply carbon/glass unidirectional laminates: accurate experimental determination and prediction, Composites Part A: Applied Science and Manufacturing 88 (2016) 131–139. `doi:10.1016/j.compositesa.2016.04.014`.

[108] A. Thionnet, J. Renard, Multi-scale analysis to determine fibre/matrix debonding criteria in SiCTitanium composites with and without consideration of the manufacturing residual stresses, Composites Science and Technology 58 (6) (1998) 945–955. `doi:10.1016/S0266-3538(97)00220-0`.

[109] F. Feyel, A multilevel finite element method (FE2) to describe the response of highly non-linear structures using generalized continua, Computer Methods in Applied Mechanics and Engineering`doi:10.1016/S0045-7825(03)00348-7`.

[110] F. V. Souza, D. H. Allen, Y. R. Kim, Multiscale model for predicting damage evolution in composites due to impact loading, Composites Science and Technology 68 (13) (2008) 2624–2634. `doi:10.1016/j.compscitech.2008.04.043`.

[111] H. Y. Chou, A. R. Bunsell, G. Mair, A. Thionnet, Effect of the loading rate on ultimate strength of composites. Application: Pressure vessel slow burst test, Composite Structures 104 (2013) 144–153. `doi:10.1016/j.compstruct.2013.04.003`.

[112] A. Scott, I. Sinclair, S. Spearing, A. Thionnet, A. Bunsell, Damage accumulation in a carbon/epoxy composite: Comparison between a multiscale model and computed tomography experimental results, Composites Part A: Applied Science and Manufacturing 43 (9) (2012) 1514–1522. `doi:10.1016/j.compositesa.2012.03.011`.

[113] A. S. Kaddour, M. J. Hinton, P. A. Smith, S. Li, Mechanical properties and details of composite laminates for the test cases used in the third world-wide failure exercise, Journal of Composite Materials 47 (20-21) (2013) 2427–2442. `doi:10.1177/0021998313499477`.

[114] F. Tanaka, T. Okabe, H. Okuda, I. A. Kinloch, R. J. Young, Factors controlling the strength of carbon fibres in tension, Composites Part A: Applied Science and Manufacturing 57 (2014) 88–94. `doi:10.1016/j.compositesa.2013.11.007`.

[115] E. M. Odom, D. F. Adams, Specimen size effect during tensile testing of an unreinforced polymer, Journal of Materials Science 27 (7) (1992) 1767–1771. `doi:10.1007/BF01107202`.

[116] T. Hobbiebrunken, B. Fiedler, M. Hojo, M. Tanaka, Experimental determination of the true epoxy resin strength using micro-scaled specimens, Composites Part A: Applied Science and Manufacturing 38 (3) (2007) 814–818. `doi:10.1016/j.compositesa.2006.08.006`.

[117] X. Ji, X.-R. Liu, T.-W. Chou, Dynamic Stress Concentration Factors in Unidirectional Composites, Journal of Composite Materials 19 (3) (1985) 269–275. `doi:10.1177/002199838501900305`.

[118] R. Ganesh, S. Sockalingam, B. Z. Haque, J. W. Gillespie, Dynamic effects of single fiber break in unidirectional glass fiber-reinforced composites, Journal of Composite Materials 51 (9) (2017) 1307–1320. `doi:10.1177/0021998316669218`.

[119] T. Belytschko, W. K. Liu, B. Moran, Nonlinear finite elements for continua and structures, Wiley, 2000.

[120] L. St-Pierre, N. J. Martorell, S. T. Pinho, Stress redistribution around clusters of broken fibres in a composite, Composite Structures 168. `doi:10.1016/j.compstruct.2017.01.084`.

[121] D. J. Boll, W. D. Bascom, J. C. Weidner, W. J. Murri, A microscopy study of impact damage of epoxy-matrix carbon-fibre composites, Journal of Materials Science 21 (8) (1986) 2667–2677. `doi:10.1007/bf00551471`.

[122] M. G. R. Sause, S. Richler, Finite element modelling of cracks as acoustic emission sources, Journal of Nondestructive Evaluation 34 (1) (2015) 4. `doi:10.1007/s10921-015-0278-8`.

[123] S. Kalafat, A.-M. Zelenyak, M. G. R. Sause, In-situ monitoring of composite failure by computing tomography and acoustic emission, 20th International Conference on Composite Materials (October) (2015) 1–8.

[124] F. Aymerich, S. Meili, Ultrasonic evaluation of matrix damage in impacted composite laminates, Composites Part B: Engineering 31 (1) (2000) 1–6. `doi:10.1016/S1359-8368(99)00067-0`.

[125] V. P. Vavilov, S. Marinetti, E. G. Grinzato, P. G. Bison, Thermal tomography characterization and pulse-phase thermography of impact damage in CFRP, or why end users are still reluctant about practical use of transient IR thermography, Thermosense XX 3361 (March 1998) (1998) 275–281. `doi:10.1117/12.304737`.

[126] P. Wright, A. Moffat, I. Sinclair, S. M. Spearing, High resolution tomographic imaging and modelling of notch tip damage in a laminated composite, Composites Science and Technology 70 (10) (2010) 1444–1452. `doi:10.1016/j.compscitech.2010.04.012`.

[127] P. Wright, X. Fu, I. Sinclair, S. Spearing, Ultra High Resolution Computed Tomography of Damage in Notched Carbon Fiber–Epoxy Composites, Journal of Composite Materials 42 (19) (2008) 1993–2002. `doi:10.1177/0021998308092211`.

[128] A. E. Scott, I. Sinclair, S. M. Spearing, M. N. Mavrogordato, W. Hepples, Influence of voids on damage mechanisms in carbon/epoxy composites determined via high resolution computed tomography, Composites Science and Technology 90 (2014) 147–153. `doi:10.1016/j.compscitech.2013.11.004`.

[129] S. R. Stock, X-ray microtomography of materials, International Materials Reviews 44 (4) (1999) 141–164. `doi:10.1179/095066099101528261`.

[130] E. Maire, J. Y. Buffière, L. Salvo, J. J. Blandin, W. Ludwig, J. M. Létang, On the application of X-ray microtomography in the field of materials science, Advanced Engineering Materials 3 (8) (2001) 539–546. `doi:10.1002/1527-2648(200108)`.

[131] S. R. Stock, Recent advances in X-ray microtomography applied to materials, International Materials Reviews 53 (3) (2008) 129–181. `doi:10.1179/174328008X277803`.

[132] R. Hanke, T. Fuchs, M. Salamon, S. Zabler, X-ray Microtomography for Materials Characterization, Elsevier Ltd, 2016. `doi:10.1016/B978-0-08-100040-3.00003-1`.

[133] L. Salvo, P. Cloetens, E. Maire, S. Zabler, J. J. Blandin, J. Y. Buffière, W. Ludwig, E. Boller, D. Bellet, C. Josserond, X-ray micro-tomography an attractive characterisation technique in materials science, Nuclear Instruments and Methods in Physics Research, Section B: Beam Interactions with Materials and Atoms 200 (2003) 273–286. `doi:10.1016/S0168-583X(02)01689-0`.

[134] K. Ogawa, Y. Harata, T. Ichihara, A. Kubo, S. Hashimoto, A Practical Method for Position-Dependent Compton-Scatter Correction in Single Photon Emission CT, IEEE Transactions on Medical Imaging 10 (3) (1991) 408–412. `doi:10.1109/42.97591`.

[135] S. J. Norton, Compton scattering tomography, Journal of Applied Physics 76 (4) (1994) 2007–2015. `doi:10.1063/1.357668`.

[136] G. T. Herman, Fundamentals of Computerized Tomography: Image Reconstruction from Projections, 2nd Edition, Springer Publishing Company, Incorporated, 2009.

[137] E. N. Landis, D. T. Keane, X-ray microtomography, Materials Characterization 61 (12) (2010) 1305–1316. `doi:10.1016/j.matchar.2010.09.012`.

[138] T. Flohr, CT Systems, Current Radiology Reports 1 (1) (2013) 52–63. `doi:10.1007/s40134-012-0005-5`.

[139] J. A. Ambrose, Computerized transverse axial tomography, The British journal of radiology 46 (545) (1973) 401. `doi:10.1259/0007-1285-46-545-401`.

[140] J. Hsieh, Key Performance Parameters of the CT Scanner, Computed Tomography Principles, Design, Artifacts, and Recent Advances (2009) 143–178.

[141] F. P. Vidal, J. M. Létang, G. Peix, P. Cloetens, Investigation of artefact sources in synchrotron microtomography via virtual X-ray imaging, Nuclear Instruments and Methods in Physics Research, Section B: Beam Interactions with Materials and Atoms 234 (3) (2005) 333–348. `doi:10.1016/j.nimb.2005.02.003`.

[142] F. P. Vidal, J. M. Létang, G. Peix, P. Cloetens, Investigation of artefact sources in synchrotron microtomography via virtual X-ray imaging, Nuclear Instruments and Methods in Physics Research, Section B: Beam Interactions with Materials and Atoms 234 (3) (2005) 333–348. `doi:10.1016/j.nimb.2005.02.003`.

[143] S. C. Garcea, Y. Wang, P. J. Withers, X-ray computed tomography of polymer composites, Composites Science and Technology 156 (2018) 305–319. `doi:10.1016/j.compscitech.2017.10.023`.

[144] S. Ebashi, M. Koch, E. Rubenstein, Handbook on synchrotron radiation, volume 4, North-Holland ; Sole distributors for the USA and Canada, Elsevier Science Pub. Co., Amsterdam; New York; New York, NY, USA, 1991.

[145] B. P. Flannery, H. W. Deckman, W. G. Roberge, K. L. Amico, Three-Dimensional X-ray Microtomography, Science 237 (4821) (1987) 1439–1444. `doi:10.1126/science.237.4821.1439`.

[146] S. W. Wilkins, T. E. Gureyev, D. Gao, A. Pogany, A. W. Stevenson, Phase-contrast imaging using polychromatic hard X-rays, Nature 384 (6607) (1996) 335–338. `doi:10.1038/384335a0`.

[147] J. Baruchel, J. Y. Buffiere, E. Maire, X-ray tomography in material science, Hermes science publications, France, 2000.

[148] E. Maire, P. J. Withers, Quantitative X-ray tomography, International Materials Reviews 59 (1) (2014) 1–43. `doi:10.1179/1743280413Y.0000000023`.

[149] P. C. Diemoz, A. Bravin, P. Coan, Theoretical comparison of three X-ray phase-contrast imaging techniques: propagation-based imaging, analyzer-based imaging and grating interferometry, Opt. Express 20 (3) (2012) 2789–2805. `doi:10.1364/OE.20.002789`.

[150] S. C. Mayo, A. W. Stevenson, S. W. Wilkins, In-Line Phase-Contrast X-ray Imaging and Tomography for Materials Science, Materials 5 (12) (2012) 937–965. `doi:10.3390/ma5050937`.

[151] P. Cloetens, W. Ludwig, J. Baruchel, D. Van Dyck, J. Van Landuyt, J. P. Guigay, M. Schlenker, Holotomography: Quantitative phase tomography with micrometer resolution using hard synchrotron radiation x rays, Applied Physics Letters 75 (19) (1999) 2912–2914. `doi:10.1063/1.125225`.

[152] P. Cloetens, R. Barrett, J. Baruchel, J. P. Guigay, M. Schlenker, Phase objects in synchrotron radiation hard x-ray imaging, Journal of Physics D: Applied Physics 29 (1) (1996) 133–146. `doi:10.1088/0022-3727/29/1/023`.

[153] D. Paganin, S. C. Mayo, T. E. Gureyev, P. R. Miller, S. W. Wilkins, Simultaneous phase and amplitude extraction from a single defocused image of a homogeneous object, Journal of Microscopy 206 (1) (2002) 33–40. `doi:10.1046/j.1365-2818.2002.01010.x`.

[154] J. A. Dunlop, S. Wirth, D. Penney, A. McNeil, R. S. Bradley, P. J. Withers, R. F. Preziosi, A minute fossil phoretic mite recovered by phase-contrast x-ray computed tomography, Biology Letters 8 (3) (2012) 457–460. `doi:10.1098/rsbl.2011.0923`.

[155] B. A. Dowd, G. H. Campbell, R. B. Marr, V. V. Nagarkar, S. V. Tipnis, L. Axe, D. P. Siddons, Developments in synchrotron x-ray computed microtomography at the National Synchrotron Light Source, Proc. SPIE 3772 (July) (1999) 224–236. `doi:10.1117/12.363725`.

[156] L. Salvo, M. Suéry, A. Marmottant, N. Limodin, D. Bernard, 3D imaging in material science: Application of X-ray tomography, Comptes Rendus Physique 11 (9-10) (2010) 641–649. `doi:10.1016/j.crhy.2010.12.003`.

[157] B. Yu, R. S. Bradley, C. Soutis, P. J. Withers, A comparison of different approaches for imaging cracks in composites by X-ray microtomography, Philosophical Transactions of the Royal Society A: Mathematical, Physical and Engineering Sciences 374 (2071). `doi:10.1098/rsta.2016.0037`.

[158] J. Y. Buffiere, E. Maire, J. Adrien, J. P. Masse, E. Boller, In situ experiments with X ray tomography: An attractive tool for experimental mechanics, Proceedings of the Society for Experimental Mechanics, Inc. 67 (2010) 289–305. `doi:10.1007/s11340-010-9333-7`.

[159] F. Xu, Quantitative characterization of deformation and damage process by digital volume correlation: A review, Theoretical and Applied Mechanics Letters 8 (2) (2018) 83–96. `doi:10.1016/j.taml.2018.02.004`.

[160] L. Mishnaevsky, P. Brøndsted, Micromechanisms of damage in unidirectional fiber reinforced composites: 3D computational analysis, Composites Science and Technology 69 (7-8) (2009) 1036–1044. `doi:10.1016/j.compscitech.2009.01.022`.

[161] Y. Swolfs, R. M. McMeeking, V. P. Rajan, F. W. Zok, I. Verpoest, L. Gorbatikh, Global load-sharing model for unidirectional hybrid fibre-reinforced composites, Journal of the Mechanics and Physics of Solids 84 (2015) 380–394. `doi:10.1016/j.jmps.2015.08.009`.

[162] C. M. Landis, R. M. McMeeking, A shear-lag model for a broken fiber embedded in a composite with a ductile matrix, Composites Science and Technology 59 (3) (1999) 447–457. `doi:10.1016/S0266-3538(98)00091-8`.

[163] H. L. Cox, The elasticity and strength of paper and other fibrous materials, British Journal of Applied Physics 3 (3) (1952) 72–79. `doi:10.1088/0508-3443/3/3/302`.

[164] R. Ganesh, S. Sockalingam, J. W. Gillespie, Dynamic effects of a single fiber break in unidirectional glass fiber-reinforced polymer composites: Effects of matrix plasticity, Journal of Composite Materials 52 (14) (2018) 1873–1886. `doi:10.1177/0021998317737604`.

[165] N. Otsu, A threshold selection method from gray-level histograms, IEEE Transactions on Systems, Man, and Cybernetics C (1) (1979) 62–66. `doi:10.1109/TSMC.1979.4310076`.

[166] S. Connell, F. Zok, Z. Du, Z. Suo, On the tensile properties of a fiber reinforced titanium matrix composite—II. Influence of notches and holes, Acta Metallurgica et Materialia 42 (10) (1994) 3451–3461. `doi:10.1016/0956-7151(94)90478-2`.

[167] D. B. Gundel, F. E. Wawner, Experimental and theoretical assessment of the longitudinal tensile strength of unidirectional sic-fiber/titanium-matrix composites, Composites Science and Technology 57 (4) (1997) 471–481. `doi:10.1016/S0266-3538(96)00163-7`.

[168] G. Borstnar, F. Gillard, M. N. Mavrogordato, I. Sinclair, S. M. Spearing, Three-dimensional deformation mapping of Mode i interlaminar crack extension in particle-toughened interlayers, Acta Materialia 103 (2016) 63–70. `doi:10.1016/j.actamat.2015.09.059`.

[169] S. C. Garcea, M. N. Mavrogordato, A. E. Scott, I. Sinclair, S. M. Spearing, Fatigue micromechanism characterisation in carbon fibre reinforced polymers using synchrotron radiation computed tomography, Composites Science and Technology 99 (2014) 23–30. `doi:10.1016/j.compscitech.2014.05.006`.

[170] S. C. Garcea, I. Sinclair, S. M. Spearing, Fibre failure assessment in carbon fibre reinforced polymers under fatigue loading by synchrotron X-ray computed tomography, Composites Science and Technology 133 (2016) 157–164. `doi:10.1016/j.compscitech.2016.07.030`.

[171] P. D. Soden, A. S. Kaddour, M. J. Hinton, Recommendations for designers and researchers resulting from the world-wide failure exercise, Failure Criteria in Fibre-Reinforced-Polymer Composites 64 (2004) 1223–1251. `doi:10.1016/B978-008044475-8/50039-1`.

[172] G. Yamamoto, M. Onodera, K. Koizumi, J. Watanabe, H. Okuda, F. Tanaka, T. Okabe, Considering the stress concentration of fiber surfaces in the prediction of the tensile strength of unidirectional carbon fiber-reinforced plastic composites, Composites Part A: Applied Science and Manufacturing 121 (June 2018) (2019) 499–509. `doi:10.1016/j.compositesa.2019.04.011`.

[173] Y. Swolfs, I. Verpoest, L. Gorbatikh, Maximising the hybrid effect in unidirectional hybrid composites, Materials and Design 93 (2016) 39–45. `doi:10.1016/j.matdes.2015.12.137`.

[174] T. C. C.J. Creighton, M.P.F. Sutcliffe, A multiple field image analysis procedure for characterisation of fibre alignment in composites, Selenium: Its Molecular Biology and Role in Human Health 9781461410 (2012) 335–344. `doi:10.1007/978-1-4614-1025-6_26`.

[175] M. W. Czabaj, M. L. Riccio, W. W. Whitacre, Numerical reconstruction of graphite/epoxy composite microstructure based on sub-micron resolution X-ray computed tomography, Composites Science and Technology 105 (2014) 174–182. `doi:10.1016/j.compscitech.2014.10.017`.

[176] M. J. Emerson, K. M. Jespersen, A. B. Dahl, K. Conradsen, L. P. Mikkelsen, Individual fibre segmentation from 3D X-ray computed tomography to study the misalignment in unidirectional composite materials, Composites Part A: Applied Science and Manufacturing 97 (2016) 83–92. `doi:10.1016/j.compositesa.2016.12.028`.

[177] W. S. Rasband, ImageJ, U. S. National Institutes of Health, Bethesda, Maryland, USA, 1997.
`https://imagej.nih.gov/ij/`

[178] C. M. Thompson, L. Shure, Image Processing Toolbox: For Use with MATLAB;[user's Guide], MathWorks, 1995.

[179] T. B. Arnold, J. W. Emerson, Nonparametric Goodness-of-Fit Tests for Discrete Null Distributions, The R Journal 3 (2) (2011) 34–39.
`https://journal.r-project.org/archive/`

[180] R Core Team, R: A Language and Environment for Statistical Computing, R Foundation for Statistical Computing, Vienna, Austria, 2019.
`http://www.r-project.org/`

[181] H.-Y. Kim, Statistical notes for clinical researchers: assessing normal distribution (2) using skewness and kurtosis, Restorative Dentistry & Endodontics 38 (1) (2013) 52. `doi:10.5395/rde.2013.38.1.52`.

[182] F. Pukelsheim, The Three Sigma Rule, The American Statistician 48 (2) (1994) 88–91. `doi:10.1080/00031305.1994.10476030`.

[183] K. D. Hopkins, D. L. Weeks, Tests for Normality and Measures of Skewness and Kurtosis: Their Place in Research Reporting, Educational and Psychological Measurement 50 (4) (1990) 717–729. `doi:10.1177/0013164490504001`.

[184] C. M. Landis, R. M. McMeeking, Stress concentrations in composites with interface sliding, matrix stiffness and uneven fiber spacing using shear lag theory, International Journal of Solids and Structures 36 (28) (1999) 4333–4361. `doi:10.1016/S0020-7683(98)00193-0`.

[185] D. G. Harlow, S. L. Phoenix, Probability distributions for the strength of composite materials II: A convergent sequence of tight bounds, International Journal of Fracture 17 (6) (1981) 601–630. `doi:10.1007/BF00681559`.

[186] K. E. Jackson, S. Kellas, J. Morton, Scale Effects in the Response and Failure of Fiber Reinforced Composite Laminates Loaded in Tension and in Flexure, Journal of Composite Materials 26 (18) (1992) 2674–2705. `doi:10.1177/002199839202601803`.

[187] M. R. Wisnom, J. W. Atkinson, Reduction in tensile and flexural strength of unidirectional glass fibre-epoxy with increasing specimen size, Composite Structures 38 (1-4) (1997) 405–411. `doi:10.1016/S0263-8223(97)00075-5`.

[188] M. Wisnom, S. Hallett, C. Soutis, Scaling Effects in Notched Composites, Journal of Composite Materials 44 (2) (2010) 195–210. `doi:10.1177/0021998309339865`.

[189] G. Borstnar, Micro-mechanical contributions to interlaminar toughness in particle-toughened CFRPs (January) (2016) 277.
`https://eprints.soton.ac.uk/393743/`